

Poster Session

-Poster Session-

The poster number with "S" is eligible for the Best Student Poster Award nomination.

P01 Research and Development of Magnet for HiSOR-II

Y. Lu^a, M. Shimada^{c,a}, H. Miyauchi^{c,a}, M. Katoh^{a,b}

a Hiroshima Synchrotron Radiation Center, Hiroshima University, HSRC, Japan

b Institute for Molecular Science, Okazaki, IMS, Japan

c High Energy Accelerator Research Organization, KEK, Japan

P02S Experimental Study on Single Electron Storage

Y. Asai^a, H. Miyauchi^{b,c}, M. Shimada^{b,c}, M. Katoh^{b,d}

a Graduate School of Advanced Science and Engineering Hiroshima University, Japan

b Hiroshima Synchrotron Radiation Center (HSRC), Hiroshima University, Japan

c High Energy Accelerator Research Organization (KEK), Japan

d UVSOR Synchrotron Facility, Japan

P03 Diffraction of Optical Vortex from Undulator

Y. Nishihara^a, M. Shimada^{c,b}, H. Miyauchi^{c,b}, K. Matsuo^{b,a}, M. Katoh^{b,a,d}

a School of Science, Hiroshima University, Japan

b Hiroshima Synchrotron Radiation Center (HSRC), Hiroshima University, Japan

c High Energy Accelerator Research Organization (KEK), Japan

d UVSOR Synchrotron Facility, Japan

P04S Unexpected two-fold symmetry of the electronic structure in heavily overdoped Bi2201 observed by angle-resolved photoemission spectroscopy

Y. Miyai^a, S. Ideta^b, T. Kurosawa^c, M. Oda^d, K. Tanaka^e, M. Arita^b

K. Shimada^b

a Graduate School of Advanced Science and Engineering, Hiroshima University, Japan

b Hiroshima Synchrotron Radiation Center, Hiroshima University, Japan

c Faculty of Science and Engineering, Muroran Institute of Technology, Japan

d Department of Physics, Hokkaido University, Japan

e UVSOR-III Synchrotron, Institute for Molecular Science, Japan

P05S Comprehensive Studies of the Electronic Structure for the Double-layer high- T_c Superconductor $\text{Bi}_2\text{Sr}_2\text{CaCu}_2\text{O}_{8+\delta}$

- Revisit of the Phase Diagram by ARPES

Y. Tsubota^a, Y. Miyai^b, S. Kumar^{b,c}, K. Tanaka^d, S. Ishida^e, H. Eisaki^e,

S. Nakagawa^f, T. Kashiwagi^f, M. Arita^b, K. Shimada^{a,b}, S. Ideta^{a,b}

a Graduate School of Advanced Science and Engineering, Hiroshima Univ., Japan

b Hiroshima Synchrotron Radiation Center (HiSOR), Hiroshima Univ., Japan

c Institute of Microelectronics (IME), Agency for Science, Technology and Research (A STAR), Singapore*

d UVSOR-III Synchrotron, Institute for Molecular Science, Japan

e National Institute of Advanced Industrial Science and Technology (AIST), Japan

f Division of Materials Science, Tsukuba University, Japan

-Poster Session-

The poster number with "S" is eligible for the Best Student Poster Award nomination.

P06S Probing the Electronic Band Structure of Altermagnetic

MnTe: An ARPES Study

K. G. Martuza^a, Y. Kumar^a, S. Kumar^{b,c}, S. Ideta^{a,b}, K. Shimada^{a,b}

a Graduate School of Advanced Science and Engineering, Hiroshima University, Japan

b Hiroshima Synchrotron Radiation Centre (HiSOR), Hiroshima University, Japan

*c Institute of Microelectronics, Agency for Science, Technology and Research (A*STAR), Singapore*

P07S Effects of Quantum Charge Fluctuations on the Electron Self-energy of High- T_c Cuprate Superconductors Using Angle-Resolved Photoemission and Inverse Photoemission Spectroscopies

Y. Onishi^a, Y. Miyai^a, Y. Tsubota^a, K. Tanaka^c, S. Ishida^d, H. Eisaki^d,

H. Sato^b, M. Arita^b, K. Shimada^{a,b}, S. Ideta^{a,b}

a Graduate School of Advanced Science and Engineering, Hiroshima Univ., Japan

b Hiroshima Synchrotron Radiation Center (HiSOR), Hiroshima Univ., Japan

c UVSOR-III Synchrotron, Institute for Molecular Science, Japan

d National Institute of Advanced Industrial Science and Technology (AIST), Japan

P08S Observation of Topological Surface States and Non-symmorphic Band Degeneracy in Superconducting PdSeTe Single-crystal

Y. Kumar^a, S. Kumar^b, Y. Venkateswara^d, R. Oishi^a, J. Nayak^c, T. Onimaru^a,

S. Ideta^{a,b}, K. Shimada^{a,b}

a Graduate School of Advanced Science and Engineering, Hiroshima University, Japan

b Hiroshima Synchrotron Radiation Centre (HiSOR), Hiroshima University, Japan

c Department of Physics, Indian Institute of Technology, India

d Department of Physics, SUNY Buffalo State University, USA

P09S Strain-Induced Relocation of Topological Surface States in Bi₂Se₃ Single Crystal

Y. Kumar^a, S. Kumar^b, S. Ideta^{a,b}, T. Okuda^{a,b}, K. Shimada^{a,b}

a Graduate School of Advanced Science and Engineering, Hiroshima University, Japan

b Hiroshima Synchrotron Radiation Centre (HiSOR), Hiroshima University, Japan

P10S Research of Charge Fluctuations in the Electron-doped High- T_c Cuprate NCCO Revealed by ARPES and IPES

H. Yamaguchi^a, Y. Onishi^b, Y. Miyai^b, Y. Tsubota^b, M. Atira^c, K. Tanaka^d,

H. Sato^c, D. Song^e, K. Shimada^{b,c}, S. Ideta^{b,c}

a School of Science, Hiroshima Univ., Japan

b Graduate School of Advanced Science and Engineering, Hiroshima Univ., Japan

c Hiroshima Synchrotron Radiation Center (HiSOR), Hiroshima Univ., Japan

d UVSOR-III Synchrotron, Institute for Molecular Science, Japan

e Stewart Blusson Quantum Matter Institute, University of British Columbia, Canada

-Poster Session-

The poster number with "S" is eligible for the Best Student Poster Award nomination.

- P11 XPS study on the boron-doped amorphous carbon films**
Y. Muraoka^a, K. Matuso^b, T. Wakita^a, T. Yokoya^a
a Research Institute for Interdisciplinary Science, Okayama University, Japan
b Graduate School of Natural Science and Technology, Okayama University, Japan
- P12 Synchrotron ARPES studies of nodal line semimetal LaTe_{1+x}Bi_{1-x}**
R. Saito^a, Y. Okishi^a, T. Higashikawa^a, T. Wakita^{a,b}, Y. Kumar^c, Y. Miyai^c,
H. Kageyama^a, R. Kondo^a, Y. Nogami^a, S. Ideta^c, K. Shimada^c, Y. Muraoka^{a,b},
T. Yokoya^{a,b}
a Graduate School of Natural Science and Technology, Okayama University, Japan
b Research Institute for Interdisciplinary Science, Okayama University, Japan
c Hiroshima Synchrotron Radiation Center, Hiroshima University, Japan
- P13 Current Activities of Research and Education on BL-5 (FY2023)**
T. Yokoya^{a,b}, T. Wakita^a, Y. Muraoka^{a,b}
a Research Institute for Interdisciplinary Science, Okayama University, Japan
b Research Laboratory for Surface Science, Okayama University, Japan
- P14 Visualization of boron distributions in cancer cells dosed with a boron delivery drug**
T. Wakita^a, K. Igawa^b, M. Kaneda^c, N. Ikeda^c, H. Terato^d, Y. Muraoka^{a,c},
T. Yokoya^{a,c}
a Research Institute for Interdisciplinary Science, Okayama University, Japan
b INeutron Therapy Research Center, Okayama University, Japan
c Graduate School of Natural Science and Technology, Okayama University, Japan
d Advanced Science Research Center, Okayama University, Japan
- P15S Fermi surface of chiral magnet Yb(Ni_{1-x}Cu_x)₃Al₉ observed by ARPES**
Y. Tanimoto^a, M. Sugimoto^a, R. Kamimori^a, Y. Nakashima^b, H. Sato^c,
K. Yamagami^d, M. Arita^c, S. Kumar^c, K. Shimada^c, S. Nakamura^e, S. Ohara^e
a Graduate School of Advanced Science and Engineering, Hiroshima University, Japan
b Faculty of Science, Hiroshima University, Japan
c Hiroshima Synchrotron Radiation Center, Hiroshima University, Japan
d Japan Synchrotron Radiation Research Institute, Japan
e Graduate School of Engineering, Nagoya Institute of Technology, Japan
- P16 ARPES study of TiFe_xS₂ (x = 0, 0.33)**
Y. Nakashima^a, Y. Tanimoto^b, M. Sugimoto^b, H. Sato^c, Y. Miyai^b, S. Ideta^c,
K. Shimada^c, M. Miyata^d, M. Koyano^d
a Faculty of Science, Hiroshima University, Japan
b Graduate School of Advanced Science and Engineering, Hiroshima University, Japan
c Hiroshima Synchrotron Radiation Center, Hiroshima University, Japan
d School of Materials Science, Japan Advanced Institute of Science and Technology, Japan
- P17S Preparation of Pt Thin Film on MgO (001) and Observation of Its Electronic Structure**
T. Asano^a, K. Sumida^b, K. Kunitomo^a, T. Okuda^b, K. Miyamoto^b
a Graduate School of Advanced Science and Engineering, Hiroshima University, Japan
b Hiroshima Synchrotron radiation Center (HSRC), Hiroshima University, Japan

-Poster Session-

The poster number with "S" is eligible for the Best Student Poster Award nomination.

P18S Attempt to Control the Anisotropy of Topological Surface States

R. Yamamoto^a, K. Sumida^b, K. Miyamoto^b, T. Okuda^b

a Graduate School of Advanced Science and Engineering Hiroshima University, Japan

b Hiroshima Synchrotron Radiation Center (HSRC), Hiroshima University, Japan

P19S Spin-polarized electronic states of FeCo thin film on Rh(001) substrate

K. Kunitomo^a, K. Sumida^b, K. Miyamoto^b, C. Zhang^a, Y. Sakuraba^c, T. Okuda^b

a Graduate School of Advanced Science and Engineering Hiroshima University, Japan

b Hiroshima Synchrotron Radiation Center (HSRC), Hiroshima University, Japan

c National Institute for Materials Science (NIMS), Japan

P20 Ultrafast Spin-Dependent Dynamics in a Carrier-Tuned Topological Insulator

K. Sumida^a, K. Kunitomo^b, M. Kakoki^b, K. A. Kokh^c, O. E. Tereshchenko^c,
J. Reimann^d, J. Gddede^d, U. Hfer^d, K. Miyamoto^a, T. Okuda^{a,e}, A. Kimura^{b,e}

a Hiroshima Synchrotron Radiation Center, Hiroshima University, Japan

b Graduate School of Advanced Science and Engineering, Hiroshima University, Japan

c Physics Department, Novosibirsk State University, Russia

d Department of Physics and Materials Sciences Center, Philipps-University, Germany

e International Institute for Sustainability with Knotted Chiral Meta Matter (SKCM2), Japan

P21S Demonstration of phase-resolved spin-ARPES on topological surface states in Bi₂Te₃

T. Kousa^a, T. Iwata^{a,b}, S. Kumar^c, A. Kimura^{a,b}, K. Miyamoto^c, T. Okuda^{b,c},
K. Kuroda^{a,b}

a Graduate School of Advanced Science and Engineering, Hiroshima University, Japan

b International Institute for Sustainability with Knotted Chiral Meta Matter(WPI-SKCM2), Hiroshima University, Japan

c Hiroshima Synchrotron Radiation Center, Hiroshima University, Japan

P22S Performance of laser-based SARPES with micrometer spatial and vector spin resolution at HiSOR

T. Iwata^{a,b}, T. Kousa^a, A. Y. Nishioka^a, K. Ohwada^a, K. Sumida^c, E. Annese^d,
M. Kakoki^a, K. Kuroda^{a,b}, H. Iwasawa^e, M. Arita^c, S. Kumar^c, A. Kimura^{a,b},
K. Miyamoto^c, T. Okuda^{b,c}

a Grad. Sch. Adv. Sci. Eng., Hiroshima Univ., Japan

b WPI-SKCM-2., Hiroshima Univ., Japan

c HiSOR, Hiroshima Univ., Japan

d Brazilian Center for Research in Physics, Brazil

e Institute for Advanced Synchrotron Light Source, National Institutes for Quantum Science and Technology, Japan

P23 Direct Observation of Spin-split Electronic Structures in Antiferromagnet NdBi by Laser-based SARPES

R. Yamamoto^a, T. Motoyama^b, T. Iwata^{a,b}, T. Kosa^b, Y. Nishioka^b, K. Ideura^b,
M. Arita^c, S. Ideta^c, K. Shimada^{a,c}, K. Miyamoto^c, T. Okuda^{a,c}, A. Kimura^{a,b},
T. Onimaru^b, K. Kuroda^{a,b}

a International Institute for Sustainability with Knotted Chiral Meta Matter (WPI-SKCM2), Hiroshima University, Japan

b Graduate School of Advanced Science and Engineering, Hiroshima University, Japan

c Hiroshima Synchrotron Radiation Center, Hiroshima University, Japan

-Poster Session-

The poster number with "S" is eligible for the Best Student Poster Award nomination.

P24 Secondary Structural Changes of FUS-LC induced with Phase-Separation observed by VUV-CD

K. Fujii^a, N. Maita^a, K. Matsuo^b, M. Kato^a

a Institute for Quantum Life Science, National Institutes for Quantum Science and Technology, Japan

b Hiroshima Synchrotron Radiation Center, Hiroshima-university, Japan

P25 Insights into Physical Interactions and Structuration in Self-Assembled Azapeptide Hydrogels Through Spectroscopy Techniques

M. Ibrahim^{a,b}, J. Bodiguel^b, M. Averlant-Petit^b, K. Matsuo^a

a Hiroshima Synchrotron Radiation Center (HiSOR), Hiroshima University, Japan

b Université de Lorraine, CNRS, LCPM, France

P26S Monitoring the Self-Assembly of Alginate Hydrogel Using Synchrotron Radiation Circular Dichroism

T. Haga^a, M. Yoshida^a, T. Haino^a, K. Matsuo^b, M. I.A. Ibrahim^b

a Graduate School of Advanced Science and Engineering, Hiroshima University, Japan

b Hiroshima Synchrotron Radiation Center (HiSOR), Hiroshima University, Japan

P27S VUVCD Measurements of dried proteins and its application to protein-membrane interaction study

K. Hayashi^a, R. Imaura^a, K. Matsuo^{a,b}

a Graduate School of Advanced Science and Engineering, Hiroshima University, Japan

b Hiroshima Synchrotron Radiation Center, Hiroshima University, Japan

P28 Optical Activity Measurement of Circularly Polarized Lyman- α Light Irradiated and Magnetic Field Applied Amino-acid Films

J. Takahashi^a, M. Kobayashi^b, G. Fujimori^c, H. Ota^d, K. Matsuo^e, Y. Taira^d,

M. Katoh^{d,e}, K. Kobayashi^{c,f}, Y. Kebukawa^f, H. Nakamura^b

a Doshisha University, Japan

b National Institute for Fusion Science, Japan

c Yokohama National University, Japan

d UVSOR Synchrotron Facility, Japan

e Hiroshima Synchrotron Radiation Center, Japan

f Tokyo Institute of Technology, Japan

P29S Molecular orientation in polymer/fullerene blend films studied by NEXAFS

Y. Hanaki^a, H. Yoshida^{b,c}, T. Sekitani^{b,c}

a Faculty of Science, Hiroshima University, Japan

b Graduate School of Advanced Science and Engineering, Hiroshima University, Japan

c Hiroshima Synchrotron Radiation Center, Hiroshima University, Japan

-Poster Session-

The poster number with "S" is eligible for the Best Student Poster Award nomination.

P30S Charge Transfer in Gold Substrates and Nanoparticles Coated with Methyl Ester Substituted Aromatic Thiol Molecules

S. Tendo^a, A. Niozu^a, K. Yoshioka^a, J. Adachi^b, H. Tanaka^b, S. Wada^{a,b}
a Graduate School of Science and Engineering, Hiroshima University, Japan
b Photon Factory, Institute of Materials Structure Science, KEK, Japan
c Hiroshima Synchrotron Radiation Center, Hiroshima University, Japan

P31 Ultrafast charge transfer through biphenyl and fluorene monolayers studied by core-hole clock spectroscopy

A. Niozu^a, K. Yoshioka^a, S. Tendo^a, S. Asakura^b, Y. Hanaki^b, J. Koizumi^b,
Y. Ohura^b, J. Yamada^b, S. Wada^{a, c}
a Graduate School of Science and Engineering, Hiroshima University, Japan
b Faculty of Science, Hiroshima University, Japan
c Hiroshima Synchrotron Radiation Center, Hiroshima University, Japan

P32 Soft X-ray Absorption Spectroscopy of Phospholipid Films Supported on Au Substrates by Different Casting Techniques

Y. Ohura^a, K. Yoshioka^b, S. Tendo^b, A. Niozu^{a,b}, S. Wada^{a,b,c}
a Faculty of Science, Hiroshima University, Japan
b Graduate School of Science and Engineering, Hiroshima University, Japan
c Hiroshima Synchrotron Radiation Center, Hiroshima University, Japan

Research and Development of Magnet for HiSOR-II

Y. Lu^a, M. Shimada^{c,a}, H. Miyauchi^{c,a}, and M. Katoh^{a,b}

^aHiroshima Synchrotron Radiation Center, Hiroshima University, HSRC, Higashi-Hiroshima, Hiroshima 739-0046, Japan

^bInstitute for Molecular Science, Okazaki, IMS, Aichi 444-8585, Japan

^cHigh Energy Accelerator Research Organization, KEK, Tsukuba, Ibaraki 305-0801, Japan

Keywords: Combined-function magnet, Hybrid permanent magnet, Energy saving

HiSOR-II has been designed as a future plan of HSRC, which will provide higher brightness VUV radiation increasing by 2 orders of magnitude compared with the present HiSOR. To reduce the construction cost and accelerator size, the magnets in the ring lattice are being designed as combined-function magnets which are capable of producing multipole field components, such as dipole, quadrupole, and sextupole. On the basis of lattice parameters of HiSOR-II, we proposed two kinds of combined-function quadrupole-sextupole magnets using auxiliary coil and pole profile adjustment, respectively [1, 2]. The magnet model is simulated using Radia [3], which is shown in Figure 1. In the combined-function magnet using auxiliary coil, the magnet pole profile is designed from a quadrupole magnet, and the sextupole magnetic field is generated by a sextupole coil on the pole face and a dipole correction coil around the pole. The quadrupole magnetic field and sextupole magnetic field can be adjusted separately. However, the structure is complicated and requires three independent power sources. As for the magnet using pole profile adjustment, the pole profile is a superimposition of the quadrupole and sextupole equipotential surfaces, which represents that the quadrupole and sextupole fields are adjusted in the design stage and fixed. Therefore, it is not compatible with flexible optics that changes in the operation.

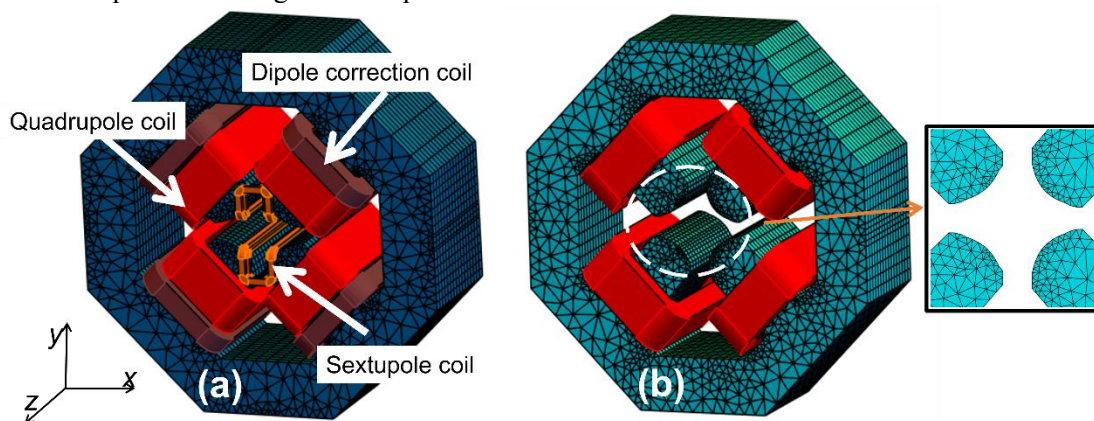


FIGURE 1. Combined-function quadrupole-sextupole magnets (a) with using auxiliary coil and (b) with pole profile adjustment.

To reduce the operation cost, we are also considering using an electrical/permanent hybrid magnet for energy saving [4]. The magnetomotive force is mainly generated by the permanent magnet material. The coil is assembled to provide part of magnetomotive force and adjust magnetic field strength. Such a kind of magnet can save the costs for electrical power. In addition, the magnet can get rid of water-cooling system of the coil because of a low current density. However, permanent magnets are difficult to achieve high precision and easy adjustability of the field strengths. Furthermore, there are other issues such as temperature dependence and demagnetization caused by radiation. We also found that the existence of the PM in the magnetic circuit produces a large magnetic resistance against the magnetomotive force produced by the coil. To solve this issue, we continue careful design study on the magnet configuration.

In order to apply the hybrid permanent magnet to HiSOR-II, the thermal effect compensation is being studied by using a permanent dipole magnet developed at Nagoya University [5]. In the experiment, it is

observed that the variation of the dipole field strength is almost proportional to the temperature of the Permanent Magnet (PM), as shown in Figure 2.

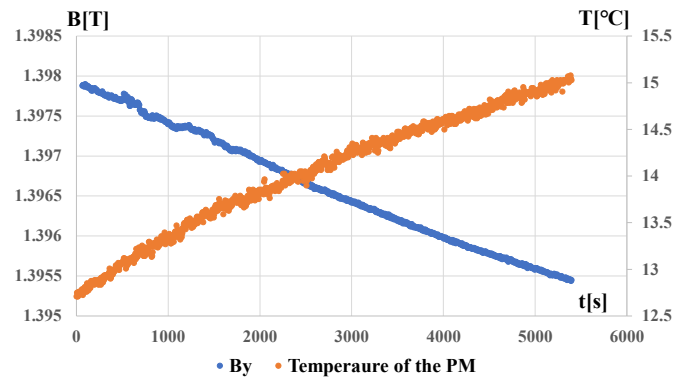


FIGURE 2. Variation of the B_y and temperature of the PM when current density is $2\text{A}/\text{mm}^2$.

A feedback control system for the magnetic field correction were tested. The drift of magnetic field is less than 0.0002 T (0.014%). In the future, the performance of the feedback system will be improved by increasing the precision of the measurement of the magnetic field and temperature.

REFERENCES

1. M. Katoh *et al*, "Upgrade plan for UVSOR," in *Proc. of the 2th Asian. Part. Accel. Conf*, Beijing, China, 2001.
2. W. Beeckman, *et al*, in *Proc. PAC2013*, Pasadena, CA USA, pp. 1229-1231.
3. <http://www.esrf.eu/Accelerators/Groups/InsertionDevices/Software/Radia>
4. G. Tosin, *et al*, *Nuclear Instruments and Methods in Physics Research A* 674 (2012) 67–73.
5. S. Fukue, *et al*, in *Proc. of the 13th annual meeting of PASJ*, August 2016, Chiba, Japan.

Experimental Study on Single Electron Storage

Y. Asai^a, H. Miyauchi^{b, c}, M. Shimada^{b, c} and M. Katoh^{b, d}

^aGraduate School of Advanced Science and Engineering Hiroshima University, 1-3-1 Kagamiyama Higashi-Hiroshima 739-8526, Japan

^bHiroshima Synchrotron Radiation Center (HSRC), Hiroshima University 2-313 Kagamiyama Higashi-Hiroshima 739-0046

^cHigh Energy Accelerator Research Organization (KEK), 1-1 Oho Tsukuba 305-0801, Japan

^dUVSOR Synchrotron Facility, 38 Nishigo-Naka Myodaiji Okazaki 444-8585, Japan

Keywords: electron, photon, undulator, synchrotron radiation, quantum mechanics

We have started single electron storage experiments at UVSOR since 2021 with the aim of conducting fundamental research on electromagnetic radiation. At BL1U, we extracted undulator light in the UV region at a wavelength of 355 nm into the atmosphere and observed its intensity by a photomultiplier tube, as reducing background light using appropriate band-pass filters, and decreased the electron beam intensity using a beam scraper. We succeeded in observing a step-function-like intensity change under a small number of electron storage conditions with a good SN ratio and in confirming the single electron storage. In 2022, we improved the method of observing the accumulation state of single electron and attempted to observe undulator radiation from single electron.

This study utilizes an insertion device called a tandem undulator, which consists of two undulators arranged in series. It is known that the synchrotron radiation from the tandem undulator shows a finely modulated spectrum with the envelope of that from one undulator, as shown in Fig. 1 [1]. This modulation is the result of the spectral interference between the radiation from two undulators.

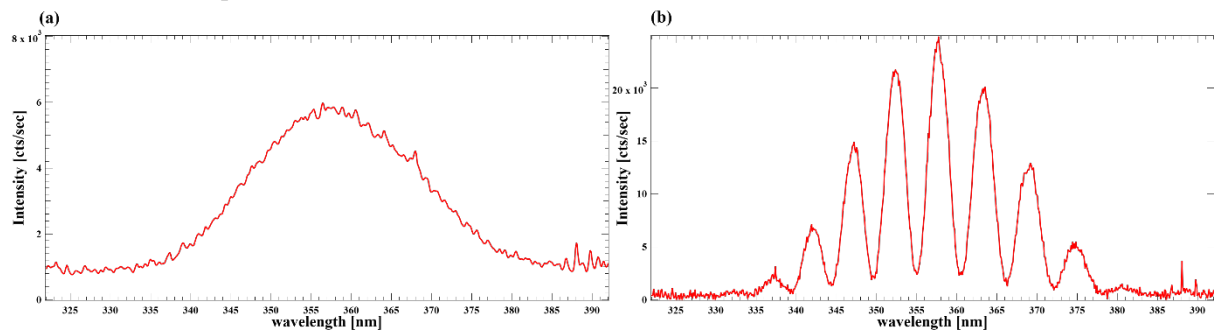


FIGURE 1. Spectra at a low beam current $I_b = 0.1$ mA; (a) from single undulator and (b) from tandem undulator.

The number of photons emitted during single passage of an electron in the undulator is much less than unity, which is in the same order of fine structure constant. Then, we have a question that when the single electron radiate single photon in the tandem undulator, does the spectrum shows the modulation? This is similar to Young's interference experiment but in the time domain. We have conducted such an experiment at UVSOR BL1U. The latest result from the experiment will be presented at the symposium.

REFERENCES

1. M. Billardon *et al.*, *J. Phys. Colloques* **44**, 1983, pp. 29-71

Diffraction of Optical Vortex from Undulator

Yu Nishihara^a, Miho Shimada^{c,b}, Hiroshi Miyauchi^{c,b}, Koichi Matsuo^{b,a},
Masahiro Katoh^{b,a,d}

^a*School of Science, Hiroshima University, 1-3-1 Kagamiyama Higashi-Hiroshima 739-8526, Japan*

^b*Hiroshima Synchrotron Radiation Center (HSRC), Hiroshima University 2-313 Kagamiyama
Higashi-Hiroshima 739-0046*

^c*High Energy Accelerator Research Organization (KEK), 1-1 Oho Tsukuba 305-0801, Japan*

^d*UVSOR Synchrotron Facility, 38 Nishigo-Naka Myodaiji Okazaki 444-8585, Japan*

Keywords: Undulator, Synchrotron radiation, Optical vortex, Diffraction.

It has been theoretically shown that radiation from an electron in circular motion with a relativistic speed has vortex property. Electron motion in a helical undulator radiation may be regarded as combination of mildly relativistic circular motion and ultra-relativistic drift motion along the rotation axis which is identical with the undulator axis. Therefore, helical undulator radiation has vortex property such that the fundamental component is circularly polarized plane wave and the higher harmonics are circularly polarized but optical vortex with helical wavefront. When we apply undulator vortex radiation to some experiments, it is desirable to observe the helicity and the topological charge of the vortex beam at various position in the beam-line. It is well known that optical vortex shows interesting diffraction patterns for various apertures. We can get information on the vortex property from the diffraction patterns. Among these, diffraction from triangular aperture seemed most feasible for our purpose.

To make a systematic study on the triangular diffraction, we have prepared triangular aperture of several size. The experiment was carried out at BL1U of UVSOR-III storage ring. This beam-line equipped with APPLE-II type undulator. By setting it in the helical mode with the fundamental wavelength at 710nm, the second harmonic radiation at 355 nm was extracted to the air. By using conventional CCD Camera, we made observation on the diffraction pattern. Some of the results are shown in Figure 1. We succeeded in observing the characteristic pattern which shows the helicity and the topological charge. Some more details on the experimental results will be presented in the symposium.

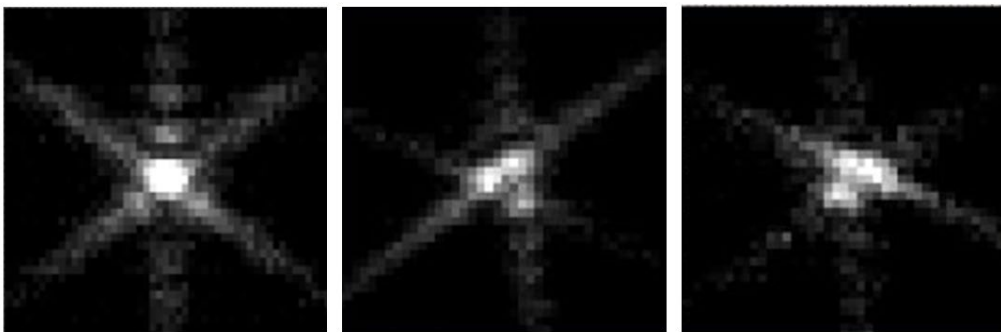


FIGURE 1. Diffraction by triangular aperture of helical undulator radiation observed at UVSOR BL1U, for 1st harmonic (left) and 2nd harmonic radiation (center and right, the helicity is reversed). The wavelength is centered at 355nm.

20AU018, 22AG005, 22BG004

BL-9A

Unexpected two-fold symmetry of the electronic structure in heavily overdoped Bi2201 observed by angle-resolved photoemission spectroscopy

Y. Miyai^a, S. Ideta^b, T. Kurosawa^c, M. Oda^d, K. Tanaka^e, M. Arita^b
and K. Shimada^b

^aGraduate School of Advanced Science and Engineering, Hiroshima University, Higashi-Hiroshima 739-8526, Japan

^bHiroshima Synchrotron Radiation Center, Hiroshima University, Higashi-Hiroshima 739-8526, Japan

^cFaculty of Science and Engineering, Muroran Institute of Technology, Muroran 050-8585, Japan

^dDepartment of Physics, Hokkaido University, Sapporo 060-0809, Japan

^eUVSOR-III Synchrotron, Institute for Molecular Science, Okazaki 444-8585, Japan

Keywords: High- T_C superconductor, ARPES

High transition-temperature (T_C) cuprate superconductors have attracted much interest since their discovery in 1986 for their high T_C as well as unusual physical properties such as a pseudogap [1] and a Nematicity [2]. Superconductivity occurs in the CuO_2 plane and the $\text{Cu } 3d_{x^2-y^2}$ state forms the Fermi surface (FS). It has been widely believed that the CuO_2 plane is four-fold symmetric so far. Recently, however, symmetry reduction of the electronic structure has been reported in Bi-based cuprate superconductors [2,3]. Note that the breaking of the four-fold rotational symmetry or nematicity has been also found in the electronic structure of iron-based superconductors [4]. Although the nematicity in electron liquid has attracted much interest, the rotational symmetry breaking in the electronic structure of high- T_C cuprate superconductors has not been directly clarified yet.

In this study, we examined the symmetry of the electronic structure of the cuprate superconductors using high-resolution angle-resolved photoemission spectroscopy (ARPES). Here, as a suitable system for this study, we have selected heavily overdoped Bi-based high- T_C cuprates, $(\text{Bi,Pb})_2\text{Sr}_2\text{CuO}_{6+\delta}$ (Pb-Bi2201) because it has a single CuO_2 plane in the unit cell and the superstructure reflections are suppressed by Pb doping. Furthermore, the pseudogap disappears in the heavily overdoped sample and one can clearly see the entire FS in the normal state.

By mechanically rotating the sample, we found the difference of nodal distances for the two nodal directions (#1 and #2 in the inset of Fig. 1(a)) at the Fermi level (E_F). The two-fold symmetry was obvious if we compared the observed FS with the four-fold symmetric theoretical FS given by the tight-binding model. In addition, the ARPES spectral intensities at the E_F were different for these two nodal directions. To further examine many-body interactions, we have evaluated self-energies ($\Sigma^{(\#1)}, \Sigma^{(\#2)}$) as shown in Figs. 1(a) and 1(b) along the two nodal directions #1 and #2 in the inset of Fig. 1(a). Since the experimentally extracted real and imaginary parts of the self-energies satisfy the Kramers-Kronig relation, the two-fold anisotropy should be intrinsic, indicating that the many-body interactions such as the electron-electron and the electron-boson (phonon) interactions are anisotropic in these two nodal directions. Note that the observed symmetry breaking of the electronic structure is independent of temperature in the range used in this study (20 – 260 K).

The two-fold symmetry of the electronic structures in the heavily overdoped Pb-Bi2201 may be related to a charge order formation in heavily overdoped Pb-Bi2201 as observed by resonant inelastic X-ray scattering [5]. Our results provide an insight for the intriguing physical properties such as the nematicity [2]

and the ferromagnetic fluctuation [6] of the heavily overdoped Bi2201.

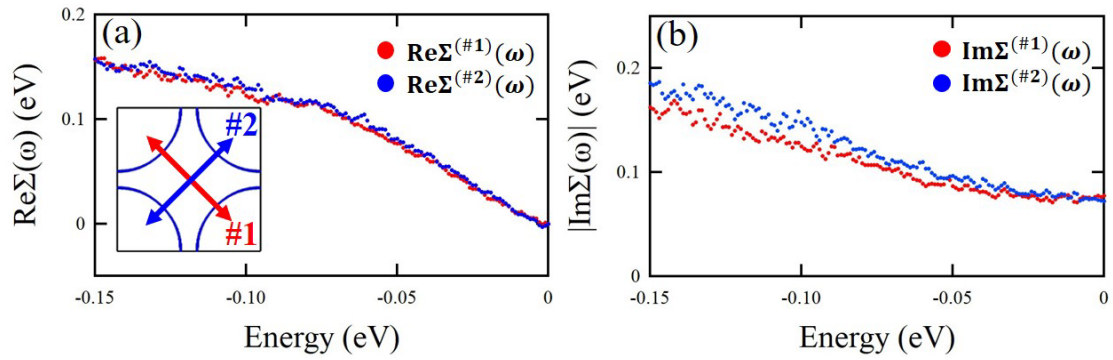


FIGURE 1. (a), (b) Experimentally obtained self-energy (Σ) along the orthogonal two nodal directions. Red and blue dots indicate $\Sigma^{(\#1)}$ and $\Sigma^{(\#2)}$ extracted from #1 and #2 directions as shown in the inset of panel (a) respectively.

1. M. Hashimoto *et al.*, *Nature Physics* **10**, 483 (2014).
2. S. Nakata *et al.*, *npj Quantum Materials* **6**, 86 (2021).
3. N. Auvray *et al.*, *Nature Communications* **10**, 5209 (2019).
4. H. C. Xu *et al.*, *Physical Review Letters* **117**, 157003 (2016).
5. Y. Y. Peng *et al.*, *Nature Materials* **17**, 697 (2018).
6. K. Kurashima *et al.*, *Physical Review Letters* **121**, 057002 (2018).

Comprehensive Studies of the Electronic Structure for the Double-layer high- T_c Superconductor $\text{Bi}_2\text{Sr}_2\text{CaCu}_2\text{O}_{8+\delta}$ - Revisit of the Phase Diagram by ARPES

Y. Tsubota^a, Y. Miyai^b, S. Kumar^{b,c}, K. Tanaka^d, S. Ishida^e, H. Eisaki^e, S. Nakagawa^f, T. Kashiwagi^f, M. Arita^b, K. Shimada^{a,b}, and S. Ideta^{a,b}

^a Graduate School of Advanced Science and Engineering, Hiroshima Univ., Higashi-Hiroshima 739-0046, Japan

^b Hiroshima Synchrotron Radiation Center (HiSOR), Hiroshima Univ., Higashi-Hiroshima 739-0046, Japan

^c Institute of Microelectronics (IME), Agency for Science, Technology and Research (A*STAR), Singapore 138632, Singapore

^d UVSOR-III Synchrotron, Institute for Molecular Science, Okazaki, Aichi 444-8585, Japan

^e National Institute of Advanced Industrial Science and Technology (AIST), Tsukuba, Ibaraki 305-8560, Japan

^f Division of Materials Science, Tsukuba University, Tsukuba, Ibaraki 305-8577, Japan

Keywords: high- T_c cuprate superconductors, ARPES, electronic structure, strongly correlated electron materials

It has been known that the cuprate superconductors show a high superconducting (SC) transition temperature (T_c) and exotic physical properties. However, the SC mechanism of cuprates has been unclear yet. In order to understand the mechanism of the microscopic origin of the high- T_c cuprate, various theoretical and experimental studies have been done so far [1]. In high- T_c cuprate superconductors, superconductivity occurs by hole doping into the CuO_2 plane. The superconducting transition temperature T_c as a function of hole concentration was reported as schematically shown in Fig. 1 [2]. For the hole-doped cuprate superconductors, it has been widely believed that the phase diagram is universal, and the highest T_c occurs at the hole concentration of ~ 0.16 . However, recent angle-resolved photoemission spectroscopy (ARPES) experiments indicated that the empirical phase diagram may not be universal and shifted toward the overdoped region [3-5].

In this study, we have performed ARPES measurements systematically to directly investigate the electronic structure of the underdoped, optimally doped, and overdoped regions with three different compositions of the double-layer cuprate, $\text{Bi}_2\text{Sr}_2\text{CaCu}_2\text{O}_{8+\delta}$ (Bi2212). We have estimated the hole concentration of each sample from the Fermi-surface area and compared them quantitatively. Fig. 1 shows the Fermi surface of the optimally doped Bi2212 with $T_c = 92$ K and determined the Fermi momentum (red dots in Fig. 1) from the ARPES lineshape analyses.

In this poster presentation, we will show the results of the hole concentration estimated from the Fermi surfaces in Bi2212 for each sample and are compared with the previous study to understand the relationship between the hole concentration and T_c , namely, the new phase diagram. In this study, we found that the phase diagram differs from the reported one [2]; the maximum T_c shifts toward the overdoped region. Furthermore, we have measured the electronic structure in which the pseudogap closes and verified its consistency with respect to the carrier concentration below and above T_c . Based on the present ARPES study, we will show the new phase diagram in Bi2212 and discuss the results in comparison with other studies [6,7].

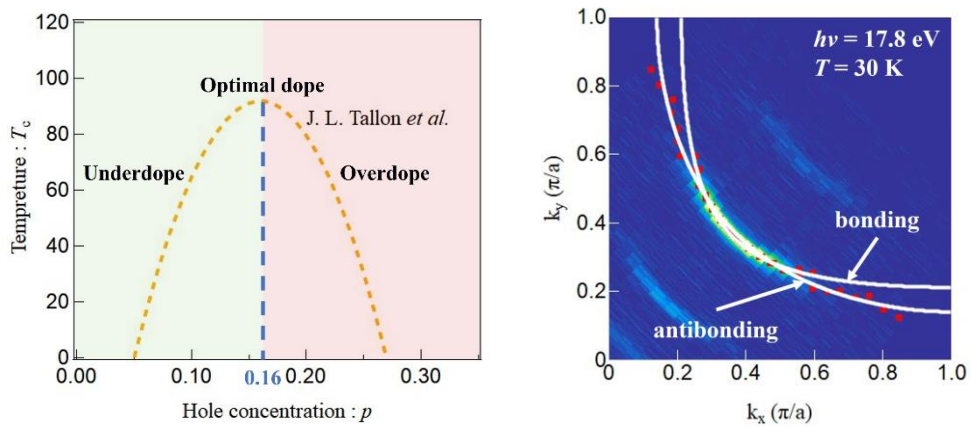


FIGURE 1. Schematic phase diagram reported from Ref. [2] (left). Fermi surfaces of Bi2212 observed by ARPES (right). Red dots indicate the Fermi momentum estimated from the momentum-distribution curves near the Fermi level. White curves are the Fermi surfaces fitted by tight-binding model. The bonding and antibonding bands are shown by the white curves, respectively.

REFERENCES

1. B. Keimer *et al.*, *Nature* **518**, 179-186 (2015).
2. J. L. Tallon *et al.*, *Phys. Rev. B* **51**, 12911(1995).
3. H. Sakamoto *et al.*, *J. Phys. Soc. Jpn.* **85**, 104710(2016).
4. I. K. Drozdov *et al.*, *Nat. Commun.* **9**, 5210(2018).
5. R. Sobota *et al.*, *J. Phys. Soc. Jpn.* **88**, 064711(2019).
6. I. M. Vishik *et al.*, *Proc. Nat. Acad. Sci.* **109** (45), 182-18337 (2012).
7. S-D. Chen, *et al.*, *Science* **366**, 1099–1102 (2019).

Probing the Electronic Band Structure of Altermagnetic MnTe: An ARPES Study

Kazi Golam Martuza^a, Yogendra Kumar^a, Shiv Kumar^{b,c}, Shin-ichiro Ideta^{a,b} and Kenya Shimada^{a,b}

^aGraduate School of Advanced Science and Engineering, Hiroshima University, Japan 739-0046

^bHiroshima Synchrotron Radiation Centre (HiSOR), Hiroshima University, Japan 739-0046

^cInstitute of Microelectronics, Agency for Science, Technology and Research (A*STAR), Singapore

Keywords: MnTe, altermagnet, electronic structure, ARPES

Altermagnetism is a recently recognized type of magnetism with vanishing net magnetization and a time-reversal symmetry broken electronic structure and have attracted much interest for their distinct magnetic characteristics and prospective applications [1]. As a canonical altermagnetic material, MnTe has garnered a lot of interest recently [2-6]. MnTe with a hexagonal NiAs-type structure is one of the few semiconductors among the 3d transition-metal compounds [3,4].

In this study, we investigated the electronic band structure of the hexagonal MnTe (0001) bulk single crystal using polarization dependent angle-resolved photoemission spectroscopy (ARPES). The samples were prepared by mixing stoichiometric amounts of finely powdered Mn and Te and sealed in evacuated quartz ampoule at 10^{-5} pa. We grew MnTe single crystal by solid reaction method and cut it to exhibit the (0001) plane. For getting clean surface we sputtered and annealed the sample. We used 2kV beam energy for sputtering and annealing temperature was 330 degree Celsius. By repeated cycles of sputtering and annealing, we could finally get a clean surface. The impurity of the surface was checked by the Auger electron spectroscopy and the long-range order was confirmed by the sharp hexagonal low-energy electron diffraction (LEED) spots. The polarization dependent ARPES experiments were done on HiSOR BL-9A equipped with an ASTRAIOS electron analyzer. We set the photon energy at 40 eV and the temperature at 200K. The polarization direction of the incident light was controlled by the undulator magnets configuration.

Figs. 1(a) and 1(b) show the k_x - k_y ARPES intensity map at the chemical potential taken with the s- and p-polarization geometries, respectively. Although MnTe is a semiconductor, due to the intrinsic hole doping, the chemical potential is located below the top of the valence band. The photoemission intensity is much intense taken at the s-polarization geometry indicating that the electron wave functions are odd with respect to the mirror plane. It indicates the observed valence bands are derived from Mn $3d_{xy}$, Mn $3d_{yz}$, and Te $5p_y$ states. The spectral intensity is strong around the $\bar{\Gamma}$ point and the ARPES intensity map along the $\bar{\Gamma}\bar{K}$ direction in Fig. 1(c) suggests an existence of hole-like bands, which is consistent with the band-structure calculations [5,7]. The ARPES intensity mapping at the chemical potential in Fig. 1(a) is compatible with the hexagonal (0001) surface.

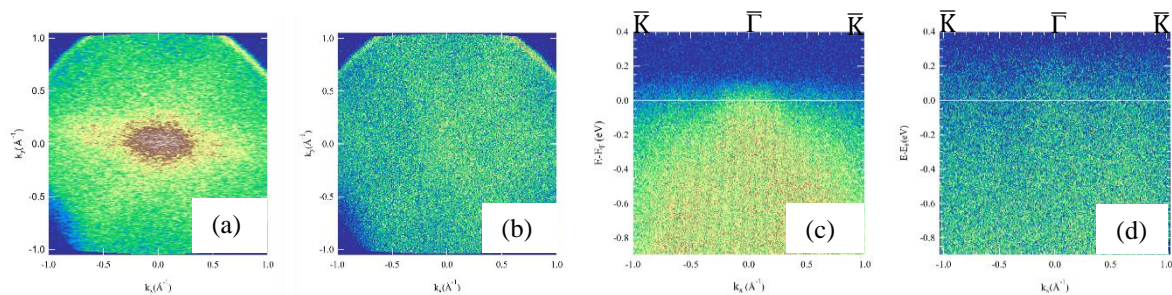


FIGURE 1. High-resolution ARPES results on MnTe (0001) single crystal taken at 200K and $h\nu=40$ eV. k_x - k_y mapping at the chemical potential with the s-polarization (a) and p-polarization (b) geometries. ARPES intensity map along the $\bar{\Gamma}\bar{K}$ high symmetry line with the s-polarization (c) and p-polarization (d) geometries.

REFERENCES

- [1] S. Lee *et al.*, Phys. Rev. Lett. **132**, 036702 (2024).
- [2] S. Mu *et al.*, Phys Rev Mater. **3**, 025403 (2019).
- [3] De Melo *et al.*, Journal of Crystal Growth **110**, 445-451 (1991).
- [4] H. Sato *et al.*, Journal of Magnetism and Magnetic Materials **140-144**, 153-154 (1995).
- [5] P. E. Faria Junior *et al.*, Phys. Rev. B **107**, L100417 (2023).
- [6] T. Osumi *et al.*, <http://arxiv.org/abs/2308.10117>.
- [7] S. J. Youn *et al.*, Physica Status Solidi (B) **241**, 1411–1414 (2004).

Effects of Quantum Charge Fluctuations on the Electron Self-energy of High- T_c Cuprate Superconductors Using Angle-Resolved Photoemission and Inverse Photoemission Spectroscopies

Y. Onishi^a, Y. Miyai^a, Y. Tsubota^a, K. Tanaka^c, S. Ishida^d, H. Eisaki^d,
H. Sato^b, M. Arita^b, K. Shimada^{a,b}, and S. Ideta^{a,b}

^a Graduate School of Advanced Science and Engineering, Hiroshima Univ., Higashi-Hiroshima 739-0046, Japan

^b Hiroshima Synchrotron Radiation Center (HiSOR), Hiroshima Univ., Higashi-Hiroshima 739-0046, Japan

^c UVSOR-III Synchrotron, Institute for Molecular Science, Okazaki, Aichi 444-8585, Japan

^d National Institute of Advanced Industrial Science and Technology (AIST), Tsukuba, Ibaraki 305-8560, Japan

Keywords: high- T_c superconductors, ARPES, IPES, charge fluctuations, electronic structure

In the previous studies of angle-resolved photoemission spectroscopy (ARPES), it has been reported that kink structures are observed in the electronic structure for the cuprates likely due to spin fluctuations and/or phonons [1-3]. This observation indicates that the glue of the Cooper pair is magnons or phonons. On the other hand, in recent years, resonant inelastic x-ray scattering experiments have been performed in the hole- and electron-doped high- T_c cuprate superconductors and charge excitations are observed [4, 5]. In addition, theoretical calculations of unconventional high- T_c superconductors using the layered t - J model, which includes the long- and short-range Coulomb interactions with charge fluctuations, have been reported to study how charge fluctuations interact to the electronic structure in cuprates [6, 7]. However, the effect of charge fluctuations to the electronic structure of cuprates has not been studied by angle-resolved photoemission spectroscopy (ARPES) directly.

In this study, to investigate the role of charge fluctuations for the electronic structure in the high- T_c cuprate superconductor, $\text{Bi}_2\text{Sr}_{1.6}\text{La}_{0.4}\text{CuO}_{6+\delta}$ (Bi2201), we have performed ARPES and inverse photoemission spectroscopy (IPES) to study the occupied and unoccupied states, respectively. In the experiments, ARPES and IPES measurements are performed along high-symmetry lines in the Brillouin zone (Fig. 1, (a)). We found the shoulder structure near 1 eV above the Fermi level in the IPES spectra as shown by red area in Fig. 1 (b). In the poster presentation, we will show the details of the electronic structure on Bi2201 in the occupied and unoccupied states and discuss the effect of charge fluctuations on the electronic structure of high- T_c cuprate superconductors, including a comparison with theoretical calculations [6, 7].

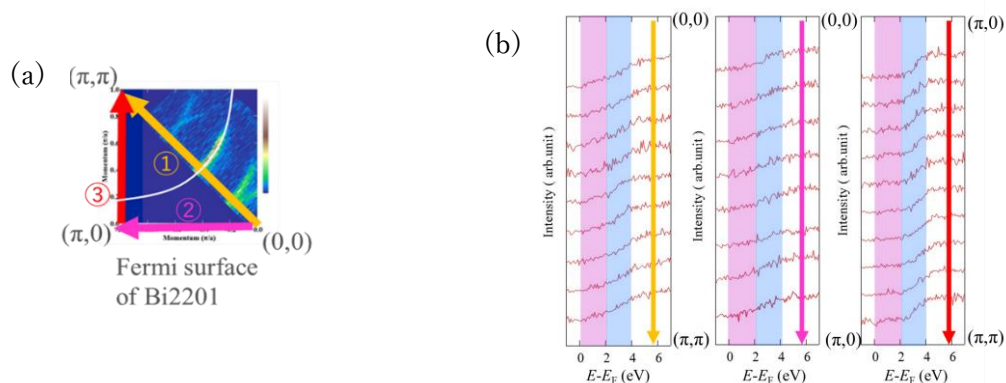


FIGURE 1. (a) The Fermi-surface on the Brillouin zone for Bi2201. Each arrow corresponds to the panel in the panel (b). (b) Energy-distribution curves in the second Brillouin zone ($T = 13\text{K}$, $E_{\text{kin}} = 50\text{eV}$).

REFERENCES

1. A. Lanzara *et al.*, Nature **412**, 510 (2001).
2. P. V. Bogdanov *et al.*, Phys. Rev. Lett. **85**, 2581 (2000).
3. S. M. Hayden *et al.*, Nature **429**, 531–534 (2004).
4. K. Ishii *et al.*, Phys. Rev. B **96**, 115148 (2017).
5. A. Singh *et al.*, Phys. Rev. B. **123**, 235105 (2022).
6. H. Yamase *et al.*, Phys. Rev. B **104**, 045141 (2021).
7. H. Yamase *et al.*, Commun Phys **6**, 168 (2023).

Observation of Topological Surface States and Non-symmorphic Band Degeneracy in Superconducting PdSeTe Single-crystal

Y. Kumar^a, S. Kumar^b, Y. Venkateswara^d, R. Oishi^a, J. Nayak^c, T. Onimaru^a, S. Ideta^{a,b}, K. Shimada^{a,b}

^aGraduate School of Advanced Science and Engineering, Hiroshima University, Japan 739-0046

^bHiroshima Synchrotron Radiation Centre (HiSOR), Hiroshima University, Japan 739-0046

^cDepartment of Physics, Indian Institute of Technology, Kanpur, India 208016

^dDepartment of Physics, SUNY Buffalo State University, New York, USA 14222

Keywords: Weyl semimetal, superconductivity, ARPES study, DFT calculation

Topological semimetals with topologically non-trivial band structures have been the focus of recent theoretical and experimental studies [1-3]. Dirac semimetals (DSMs), Weyl semimetals (WSMs), and topological nodal-line semimetals are the three main sub-categories of topological semimetals, which can be characterized according to the form and degeneracy of the band crossings near the Fermi level [4]. The layered transition metal chalcogenides among the DSMs and WSMs are particularly significant for their various intriguing physical properties, such as superconductivity and charge density wave (CDW) with application potentials [5].

In this study, we have successfully synthesized high-quality single crystals of PdSeTe which is a candidate of DSM by a two-step melting method and investigated the electronic band structure as well as the superconducting properties. We performed angle-resolved photoemission spectroscopy (ARPES) of PdSeTe on the beamline HiSOR BL-1. We have done the density functional theory (DFT) calculations and found that PdSeTe hosts four-fold degenerate Dirac crossings at the A point, originating from the non-symmorphic symmetry. These band crossings form a Dirac line node along the $\Gamma - A$ direction, which is located near the Fermi level and shows almost no energy dispersion. Therefore, Dirac fermions in PdSeTe can be studied using transport measurements. To verify the surface contribution in the ARPES results, we have done $h\nu$ -dependent measurements and directly confirmed the presence of surface states in PdSeTe. The observed surface-derived states match well with the DFT calculation for the slab model.

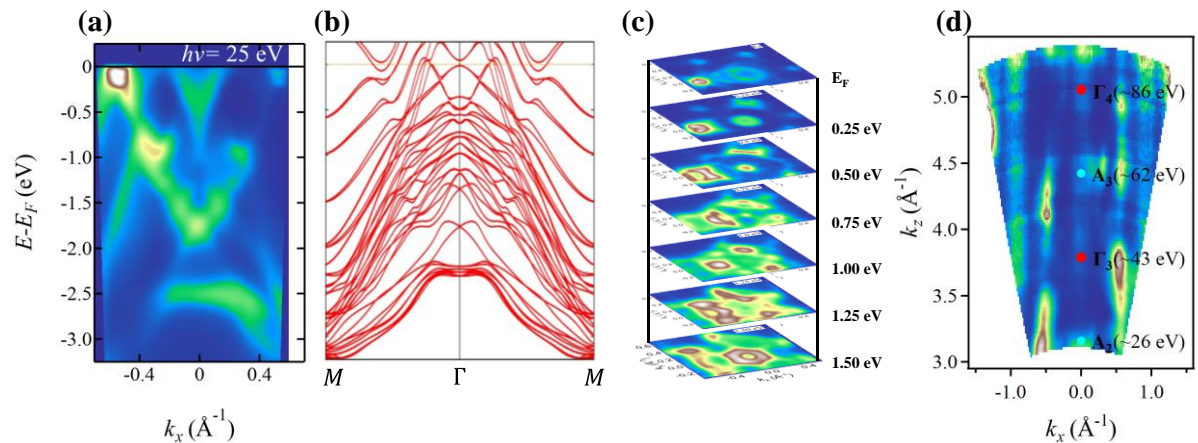


Fig. 1: (a) and (b) represent the measured ARPES spectrum along $\bar{M} - \bar{\Gamma} - \bar{M}$ direction with 25eV photon energy at 20K and simulated bands for slab (5 atomic layers) respectively. (c) The Fermi surface and constant-energy contours of the ARPES spectra at different binding energies. (d) The shows the experimental k_z -dispersion along $\bar{\Gamma} - \bar{A}$ deduced from the $h\nu$ -dependent data measured along the $\bar{M} - \bar{\Gamma} - \bar{M}$ direction.

REFERENCES

1. M.Z. Hasan, C.L. Kane, Reviews of Modern Physics **82**, 3045-3067 (2010).
2. X.-L. Qi, S.-C. Zhang, Reviews of Modern Physics **83**, 1057-1110 (2011).
3. Y. Xia et al., Nature Physics **5**, 398-402 (2009).

4. B. Yan, C. Felser, *Annual Review of Condensed Matter Physics* **8**, 337-354 (2017).
5. K. Kim, *et al.*, *PRB* **97**, 165102 (2018).

Strain-Induced Relocation of Topological Surface States in Bi_2Se_3 Single Crystal

Y. Kumar^a, S. Kumar^b, S. Ideta^{a,b}, T. Okuda^{a,b}, K. Shimada^{a,b}

^aGraduate School of Advanced Science and Engineering, Hiroshima University, Japan 739-0046

^bHiroshima Synchrotron Radiation Centre (HiSOR), Hiroshima University, Japan 739-0046

Keywords: Topological Insulator, *in-situ* Strain, ARPES, Dirac point, Straintronics.

To investigate the impact of strain on the surface and bulk electronic states of solids, we have developed a new sample holder for *in-situ* strain application for ARPES experiments at low temperatures. In this study, we report the design of the sample holder and ARPES results of a strain-induced modification of the surface and bulk states of Bi_2Se_3 single crystal. Our findings reveal significant alterations in the electronic band structure [6] (in terms of energy and momentum) of the Bi_2Se_3 layered topological insulator [1-4] when subjected to tensile strain. Specifically, tensile strain leads to a closer proximity of the Dirac point (DP) to the Fermi level (lower binding energy), while compressive strain results in the DP moving further away from the Fermi level (higher binding energy). This study demonstrates the tunability of both surface and bulk electronic states in Bi_2Se_3 through the *in-situ* application of strain and underscores the potential of strain engineering for “Straintronics” [5] devices. The sample holder developed for this purpose holds promise for advancing research on the electronic band structures of layered materials, including topological insulators and quantum materials [6-8], under strain conditions.

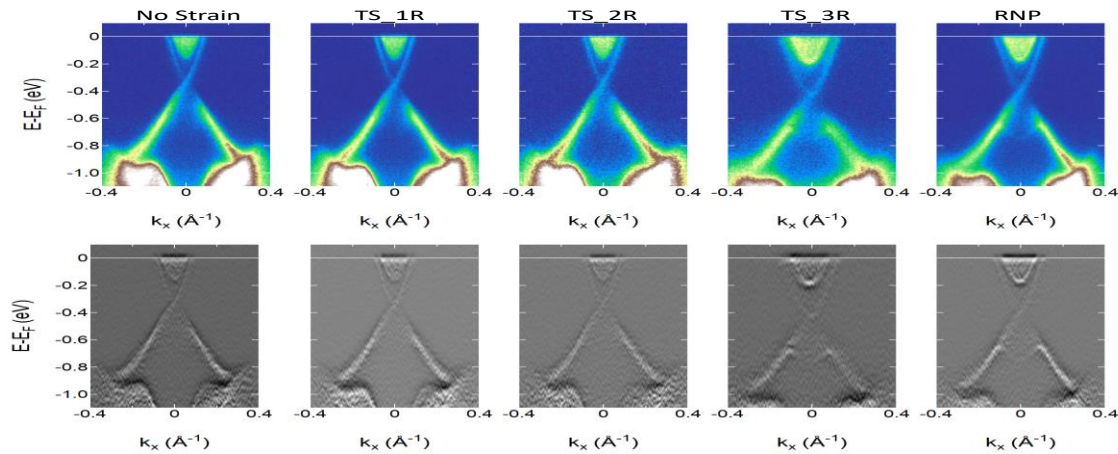


FIGURE 1. ARPES maps along $\bar{\Gamma} - \bar{K}$ for Bi_2Se_3 single crystal with increasing tensile strain (TS) from TS_1R, to TS_2R, to TS_3R measured at 10 K with 25 eV photon energy. The DP moves to the lower energy. The DP position was not recovered to the original position though we remove the tensile strain (RNP).

TABLE 1. Changes in fermi velocity, bottom of conduction band and shift in dirac point with respect to applied strain.

Change in parameters	No Strain	TS_1R	TS_2R	TS_3R	RNP
$k_F (\text{\AA}^{-1})$	0.0848	0.0846	0.0876	0.1037	0.1080
Bottom of conduction band (eV)	-0.1555	-0.1605	-0.1655	-0.1806	-0.1856
Dirac Point (eV)	-0.3398	-0.3520	-0.3584	-0.3729	-0.3862

REFERENCES

1. L. Fu, C.L. Kane, E.J. Mele, Topological Insulators in Three Dimensions, *Physical Review Letters* 98 (2007) 106803.
2. L. Fu, C.L. Kane, Topological insulators with inversion symmetry, *Physical Review B* 76 (2007) 045302.
3. M.Z. Hasan, C.L. Kane, Colloquium: Topological insulators, *Reviews of Modern Physics* 82 (2010) 3045-3067.
4. Y. Ando, Topological Insulator Materials, *Journal of the Physical Society of Japan* 82 (2013) 102001.
5. A.A. Bukharaev, A.K. Zvezdin, A.P. Pyatakov, Y.K. Fetisov, Straintronics: a new trend in micro- and nanoelectronics and materials science, *Physics-Uspekhi* 61 (2018) 1175.
6. S. Riccò, M. Kim, A. Tamai, S. McKeown Walker, F.Y. Bruno, I. Cucchi, E. Cappelli, C. Besnard, T.K. Kim, P. Dudin, M. Hoesch, M.J. Gutmann, A. Georges, R.S. Perry, F. Baumberger, In situ strain tuning of the metal-insulator-transition of Ca_2RuO_4 in angle-resolved photoemission experiments, *Nature Communications* 9 (2018).
7. I. Kostylev, S. Yonezawa, Z. Wang, Y. Ando, Y. Maeno, Uniaxial-strain control of nematic superconductivity in $\text{Sr}_x\text{Bi}_2\text{Se}_3$, *Nature Communications* 11 (2020) 4152.
8. E. Gati, L. Xiang, S.L. Bud'Ko, P.C. Canfield, Hydrostatic and Uniaxial Pressure Tuning of Iron-Based Superconductors: Insights into Superconductivity, Magnetism, Nematicity, and Collapsed Tetragonal Transitions, *Annalen der Physik* 532 (2020) 2000248.

Research of Charge Fluctuations in the Electron-doped High- T_c Cuprate NCCO Revealed by ARPES and IPES

H. Yamaguchi^a, Y. Onishi^b, Y. Miyai^b, Y. Tsubota^b, M. Atira^c, K. Tanaka^d,
H. Sato^c, D. Song^e, K. Shimada^{b,c}, S. Ideta^{b,c}

^a School of Science, Hiroshima Univ., Higashi-Hiroshima 739-0046, Japan

^b Graduate School of Advanced Science and Engineering, Hiroshima Univ., Higashi-Hiroshima 739-0046, Japan

^c Hiroshima Synchrotron Radiation Center (HiSOR), Hiroshima Univ., Higashi-Hiroshima 739-0046, Japan

^d UVSOR-III Synchrotron, Institute for Molecular Science., Okazaki, Aichi 444-8585, Japan

^e Stewart Blusson Quantum Matter Institute, University of British Columbia, Vancouver, BC V6T1Z4, Canada

Keywords: cuprate superconductors, charge fluctuation, electronic structure, ARPES, IPES

The origin of the high- T_c superconductivity has been extensively studied so far, but the bosonic interaction to form electron pairs is still elusive. There are three degrees of freedom in the solid; orbital, charge, and spin [1]. According to the previous experimental reports [2-8], the promising candidates of the bosonic interactions are phonons and magnons. On the other hand, the role of the charge fluctuation in the high- T_c superconductivity is not well understood.

Recently, inelastic X-ray scattering experiments reported that charge excitations for both hole- and electron-doped cuprate high- T_c superconductors [9-11], and therefore, the effect of the charge fluctuation to the high- T_c superconductivity has attracted interest. According to the theoretical study [12], using the layered t - J model, the electron self-energy is calculated and discussed about the effect of charge fluctuation in the spectral function.

We have performed an ARPES and inverse photoemission spectroscopy (IPES) to observe the electronic structure in the occupied and unoccupied states, respectively, on $\text{Nd}_{1-x}\text{Ca}_x\text{CuO}_4$ ($x = 0.15$) as shown in Fig. 1. We find that a strong peak structure exists in the energy region between 5 and 9 eV above the Fermi level (E_F). In the poster presentation, we will show the details about the experimental data and discuss the effect from the charge fluctuation.

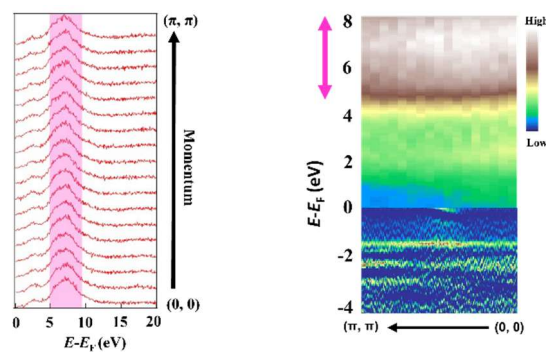


FIGURE 1. Experimental data observed by ARPES and IPES. Energy-distribution curves observed by IPES in the direction of $(0, 0)$ - (π, π) is shown on the left side. On the right side, IPES spectra without the second derivative (above E_F) and the second-derivative intensity plot observed by ARPES (below E_F) is shown.

REFERENCES

1. H. Hwang *et al.*, Nat. Mater. **11**, 103-113 (2012).
2. A. Lanzara *et al.*, Nature **412**, 510 (2001).
3. J. P. Carbotte *et al.*, Nature **401**, 354 (1999).
4. H. F. Fong *et al.*, Phys. Rev. Lett. **75**, 316 (1995).
5. L. Braicovich *et al.*, PhysRevLett. **104**, 077002 (2010).
6. M. Le Tacon *et al.*, Nature Phys **7**, 725-730 (2011).
7. J. Schlappa *et al.*, Nature **485**, 82-85 (2012).
8. M. P. M. Dean *et al.*, Nature materials **12**,1019-1023 (2013).
9. J. Lin *et al.*, npj Quantum Mater. **5**, 4 (2020).
10. A. Singh *et al.*, Phys. Rev. B **105**, 235105 (2022).
11. W. S. Lee *et al.*, Nature Phys **10**, 883-889 (2014).
12. H. Yamase *et al.*, Phys. Rev. B, **104**, 045141 (2021).

XPS study on the boron-doped amorphous carbon films

Yuji Muraoka^a, Kota Matuso^b, Takanori Wakita^a and Takayoshi Yokoya^a

^a*Research Institute for Interdisciplinary Science, Okayama University,
3-1-1 Tsushima-naka, Tsushima, Kita-ku, Okayama 700-8530, Japan*

^b*Graduate School of Natural Science and Technology, Okayama University,
3-1-1 Tsushima-naka, Tsushima, Kita-ku, Okayama 700-8530, Japan*

Keywords: XPS, Boron dope, Amorphous carbon, Film

Heavily boron (B)-doped amorphous carbon, which is called as B-doped Q-carbon, shows the superconductivity with a superconducting transition temperature of 55K [1,2]. Since B-doped Q carbon is the first example of amorphous semiconductor showing the superconductivity, much efforts have been devoted to preparing this material. However, preparation of this material is quite difficult because of its metastable form achieved by the nano-second pulsed laser annealing to the B-doped amorphous carbon precursors. So far, B-doped Q-carbon has not yet been reproduced. One of important studies related to the preparation of B-doped Q-carbon is to characterize the B-doped amorphous carbon precursors. Especially, the chemical states of B-doped amorphous carbon may affect the formation of the B-doped Q-carbon. In this study, we investigate the chemical states of carbon and boron atoms in the B-doped amorphous carbon precursors with different nominal boron content by means of an X-ray photoemission spectroscopy.

The B-doped amorphous carbon precursors were fabricated by a pulsed laser deposition method with a KrF excimer laser ($\lambda = 248\text{nm}$). Single crystal $\text{Al}_2\text{O}_3(0001)$ substrates were used for the film deposition. The deposition was performed under the vacuum condition of 3.0×10^{-6} Pa. Nominal boron content in the films was varied by changing the B/C ration in the target materials. The film thickness of the obtained precursor films was 200 to 300 nm. X-ray photoemission spectroscopy (XPS) measurements were carried out on the beamline BL-5, at the Hiroshima Synchrotron Radiation Center in Hiroshima University with non-monochromatic Mg $K\alpha$ X-ray source ($h\nu = 1253.6$ eV). C 1s and B 1s core-level spectra were measured under an ultrahigh vacuum of $\sim 10^{-7}$ Pa using a VSW hemispherical analyzer. The total energy resolution was about 1.8 eV. The binding energy of the films was corrected using the peak position of molybdenum spectra. Before measurements, the films were annealed at 100 °C under ultrahigh vacuum ($\sim 10^{-6}$ Pa) for 1 h to clean the film surface.

Figure 1 shows the C 1s core-level spectra of B-doped amorphous carbon films with different B content. The peak at 285 eV is observed for the non-doped films. This peak position shifts toward lower binding energy side with increasing boron content. Figure 2 shows the B 1s core-level spectra of B-doped amorphous carbon films with different B content. The peak structure appears as the nominal boron content is increased, indicating that boron atoms are present in the films. The B/C ratio of the films is estimated from the peak area ratio of C 1s and B 1s spectra to be 0-0.27. The peak position is located at 189 eV, which originates from B^0 states [3]. This indicates that most of boron atoms exist as an elemental state in the films. The reason for the shift of the C 1s spectra with increasing B content is probably due to the surface bending effect. It will be interesting to see how the chemical states of carbon and boron atoms change after pulsed laser annealing. Our present results provide an important starting point for obtaining the B-doped Q-carbon.

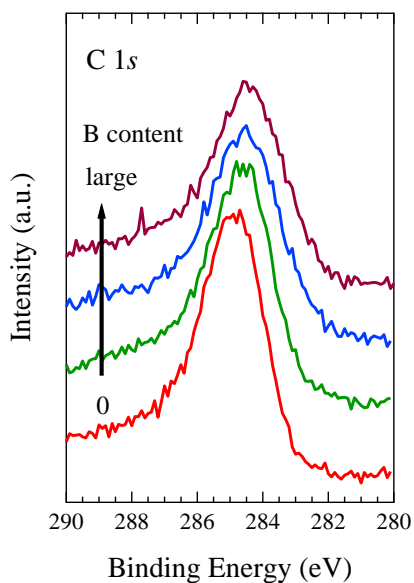


FIGURE 1. C 1s core-level spectra of boron-doped amorphous carbon films with different boron content.

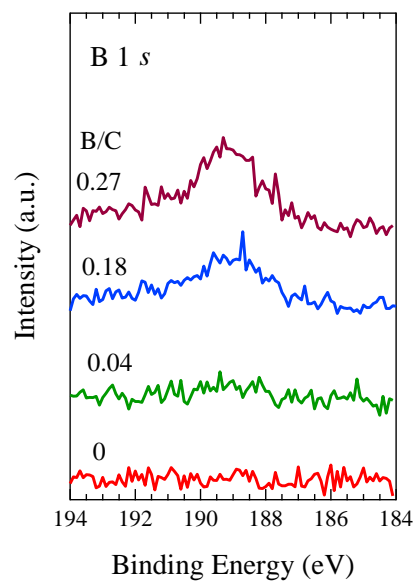


FIGURE 2. B 1s core-level spectra of boron-doped amorphous carbon films with different boron content.

REFERENCES

1. A. Bhaumik, R. Sachan, and J. Narayan, *ACS Nano*, **11**, 5351-5357 (2017).
2. A. Bhaumik, R. Sachan, S. Gupta, and J. Narayan, *ACS Nano*, **11**, 11915-11922 (2017).
3. W. G. Shin, H. J. Jung, H. G. Sung, H. S. Hyun, and Y. Sohn, *Ceram. Int.* **40**, 11511-11517 (2014).

Synchrotron ARPES studies of nodal line semimetal $\text{LaTe}_{1+x}\text{Bi}_{1-x}$

Ryusei Saito^a, Yuta Okishi^a, Tomoki Higashikawa^a, Takanori Wakita^{a,b},
Yogendra Kumar^c, Yudai Miyai^c, Haruka Kageyama^a, Ryusuke Kondo^a,
Yoshio Nogami^a, Shinichiro Ideta^c, Kenya Shimada^c, Yuji Muraoka^{a,b},
Takayoshi Yokoya^{a,b}

^aGraduate School of Natural Science and Technology, Okayama University, Okayama 700-8530, Japan

^bResearch Institute for Interdisciplinary Science, Okayama University, Okayama 700-8530, Japan

^cHiroshima Synchrotron Radiation Center, Hiroshima University, Higashi-Hiroshima 739-0046, Japan

Keywords: Topological material, Nodal line semimetal, Band dispersion, ARPES

$\text{LaTe}_{1+x}\text{Bi}_{1-x}$ is a layered material consisting of an insulating layer of LaTe and a conducting Bi square lattice layer. Band calculation predicted that it possesses a Dirac nodal-line along Γ -R in the Brillouin zone (BZ) (Fig. 1) [1], and therefore it can be classified as a nodal line semimetal for which exotic transport properties can be expected [2]. However, predicted nodal line of LaTeBi is located slightly above the Fermi level (E_F). To experimentally observe the nodal line and also determine its energy position relative to E_F are important to investigate the potential of $\text{LaTe}_{1+x}\text{Bi}_{1-x}$ to exhibit topological physical properties. In this presentation, we report synchrotron angle-resolved photoemission spectroscopy (ARPES) study of $\text{LaTe}_{1+x}\text{Bi}_{1-x}$, which was performed to directly observe the valence band electronic structure of $\text{LaTe}_{1+x}\text{Bi}_{1-x}$.

The samples measured were $\text{LaTe}_{1+x}\text{Bi}_{1-x}$ ($x = 0.2$) single crystals prepared by the flux method. Synchrotron ARPES experiments were performed by a high-resolution ARPES spectrometer at BL-1 of HiSOR, with linearly polarized light and with the light spot size of 40 (H) x 50 (V) μm . The energy resolution was set to ~ 40 meV and the measurement temperature was 20 K.

Figure 1 shows an ARPES intensity map measured along the Γ X line of the BZ. The black regions correspond to bands. Distinct dispersive bands symmetric with respect to the high symmetry points are clearly observed in the entire energy region shown. The observed bands were found generally consistent with the results of band calculations. Around X, one can find bands approaching E_F .

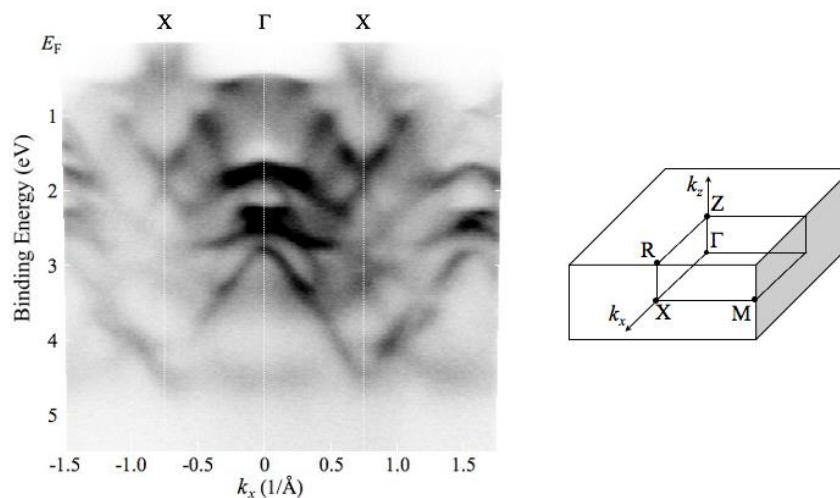


FIGURE 1. ARPES intensity map of $\text{LaTe}_{1.2}\text{Bi}_{0.8}$ and Brillouin zone

Figure 2 shows a minus second-derivative ARPES intensity map near E_F and around X. “W” shaped dispersive bands symmetric with respect to X are observed. The characteristic dispersion is consistent with calculation, indicating that a nodal line is located very close to E_F at X in $\text{LaTe}_{1.2}\text{Bi}_{0.8}$.

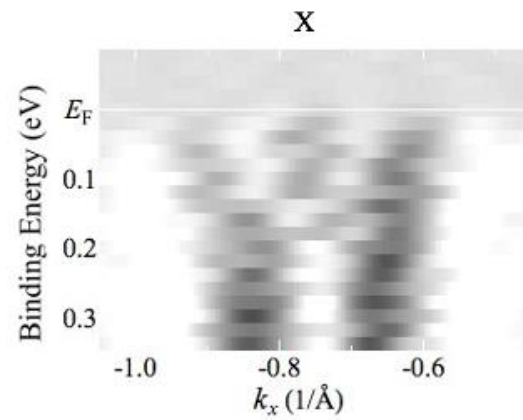


FIGURE 2. Minus second-derivative ARPES intensity map near E_F and around X of $\text{LaTe}_{1.2}\text{Bi}_{0.8}$

REFERENCES

1. R. Kondo, private communication.
2. C. Feng *et al.*, Chinese Phys. B 25, 117106 (2016).

Current Activities of Research and Education on BL-5 (FY2023)

T. Yokoya^{a,b}, T. Wakita^a and Y. Muraoka^{a,b}

^aResearch Institute for Interdisciplinary Science, Okayama University

^bResearch Laboratory for Surface Science, Okayama University, Okayama 700-8530, Japan

Keywords: Photoemission spectroscopy, photoelectron emission microscopy

We present an overview of our recent research and educational activities on beamline 5 (BL5) in the fiscal year 2023. Our beamline has two experimental stations in a tandem way. The first station is equipped with an angle-resolved photoemission spectrometer (ARPES), a low energy electron diffraction (LEED) apparatus and an X-ray source. The hemispherical analyzer of ARPES spectrometer (HA54, VSW) has a mean radius of 50 mm and is mounted on a twin axis goniometer in ultra-high vacuum chamber. Using this goniometer, one can perform ARPES and photoelectron diffraction (PED) measurements. It is also possible to perform resonant photoemission spectroscopy (RPES) measurements by using photon energy tunability of synchrotron radiation with X-ray absorption spectroscopy (XAS) measurement. With the X-ray source (XR2E2, FISOONS), we can perform an X-ray photoelectron spectroscopy (XPS) measurement for the chemical state analysis and the PED. At the second station, we have installed a photoelectron emission microscope (PEEM, 'PEEM III', Elmitec). PEEM provides a magnified image of lateral intensity distribution of photo-emitted electrons from a sample surface. The spatial resolutions are several ten nanometers with Hg lamp and a few micrometers with synchrotron radiation. The sample is transferred between the ARPES and the PEEM chamber in-situ, and one can perform measurements at both stations for the same sample.

In the recent researches on BL-5, we have studied the electronic structure of potassium doped aromatic molecule (K_x picene) [1], iron-based superconductor ($FeSe_xTe_{1-x}$) [2], transition metal di-oxide films such as VO_2 thin films which exhibits a first-order metal-to-insulator transition at 340 K [3], CrO_2 thin films which are known as a half-metallic material [4], TaO_2 film which is stabilized with a new technique developed in our group [5], and phase-separated TiO_2 - VO_2 films on mica substrates. We have also studied the electronic structures of a high-quality boron-doped diamond film which shows a signature of the highest superconducting transition temperature of 25 K [6] and a high quality single crystal of $YbFe_2O_4$ which is one of multiferroic materials [7], by utilizing RPES at B K - and Fe $M_{2,3}$ - edges, respectively. In addition, we have studied the sp^3 content in diamond-like carbon films by using photoemission spectroscopy in order to optimize the conditions to produce Q-carbon (quenched carbon) which is a newly discovered amorphous phase of carbon with several exotic properties [8]. In the last few years, we have performed PEEM and TEY measurements at BL5 in HiSOR for (1) a B-doped carbon nano wall film on a Si substrate, (2) a micro-droplet of solidified L-boronophenylalanine (L-BPA) on a Si substrate and (3) cancer cells dosed with L-BPA in order to investigate microscopic chemical states of trace B atoms in them from fine structures in local- and wide-area-XAS spectra near B K -edge and to visualize B distributions on their surfaces. For this kind of measurements with PEEM, we have developed a new auto-measurement system where we can obtain a serial PEEM images with excitation x-ray energies for a certain energy range with a fixed energy step.

Recently, we have prepared an auto-measurement system and an X-ray focusing capillary lens for photoemission holography (PEH) measurements. PEH is a method that has been greatly developed in Japan in recent years as a measurement method for elucidating the local structure of materials with an atomic resolution [9]. In particular, various results have been reported in the study of the three-dimensional atomic configurational structure around the dopants in crystals [10]. However, the opportunity to use state-of-the-art apparatuses (for example, DA30 analyzer and RFA of BL25SU at SPring-8) are limited. Although our photoelectron energy analyzer is an old model and it is difficult to separate and observe small shifts in core levels because of the energy resolution of 1-2 eV of the system, we expect that our apparatus will be used for preliminary experiments on undoped materials prior to experiments for doped samples using state-of-

the-art systems. It can also be used for educational purposes such as experiencing photoelectron holography experiments and learning the analysis methods.

We have used the BL-5 for education activity as well, for example, practical education for undergraduate students of Okayama University. The students have an opportunity to study the synchrotron radiation mechanism and to experience XPS measurement which is very useful for the surface science research. We accepted more than 100 students from 2006 to 2012. From 2014, we have started to join the practical lecture for experiments using the beamline end stations in HiSOR for both graduate school students of Hiroshima and Okayama Universities. In 2018, we have had a new project for education under a Japan-Asia youth exchange program in science supported by Japan Science and Technology Agency (JST), “Sakura Exchange Program in Science”. We have accepted six students from Changchun University of Science and Technology in China.

REFERENCES

1. H. Okazaki *et al.*, *Phys. Rev* **82**, pp. 195114 (5 pages) (2010).
2. Y. Yoshida *et al.*, *J. Phys. Soc. Jpn* **78**, pp. 034708 (4 pages) (2009).
3. K. Saeki *et al.*, *Phys. Rev* **80**, pp. 125406 (5 pages) (2009).
4. Y. Muraoka *et al.*, *MRS Proceedings* **1406** (2012).
5. Y. Muraoka *et al.*, *Thin Solid Films* **599**, pp. 125-132 (2016).
6. H. Okazaki *et al.*, *Appl. Phys. Lett* **106**, pp. 052601 (5 pages) (2015).
7. K. Fujiwara *et al.*, *Trans. Mater. Res. Soc. Jpn.* **41**, pp. 139-142 (2016).
8. H. Yoshinaka *et al.*, *Carbon*.**167**, pp. 504-511 (2020).
9. T. Matsushita *et al.* *Europhys. Lett.* **71**, 597 (2005). *Phys. Status Solidi B* **255**, 1800091 (6 pages) (2018).
10. K. Hayashi, T. Matsushita, *SPring-8 Research Frontiers* **2020**, pp. 12 -15 (2021).

Visualization of boron distributions in cancer cells dosed with a boron delivery drug

Takanori Wakita^a, Kazuyo Igawa^b, Miyu Kaneda^c, Naoshi Ikeda^c,
Hiroaki Terato^d, Yuji Muraoka^{a,c}, Takayoshi Yokoya^{a,c}

^aResearch Institute for Interdisciplinary Science, Okayama University

^bNeutron Therapy Research Center, Okayama University

^cGraduate School of Natural Science and Technology, Okayama University

^dAdvanced Science Research Center, Okayama University

Keywords: Photoemission electron microscopy, local X-ray absorption spectroscopy, elemental distributions

Boron Neutron Capture Therapy (BNCT) has attracted attention in recent years as a cancer treatment method that aims to destroy only cancer cells without damaging normal cells. It has achieved remarkable results in the treatments of cephalon and cervix cancers. [1]. In this method, cancer cells are destroyed by an alpha-ray and a lithium ion emitted through a nuclear reaction between a boron nuclear and a thermal neutron ray. In order to increase the probability of selectively destroying only cancer cells while causing as little damage to normal cells as possible, it is essential to increase the accumulation of boron compounds on the target cancer cells, which will contribute to maximize the effect of BNCT with thermal neutrons of the lowest possible intensity. Visualization of intracellular boron distribution using microscopic techniques provides important clues for the development of boron compounds that can efficiently accumulate in cancer cells.

Electron probe micro analyzer (EPMA) has been widely used in visualization of microscopic elemental distributions on various material surfaces as one of the most popular techniques, by means of combination of a scanning electron microscope and an X-ray fluorescence analyzer [2]. X-ray fluorescence is produced via relaxation of core-holes excited, in this case, by an electron beam, which is therefore element specific in nature. For light elements such as boron (B), however, Auger transition rates are more than 99.9% in their core-hole relaxation processes, which means that detection of trace light elements by X-ray fluorescence has difficulty. In contrast, X-ray absorption spectroscopy (XAS) with total electron yield (TEY) is suitable to detect trace light elements because TEY is proportional to the amount of secondary electrons generated mainly by Auger electrons [3]. The intensity of photoemission electron microscope (PEEM) is also proportional to the TEY intensity when it is used with X-ray as a light source and without both an energy filter and an energy analyzer [4]. One can obtain a local XAS spectrum by plotting intensities in a certain area on a series of PEEM images as a function of X-ray energies. In addition, an elemental distribution image can be obtained as a difference image of two PEEM images measured at X-ray energies of (1) a pre-edge and (2) a peak position above a certain absorption edge.

In this study, we have performed PEEM and TEY measurements at BL5 in HiSOR for (1) a micro-droplet of solidified L-boronophenylalanine (L-BPA), which is used as a boron delivery drug in clinical BNCTs, on a Si substrate and (2) cancer cells dosed with L-BPA, in order to investigate microscopic chemical states of trace B atoms in them from fine structures in local- and wide-area-XAS spectra near B K-edge and to visualize B distributions on their surfaces. For this kind of measurements with PEEM, we have developed a new auto-measurement system where we can obtain a serial PEEM images with excitation x-ray energies for a certain energy range with a fixed energy step. The experimental station of BL5 is equipped with a PEEM III (Elmitec GmbH) and with a manipulator connected to a digital amperemeter for a TEY measurement. As a light source, the second-order X-rays from the monochromator were used because they have higher intensity and energy resolution around B K-edge than the first-order X-ray from the monochromator with the same entrance and exit slit widths. All the measurements were performed at room temperature.

In order to elucidate the XAS signals from L-BPA, first we have performed PEEM and TEY measurements for a micro-droplet of solidified L-BPA on a Si substrate. Figure 1 (a) shows an optical microscope image of

a micro-droplet on a Si substrate. The size of the micro-droplet is about 100 μm . Figure 1 (b) shows a PEEM image of the same micro-droplet measured with Hg lamp showing 2 dimensional local work function distribution for it. The field of view is 150 μm . The blue curve in figure 1 (c) shows plots of averaged intensities per a pixel in blue square in figure 1 (b) as a function of X-ray energy around B K-edge, showing a local XAS spectrum which has a sharp peak structure at 193.6 eV and a small bump at 191.6 eV. These clear structures are not observed in an XAS spectrum measured by TEY (black curve in figure 1 (c)) which provides an averaged information of the sample surface from a wide area illuminated by X-ray (the size of X-ray is about 1 x 5 mm^2 on the sample surface). These results demonstrate the effectiveness of PEEM measurements for detecting signals from small amounts of substances on a sample surface.

Figure 2 (a) shows an optical microscope image of a colony of cancer cells dosed with L-BPA on a silicon substrate. Figure 2 (b) shows a PEEM image of the same colony measured with X-ray of 195 eV. The field of view is 150 μm . The red curve in figure 2 (c) shows plots of averaged intensities per a pixel in red square in figure 2 (b) as a function of X-ray energy around B K-edge. For the blue curve in figure 2 (c), 30 PEEM images are summed for each X-ray energy, providing better S/N ratio of the blue curve than the one of the red curve. The small structures in this local-XAS spectrum for the cancer cell does not resemble the ones in figure 1 (c) for micro-droplet of L-BPA. This suggests that the L-BPA may be decomposed in the cancer cell. Further measurements to obtain more better S/N ratio in a local-XAS spectrum for the cancer cells are in progress.

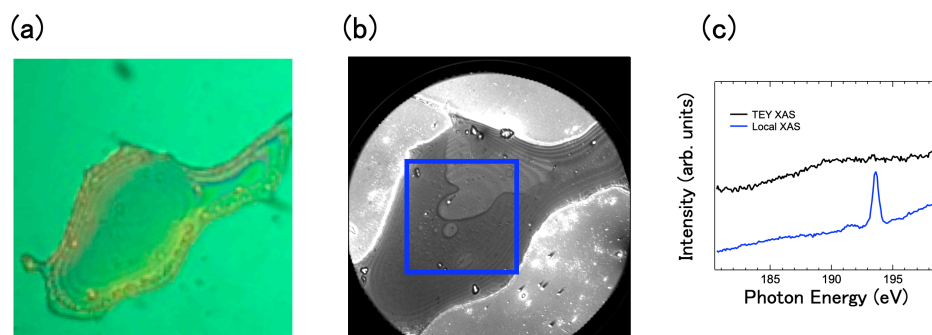


FIGURE 1. (a) An optical microscope image of a micro-droplet on a Si substrate. The size of the micro-droplet is about 100 μm . (b) A PEEM image of the same micro-droplet measured with Hg lamp. The field of view is 150 μm . The blue curve in (c) shows plots of averaged intensities per a pixel in blue square in figure 1 (b) as a function of X-ray energy around B K-edge. The black curve shows an XAS spectrum measured by TEY.

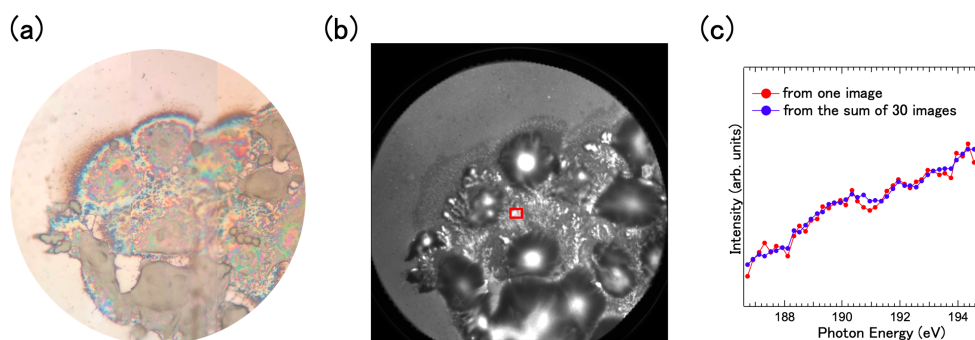


FIGURE 2. (a) An optical microscope image of a colony of cancer cells dosed with L-BPA on a silicon substrate. (b) A PEEM image of the same colony measured with X-ray of 195 eV. The field of view is 150 μm . The red curve in (c) shows plots of averaged intensities per a pixel in red square in figure 2 (b) as a function of X-ray energy around B K-edge. For the blue curve in figure 2 (c), 30 PEEM images are summed for each X-ray energy.

REFERENCES

1. H. Nakashima, YAKUGAKU ZASSHI 142, 155-164 (2022).
2. J. I. Goldstein *et al.*, *Scanning electron microscopy and X-ray microanalysis 4th ed.*, Springer (2017).
3. A. Erbil *et al.*, Phys. Rev. B **37**, 2450 (1988).
4. A. Locatelli and E. Bauer, J. Phys.: Condes. Matter **20**, 093002 (2008).

HiSOR, BL-1, BL-9A / SPring-8, BL-25SU

Fermi surface of chiral magnet $\text{Yb}(\text{Ni}_{1-x}\text{Cu}_x)_3\text{Al}_9$ observed by ARPES

Y. Tanimoto^a, M. Sugimoto^a, R. Kamimori^a, Y. Nakashima^b, H. Sato^c,
K. Yamagami^d, M. Arita^c, S. Kumar^c, K. Shimada^c, S. Nakamura^e, S. Ohara^e

^aGraduate School of Advanced Science and Engineering, Hiroshima University,
Higashi-Hiroshima 739-8526, Japan

^bFaculty of Science, Hiroshima University, Higashi-Hiroshima 739-8526, Japan

^cHiroshima Synchrotron Radiation Center, Hiroshima University, Higashi-Hiroshima 739-0046, Japan

^dJapan Synchrotron Radiation Research Institute, Sayo 679-5148, Japan

^eGraduate School of Engineering, Nagoya Institute of Technology, Nagoya 466-8555, Japan

Keywords: chiral magnetic crystal, helical magnetism, angle resolved photoemission spectroscopy

Trigonal YbNi_3Al_9 has a chiral crystal structure belonging to space group of $R32$ (No. 155) and is of interest as the first chiral magnetic alloy discovered in $4f$ electron compounds [1]. The localized Yb $4f$ spins are magnetically ordered below $T=3.4$ K, ferromagnetic in the c -plane, and exhibit left-handed or right-handed helimagnetism with propagation vector $\mathbf{q}=(0, 0, 0.8)$ [2]. Substitution of Ni with Cu significantly alters the magnetic interaction and shortens the helical propagation vector to $\mathbf{q}=(0, 0, 0.4)$ for $\text{Yb}(\text{Ni}_{0.94}\text{Cu}_{0.06})_3\text{Al}_9$. Spin-polarized conduction electrons are thought to be responsible for this phenomenon. In this study, we have performed vacuum ultraviolet and soft x-ray angle-resolved photoemission spectroscopy (VUV-ARPES and SX-ARPES) on YbNi_3Al_9 and $\text{Yb}(\text{Ni}_{0.94}\text{Cu}_{0.06})_3\text{Al}_9$ to observe the Fermi surface. The experiments were carried out at BL-1 and BL-9A of Hiroshima Synchrotron Radiation Center (HSRC), Hiroshima University for VUV-ARPES and at BL-25SU of SPring-8 for SX-ARPES. Single crystals used for the SX-ARPES measurements were synthesized by the flux-method [3].

VUV-ARPES revealed five hole-like Fermi surfaces around the $\bar{\Gamma}$ points and an electronic Fermi surface around the \bar{K} point for YbNi_3Al_9 and $\text{Yb}(\text{Ni}_{0.94}\text{Cu}_{0.06})_3\text{Al}_9$. The Fermi surface of $\text{Yb}(\text{Ni}_{0.94}\text{Cu}_{0.06})_3\text{Al}_9$ is shrink compared to that of YbNi_3Al_9 , although the feature is almost unchanged with the Cu substitution.

Figure 1(a) shows the SX-ARPES intensity plots of YbNi_3Al_9 along the $\bar{\Gamma}$ - \bar{M} directions of the surface Brillouin zone measured at $h\nu=548$ eV with circular-polarized light. Figure 1(b) shows the angle integrated spectrum. Two flat bands derived from the localized $\text{Yb}^{2+} 4f_{7/2}$ states below the Fermi level (E_F) and $\text{Yb}^{2+} 4f_{5/2}$ states at $E_B=1.4$ eV are observed. Two hole-like bands around the $\bar{\Gamma}$ point cross E_F at $k_x=0.31$ and 0.45 \AA^{-1} . These two hole-like bands are clearly observed in the VUV-ARPES spectra measured at $h\nu=24$ eV with s -polarized geometry.

Figure 2 represents the Fermi surface of YbNi_3Al_9 measured at $h\nu=450\sim 652$ eV with circular-polarized geometries. The horizontal and vertical axes are the wavenumbers k_x along $\bar{\Gamma}$ - \bar{M} direction of the surface Brillouin zone and k_z along the Γ - Z direction of the bulk Brillouin zone, respectively. A barrel-shaped Fermi surface with the minimum k_x at the Γ point and the maximum k_x at the Z point is observed, as indicated by a black line. Inside it, in addition, we find another barrel-shaped Fermi surface. On the other hand, the Fermi surface observed around $k_x=0.15$ \AA^{-1} (white line) appears to be a drum-shaped Fermi surface with the minimum k_x at the Z point and is closed between the Γ and Z points as indicated by the arrows. These Fermi surfaces are quantitatively consistent with the Fermi surfaces inferred from de Haas-van Alphen effect [4].

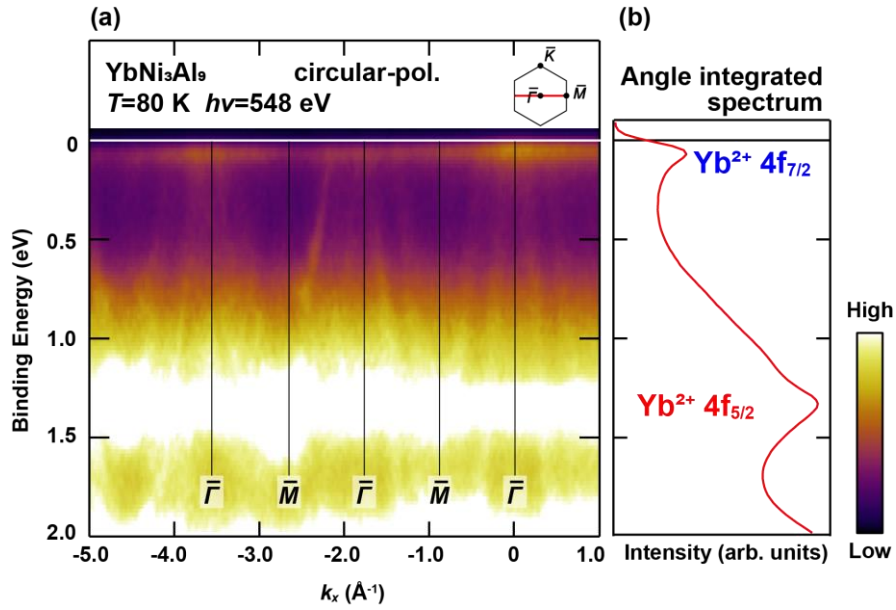


Fig. 1 (a) SX-ARPES intensity plots of YbNi_3Al_9 measured along the $\bar{\Gamma}$ - \bar{M} direction measured at $h\nu=548$ eV with circular-polarized light. (b) Angle integrated spectrum of (a).

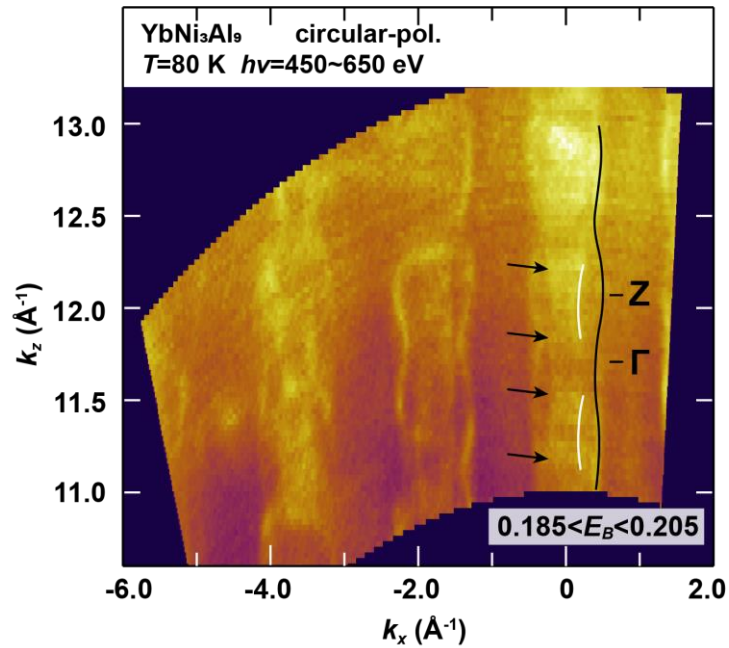


Fig. 2 Fermi surfaces of YbNi_3Al_9 obtained from SX-ARPES spectra measured at $h\nu=450\sim 652$ eV with circular-polarized light.

REFERENCES

1. S. Ohara, S. Fukuta, K. Ohta, H. Kono, T. Yamashita, Y. Matsumoto and J. Yamaura, JPS Conf. Proc. **3**, 017016 (2014).
2. T. Matsumura, Y. Kita, K. Kubo, Y. Yoshikawa, S. Michimura, T. Inami, Y. Kousaka, K. Inoue and S. Ohara, J. Phys. Soc. Jpn. **86**, 124702 (2017).
3. T. Yamashita, R. Miyazaki, Y. Aoki and S. Ohara, J. Phys. Soc. Jpn. **81**, 034705 (2012).
4. S. Ohara, private communication.

ARPES study of TiFe_xS_2 ($x = 0, 0.33$)

Y. Nakashima^a, Y. Tanimoto^b, M. Sugimoto^b, H. Sato^c, Y. Miyai^b, S. Ideta^c,
K. Shimada^c, M. Miyata^d, M. Koyano^d

^aFaculty of Science, Hiroshima University, Higashi-Hiroshima 739-8526, Japan

^bGraduate School of Advanced Science and Engineering, Hiroshima University,
Higashi-Hiroshima 739-8526, Japan

^cHiroshima Synchrotron Radiation Center, Hiroshima University, Higashi-Hiroshima 739-0046, Japan

^dSchool of Materials Science, Japan Advanced Institute of Science and Technology, Nomi 923-1292, Japan

Keywords: intercalation, superlattice, angle resolved photoemission spectroscopy

$1T\text{-TiS}_2$ is non-magnetic layered material with $1T\text{-CdI}_2$ -type crystal structure. The hexagonal layer of Ti ions is sandwiched between the two hexagonal layers of S ions and the Ti ion is octahedrally coordinated with six S ions. The S-Ti-S triple layers are covalently bonded and these TiS_2 triple layers are weakly coupled with van der Waals (vdW) force. In the vdW gap located between the TiS_2 layers, the other $3d$ transition-metal M can be intercalated as $M_x\text{TiS}_2$. Among them, Fe_xTiS_2 exhibits a wide variety of magnetic properties [1]. With increasing the Fe concentration from $x = 0$, the cluster spin glass (CG) state with the Ising spins is found for $x < 0.20$. After exhibiting the antiferromagnetic (AFM) state up from $x = 0.20$ to 0.28 , the CG state is again realized for $0.28 < x < 0.38$ and the AFM state for $0.38 < x < 0.50$. Above $x = 0.50$, the ferrimagnetic behavior is observed. On the other hand, the Fe ion intercalated in the vdW gap between the TiS_2 layers occupy the octahedral site surrounded by six S ions. X-ray studies reveal the Fe random distribution for $x < 0.20$, while the formation of $2\sqrt{3}a \times 2a \times 2c$ or $2a \times 2a \times 2c$ superlattices due to the Fe ordering for $x = 0.25$ and $\sqrt{3}a \times \sqrt{3}a \times 2c$ superlattice for $x = 0.33$. The rich magnetic states of Fe_xTiS_2 are expected to link to the change in electronic band structure due to the Fe intercalation. In this study, we carried out angle-resolved photoemission spectroscopy (ARPES) to reveal the electronic band structure of Fe_xTiS_2 ($x = 0, 0.33$) at beamlines BL-1 and BL-7 of Hiroshima Synchrotron Radiation Center (HSRC).

Figure 1(a) shows the ARPES intensity plots of TiS_2 measured at $h\nu=66$ eV along the $\bar{\Gamma}\text{-}\bar{M}$ directions of the surface Brillouin zone, roughly corresponding to $\Gamma\text{-}M$ direction of the bulk Brillouin zone, estimated from the $h\nu$ -dependent measurements. We find an electron pocket derived from the Ti $3d$ states around the M point. Almost non-dispersive band is observed at binding energy of $E_B = 0.3$ eV, which is assigned to the $3d$ states of the Ti ions self-intercalated in the vdW gap between TiS_2 layers. The parabolic band around the Γ point is due to the S $3p$ states.

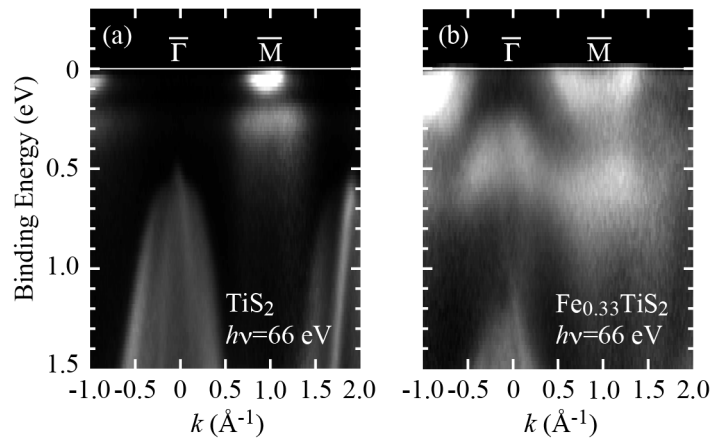


FIGURE 1. ARPES intensity plots of (a) TiS_2 and (b) $\text{Fe}_{0.33}\text{TiS}_2$ measured at $h\nu = 66$ eV along $\bar{\Gamma}\text{-}\bar{M}$ direction.

Figure 1(b) shows the ARPES intensity plots of $\text{Fe}_{0.33}\text{TiS}_2$. The electron pocket around the M point is shifted to higher binding energy. In addition, the parabolic S $3p$ band is also shifted. These results indicate that electrons are transferred from the intercalated Fe ions to host TiS_2 layers. The dispersive Fe $3d$ -derived band is observed around $E_B = 0.3 - 0.7$ eV, reflecting the Fe ions align periodically in the vdW gap parallel to the TiS_2 layers (in plane). The Fe $3d$ band seems to be bent upward before the M point, probably due to the $\sqrt{3}a \times \sqrt{3}a$ periodicity in plane for $x = 0.33$. We measured the ARPES spectra along the Γ -A direction with changing $h\nu$ from 30 to 124 eV. We find that the Fe $3d$ band exhibits the dispersion along the direction normal to the TiS_2 layers and has half period of the S $3p$ band, reflecting the $2c$ periodicity due to the formation of $\sqrt{3}a \times \sqrt{3}a \times 2c$ superlattice.

REFERENCES

1. N. V. Selezneva, E. M. Sherokalova, A. Podlesnyak, M. Frontzek and N. V. Baranov, Phys. Rev. Mater. **7**, 014401 (2023).

Preparation of Pt Thin Film on MgO (001) and Observation of Its Electronic Structure

T. Asano^a, K. Sumida^b, K. Kunitomo^a, T. Okuda^b, and K. Miyamoto^b

^aGraduate School of Advanced Science and Engineering, Hiroshima University, 1-3-1 Kagamiyama,
Higashi-Hiroshima 739-8526, Japan

^bHiroshima Synchrotron radiation Center (HSRC), Hiroshima University 2-313 Kagamiyama,
Higashi-Hiroshima 739-0046, Japan

Keywords: Pt thin film, Spin Hall effect, Photoemission spectroscopy

Spin Hall effect is an important physical phenomenon that generates spin-polarized currents and is essential for the development of spintronics devices. The spin Hall effect in metals has attracted attention because conductance mismatches are markedly suppressed at an interface with ferromagnet compared to the semiconductors and allows the use of spin-polarized current supplied by the ferromagnetic metal [1]. Among many metals, elemental Pt is extensively investigated both experimentally and theoretically [2,3]. Kimura *et al.* reported that the Pt wire exhibits largest spin Hall conductivity as large as 2.4×10^4 S/m at room temperature, which is 4 orders of magnitude larger than that of typical semiconductors, such as GaAs [2]. In order to inject spin-polarized current into ferromagnets more efficiently, the orientation of spin current must be precisely controlled, i.e., it is necessary to observe its spin orientation. In previous studies, the rough spin orientation of spin currents induced by spin Hall effects has been obtained by using the magneto-optical Kerr effect [4]. However, the experimental method to precisely detect the spin orientation induced by the spin Hall effect has not been established yet. One solution is *operando* spin-resolved photoemission spectroscopy (PES) measurements under an external electric field.

In this work, as a first step towards the development of the experimental method, we fabricated Pt thin films and investigated the electronic structure by PES measurements. The Pt thin films were prepared by using electron beam evaporation source with a carbon crucible on a MgO(001) substrate at room temperature. The MgO substrate was annealed in oxygen atmosphere ($\sim 10^{-1}$ Pa) at $\sim 200^\circ\text{C}$ for 60 min., and then, annealed at 600°C for 240 min. in vacuum prior to the Pt deposition.

To observe the electronic structure of the fabricated Pt/MgO film, we performed the PES measurements at BL-7 of Hiroshima Synchrotron Radiation Center utilizing various incident photon energies from 30 to 160 eV. Figure 1 shows Pt 4*f* core level spectrum taken at $h\nu = 155$ eV. Two peaks derived from the spin-orbit split Pt 4*f*_{5/2} and 4*f*_{7/2} are clearly seen at binding energy (E_B) of 74.4 and 71.1 eV. To obtain more detailed information, the experimental result was fitted by Doniac-Šunjić function with Shirley background function [see blue curve in Fig. 1]. From this fitting result, asymmetric parameters were determined to be 0.018 for 4*f*_{5/2} and 0.043 for 4*f*_{7/2}. These values are very small as a metal, suggesting that the density of states (DOS) near the Fermi level (E_F) is small.

The red curve in Fig. 2 shows the experimentally observed valence band PES spectrum taken at $h\nu = 70$ eV. We can see broad peak structures around $E_B = 1.6$ and 4.5 eV. Moreover, a dip structure is recognized at $E_B = 3.2$ eV. To compare the valence band spectrum, we carried out the first-principles calculation for the face-centered-cubic Pt using WIEN2k program including the spin-orbit coupling. Based on the calculation, it was found that the *d* orbital component is dominant in the valence band rather than the *s* and *p* orbitals. Moreover, photo-ionization cross-section of *d* orbital is dominated in the vacuum ultraviolet region. Therefore, in Fig. 2, we compare the PES spectrum with the Pt *d* partial DOS. Here, the calculated Pt *d* partial DOS was multiplied by the Fermi-Dirac distribution function at 300 K and convoluted by a Gaussian function (experimental resolution). Comparing the experimental and theoretical results, we notice that the locations of the peak and dip structures and the band width are qualitatively reproduced. However, a very

sharp peak predicted by the calculation in the vicinity of E_F was not observed in the experiment. This suggests that the interface and/or surface structure of the fabricated Pt film on MgO substrate makes the electronic structure differ from the electronic structure in the bulk Pt.

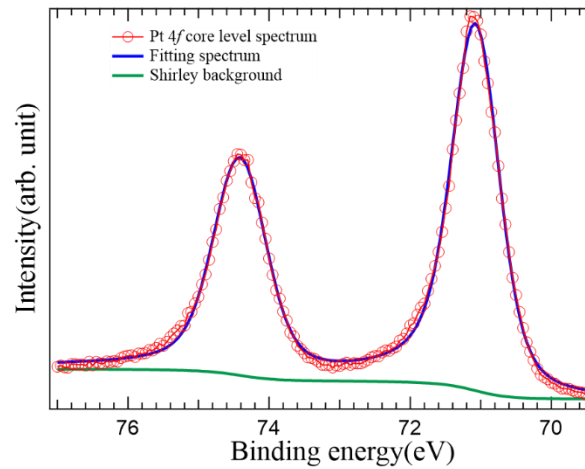


FIGURE 1. Pt 4f core level spectrum (red circles) taken at $h\nu = 155$ eV. The blue curve represents the fitting result using the Doniach-Šunjić function and active Shirley background (green curve).

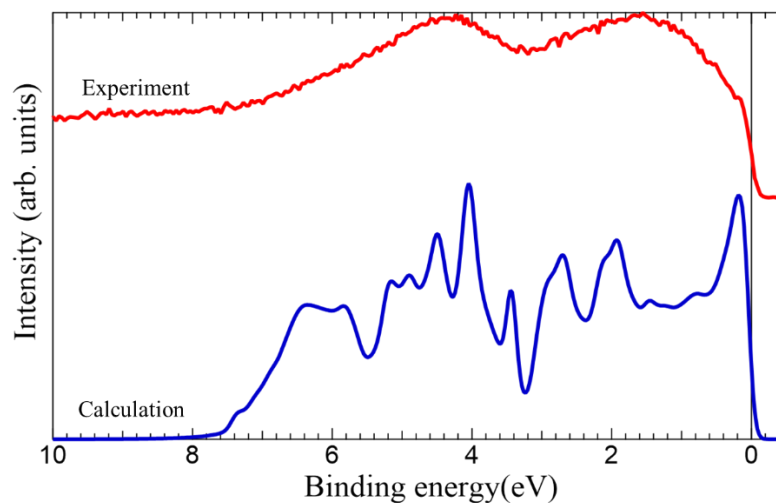


FIGURE 2. Observed photoemission spectrum taken at $h\nu = 70$ eV (red) and the calculated Pt d partial DOS (blue). The calculated DOS is multiplied by the Fermi-Dirac distribution function and convoluted by a Gaussian function.

In conclusion, we are successful to prepare Pt thin film on MgO(001) using electron beam evaporate source with a carbon crucible. Around E_F , the observed electronic structure on Pt thin film is different from calculated spectrum based on the bulk Pt. In general, the performance of the spin Hall effect is closely related to the electronic structure, so this finding of discrepancy may be important information for improving the performance of the spin Hall effect for Pt thin film on MgO(001).

REFERENCES

1. G. Schmidt, *et al.*, Phys. Rev. B **62**, R4790(R) (2000).
2. T. Kimura *et al.*, Phys. Rev. Lett. **98**, 156601 (2007).
3. G. Y. Guo, *et al.*, Phys. Rev. Lett **100**, 096401(2008).
4. Y. K. Kato, *et al.*, Science **306**, 5703 (2004).

Attempt to Control the Anisotropy of Topological Surface States

R. Yamamoto^a, K. Sumida^b, K. Miyamoto^b, and T. Okuda^b.

^a*Graduate School of Advanced Science and Engineering Hiroshima University, 1-3-1 Kagamiyama Higashi-Hiroshima 739-8526, Japan*

^b*Hiroshima Synchrotron Radiation Center (HSRC), Hiroshima University 2-313 Kagamiyama, Higashi-Hiroshima 739-0046, Japan*

Keywords: Topological Surface States, Silicon Vicinal Surface, Anisotropy of Band Structure, Bi₂Te₃ film

Topological insulators have spin-polarized conduction states on their surfaces (= topological surface states), where the spin direction of electrons is locked by their momentum resulting the helical spin-texture. The unique helical spin-texture is considered to prohibit complete backscattering by non-magnetic impurities. Thus, the surface of topological insulators is expected to be promising platform for spintronics devices. However, other backscattering passes except for the complete backscattering are not prohibited [Fig.1(a)]. One solution to suppress the backscattering is forming an anisotropic Fermi surface, ideally a one-dimensional Fermi surface[Figs. 1(b) and 1(c)].

In previous research, it has been reported that Ag films on Si(111)-(4×1)-In, which has an array of In chains, exhibit a quasi-one-dimensional band structure [1]. This result is attributed to the confinement of electrons in the quasi-one-dimensional Ag films caused by the step and terrace structure, and a similar effect can be expected even on vicinal surface. The vicinal silicon surface has atomically regular step arrays and electron motion in the film grown on the surface might be restricted only one direction parallel to the step. From this analogy, we considered that it might be possible to obtain the anisotropic spin-polarized band structure by growing Bi₂Te₃ films on silicon vicinal surface. However, there is no report of the fabrication of Bi₂Te₃ film on silicon vicinal surface so far. Therefore, the purposes of this research are to fabricate Bi₂Te₃ film on silicon vicinal surface, measure the band structure, and evaluate the band anisotropy.

In our study, we grew Bi₂Te₃ ultrathin films on Si(111) and Si(557) by molecular beam epitaxy, which were used as flat and vicinal surface substrate, respectively. Si(557) is a surface tilted by 9.5° from Si(111), and its terraces have the same plane as Si(111). We checked the quality of surface structure by low energy electron diffraction (LEED) and auger electron spectroscopy (AES). Figure 2 shows LEED patterns and the spectra of AES of Bi₂Te₃ film on each substrate. As in Fig. 2, we can see clear spots in LEED and peak of Bi and Te in AES indicating that we could succeed to grow Bi₂Te₃ film on vicinal silicon surface.

To observe the band structure of the fabricated films, angle-resolved photoemission spectroscopy (ARPES) measurements were done at BL-7 in HiSOR. Figure 3(a) shows the wide energy range ARPES images on Si(111) (top) and Si(557) (bottom). Clear bulk bands are observed on Si(111). On Si(557) substrate faint but similar bands that are shifted by 9.5° from the results of Si(111) are observed. Figure 3(b) shows the magnified band structure near the Fermi energy of each sample. A clear V-shaped topological surface state is visualized on Si(111). The observed feature is very similar to the previously reported band structure of Bi₂Te₃/Si(111) films with one quintuple layer (QL) thickness [2]. Thus, the thickness of our film is estimated to be ~1 QL. On Si(557) substrate, similar V-shaped surface state crossing the Fermi energy can be seen, but it was hard to estimate the Fermi momenta (k_F) of surface bands due to the weak intensity. Although we attempted to evaluate the anisotropy of the surface bands by Fermi surface in Fig. 3(c), unfortunately, it was also difficult.

In conclusion, we succeeded to grow Bi₂Te₃ film on silicon vicinal surface and to measure the band structure. However it was difficult to evaluate the band isotropy because of the poor intensity of topological surface states on Bi₂Te₃/Si(557). Further experiment with the better sample quality is expected in the future.

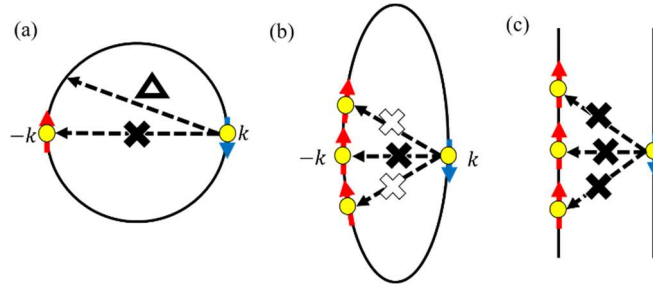


FIGURE 1. Schematic illustrations of isotropic (a), anisotropic (b), and ideally anisotropic (one-dimensional) Fermi surfaces (c) of topological insulator.

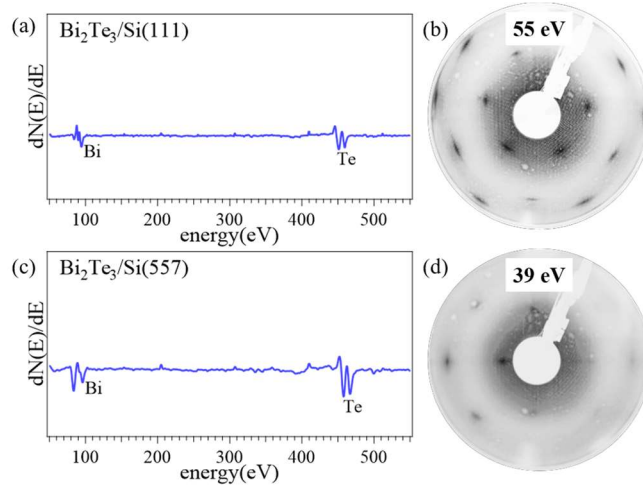


FIGURE 2. (a) AES spectrum of $\text{Bi}_2\text{Te}_3/\text{Si}(111)$ (b) LEED pattern of $\text{Bi}_2\text{Te}_3/\text{Si}(111)$ taken at 55 eV. (c) AES spectrum of $\text{Bi}_2\text{Te}_3/\text{Si}(557)$ (d) LEED pattern of $\text{Bi}_2\text{Te}_3/\text{Si}(557)$ taken at 39 eV.

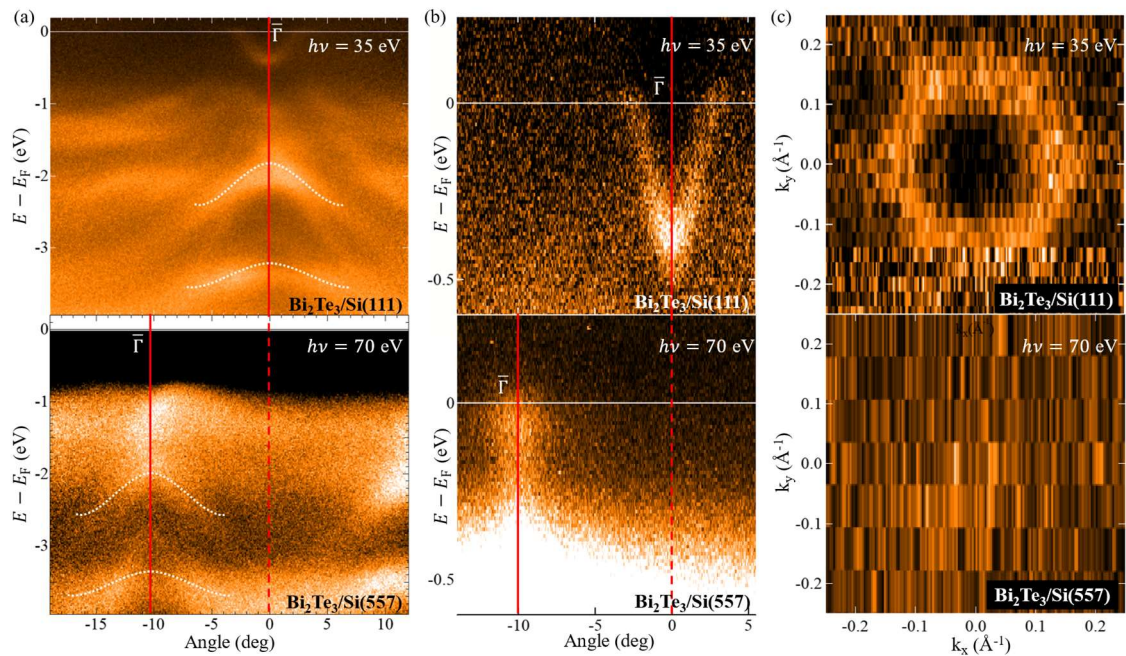


FIGURE 3. (a) Wide range ARPES images of $\text{Bi}_2\text{Te}_3/\text{Si}(111)$ and $\text{Bi}_2\text{Te}_3/\text{Si}(557)$ acquired at $h\nu = 35$ and 70 eV. (b) Magnified ARPES images around the Fermi energy of (a). (c) Fermi surface of $\text{Bi}_2\text{Te}_3/\text{Si}(111)$ and $\text{Bi}_2\text{Te}_3/\text{Si}(557)$

REFERENCES

1. N.Nagamura *et al.*, Phys. Rev. Lett. **96**, 256801 (2006).
2. S. Hatta *et al.*, Sci. Rep. **11**, 5742 (2021).

Spin-polarized electronic states of FeCo thin film on Rh(001) substrate

K. Kunitomo^a, K. Sumida^b, K. Miyamoto^b, C. Zhang^a,
Y. Sakuraba^c, and T. Okuda^b

^aGraduate School of Advanced Science and Engineering Hiroshima University, 1-3-1 Kagamiyama, Higashi-Hiroshima 739-8526, Japan

^bHiroshima Synchrotron Radiation Center (HSRC), Hiroshima University 2-313 Kagamiyama, Higashi-Hiroshima 739-0046, Japan

^cNational Institute for Materials Science (NIMS), 1-2-1 Sengen, Tsukuba, Ibaraki 305-0047, Japan

Keywords: FeCo alloys, spin polarization, perpendicular magnetic anisotropy (PMA)

The emergence of perpendicular magnetic anisotropy (PMA) in magnetic thin films is essential from the viewpoint of practical applications, *e.g.*, increasing the recording density of storage devices. Many magnetic thin films exhibiting PMA, such as Co/Pt, Co/Pd, FePt, TbFeCo, and GdFeCo, have been extensively investigated. Among them, “rare-earth and noble-metal elements free” FeCo alloy films are considered promising candidates exhibiting strong PMA. Burkert *et al.* predicted that a magnetic anisotropy energy may increase in FeCo alloys when the tetragonal distortion is applied [1]. Remarkably, around a c/a ratio of 1.20-1.25, the magnetic anisotropy energy exceeds 700-800 $\mu\text{eV}/\text{atom}$, which is one or two orders of magnitude larger than that of pure Fe or Co. The emergence of strong PMA was experimentally confirmed in the tetragonally distorted FeCo ultra-thin-films grown on Rh(001) ($c/a = 1.24$) with a thickness of 13-17 monolayers (ML) [2].

Generally, it is known that the band structure near the Fermi energy (E_F) plays a very important role in achieving PMA [3,4]. The theoretical calculations suggest that the microscopic origin of PMA in the tetragonally distorted FeCo alloy is attributed to the minority-spin states composed of d_{xy} and $d_{x^2-y^2}$ orbitals near E_F , hybridized by spin-orbit interactions [1]. However, the spin- and orbital-dependent electronic states of the tetragonally distorted FeCo alloy films are poorly investigated experimentally.

In this study, we have fabricated FeCo thin films on Rh(001) substrate by molecular beam epitaxy and investigated the spin-polarized electronic states by *in-situ* spin- and angle-resolved photoemission spectroscopy (spin-ARPES) at BL-9B of Hiroshima Synchrotron Radiation Center [5]. The quality of the sample surface was checked by low energy electron diffraction and Auger electron spectroscopy. The thickness of the film was 13.6 ML. We also carried out the first-principles calculations for the tetragonally distorted FeCo alloy ($c/a = 1.24$) with/without considering the spin-orbit coupling using WIEN2k program [6]. The exchange-correlation was treated using the generalized gradient approximation.

To determine the high symmetry points along k_z direction [Fig. 1(a)], we first performed the photon-energy-dependent measurement. Figure 1(b) shows the ARPES image acquired at various incident photon energies from 45 to 70 eV with *s*-polarization. We can recognize the mostly non-dispersive bands around $E_B = 1$ eV with $k_z = 3.7 \text{ \AA}^{-1}$ and just below E_F with $k_z = 4.4 \text{ \AA}^{-1}$. The observed features are reproduced by the calculations (not shown here), and we determined that $k_z = 3.6 \text{ \AA}^{-1}$ ($h\nu = 45$ eV) corresponds to the Γ point. Figure 1(c) shows the ARPES image along the Γ -X line recorded at 45 eV with *p*-polarization. A very steep band crossing E_F around the X point is recognized. In addition, weakly dispersive bands are found in between E_F to 1.0 eV around the Γ point.

To experimentally verify the spin-polarization, we next performed the spin-resolved measurements. The sample was magnetized along (001) direction at room temperature prior to the measurements. Figures 2(a) and 2(b) display the out-of-plane spin-resolved energy distribution curves (EDCs) and spin-polarization recorded at the Γ and X points, respectively. Here, red and blue represent the majority- and minority-spin components. For both momenta, we can clearly see the out-of-plane spin-polarization. At the Γ point, we have observed a double peak structure in the minority-spin channel around $E_B = 0.2$ and 0.6 eV, although the

broad feature can be seen in the wide energy range in the majority-spin channel [Fig. 2(a)]. On the other hand, at the X point, a prominent majority-spin peak exists at E_F [Fig. 2(b)]. These findings tell us that the weakly dispersive bands around the Γ point and the steep band around the X point mainly comprise the majority-spin and majority-spin characters, respectively. Based on the theoretical investigations [2], the majority-spin states composed of d_{xy} and $d_{x^2-y^2}$ orbitals play an important role in the emergence of the PMA of the tetragonally distorted FeCo films. We finally compare the spin-ARPES results with the first-principles calculations to scrutinize the orbital characters. Figure 2(c) shows the calculated band dispersion along the Γ -X line in the minority-spin channel. The radii of the orange (black) circles are proportional to the net contribution of d_{xy} ($d_{x^2-y^2}$) orbital. By a comparison of Figs. 2(a), 2(b) and 2(c), it signifies that the observed minority-spin peak located just below E_F at the Γ point (black arrow) and at 1.1 eV at the X point (orange arrow) are mainly attributed to the $d_{x^2-y^2}$ and d_{xy} orbitals, respectively.

In summary, we have investigated the spin-polarized electronic states of the FeCo/Rh(001) films by *in-situ* spin-ARPES and first-principles calculations. The out-of-plane spin-polarization indicating the emergence of PMA was clearly observed at room temperature with zero-field. We conclude that the minority-spin states near E_F are mainly composed of $d_{x^2-y^2}$ and d_{xy} orbitals. Our findings provide the fundamental properties of the FeCo thin films and pave the way for the PMA-based applications, such as the photoelectron spin polarimeter, enabling the detection of the out-of-plane spin components.

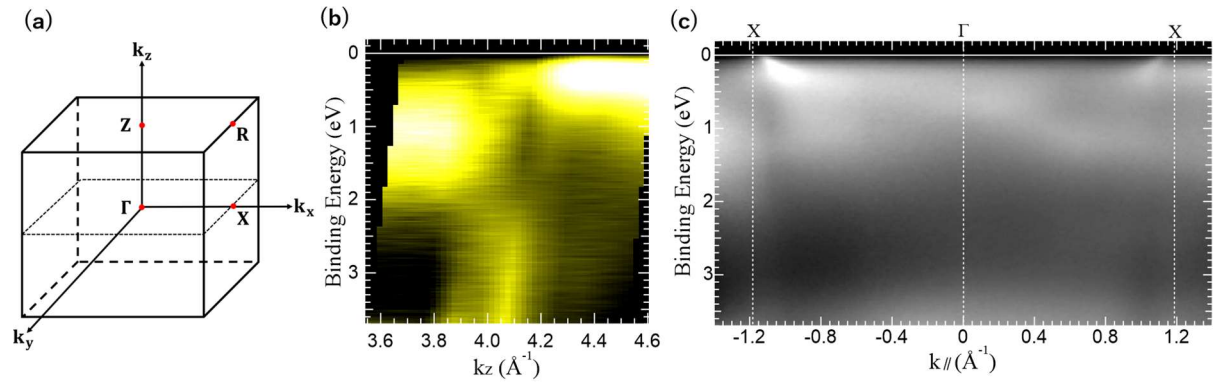


FIGURE1 (a) Brillouin Zone of bct FeCo. (b) ARPES image of FeCo/Rh(001) film acquired from 45 to 75 eV with *p*-polarized light. (c) ARPES image along the Γ -X line acquired at 45 eV with *p*-polarized light.

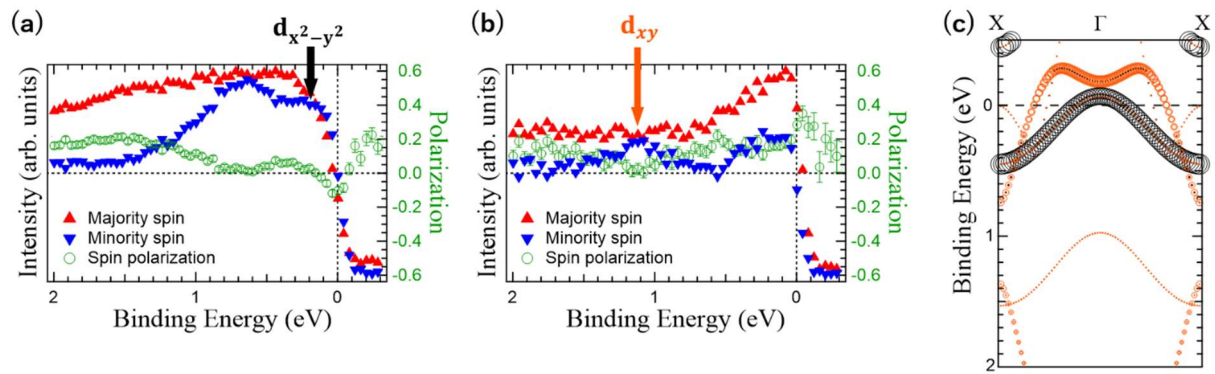


FIGURE2 (a) Out-of-plane spin-EDCs and spin-polarization at the Γ point. (b) Same as (a) but at the X point. (c) Calculated band dispersion along the Γ -X line in the minority-spin channel. Black and orange represent the $d_{x^2-y^2}$ and d_{xy} orbitals, respectively.

REFERENCES

1. T. Burkert *et al.*, Phys. Rev. Lett. **93**, 027203 (2004).
2. F. Yildiz *et al.*, Phys. Rev. B **80**, 064415 (2009).
3. P. Bruno, Phys. Rev. B **39**, 865 (1989).
4. Y. Kota and A. Sakuma, J. Magn. Soc. Jpn. **37**, 17 (2013).
5. T. Okuda *et al.*, Rev. Sci. Instrum. **82**, 103302 (2011).
6. P. Blaha *et al.*, J. Chem. Phys. **152**, 074101 (2020).

Ultrafast Spin-Dependent Dynamics in a Carrier-Tuned Topological Insulator

K. Sumida^a, K. Kunitomo^b, M. Kakoki^b, K. A. Kokh^c, O. E. Tereshchenko^c,
J. Reimann^d, J. Gdde^d, U. Hfer^d, K. Miyamoto^a, T. Okuda^{a,e}, and A. Kimura^{b,e}

^a*Hiroshima Synchrotron Radiation Center, Hiroshima University, 2-313 Kagamiyama,
Higashi-Hiroshima 739-0046, Japan*

^b*Graduate School of Advanced Science and Engineering, Hiroshima University, 1-3-1 Kagamiyama,
Higashi-Hiroshima 739-8526, Japan*

^c*Physics Department, Novosibirsk State University, ul. Pirogova 2, 630090 Novosibirsk, Russia*

^d*Department of Physics and Materials Sciences Center, Philipps-University, D-35032 Marburg, Germany*

^e*International Institute for Sustainability with Knotted Chiral Meta Matter (SKCM²), 1-3-1 Kagamiyama,
Higashi-Hiroshima 739-8526, Japan*

Keywords: Topological insulator, Time-resolved ARPES, Spin-resolved ARPES, Ultrafast carrier dynamics, Spin texture.

Topological insulators (TIs) characterized by spin-polarized Dirac-cone-like band structures on their surfaces have been extensively investigated over the last decade. As a hallmark of TIs caused by strong spin-orbit coupling, the spin-momentum-locked topological surface state (TSS) offers a pure spin current on their surfaces. The spin-polarized surface electrons of TIs are robust against nonmagnetic impurities and defects. So far, many TIs, such as Bi₂Se₃, Bi₂Te₃, and Sb₂Te₃, have been theoretically predicted and experimentally verified by angle-resolved photoemission spectroscopy (ARPES) with spin-resolution.

Recently, the ultrafast optical response of TSS has attracted much attention. Time-resolved ARPES utilizing femtosecond-laser reveals several characteristics and functionalities, *e.g.*, the emergence of Floquet state [1], population inversion [2], and the surface photovoltage effect [3]. However, the ultrafast carrier dynamics derived from the unique spin texture of TSS have hardly been investigated.

In this work, we investigated the spin-dependent ultrafast surface carrier dynamics of a ternary topological insulator (Sb,Bi)₂Te₃, where the Dirac point is adjusted to the Fermi energy (E_F), by a combination of laser-based time-resolved ARPES and synchrotron-based spin-resolved ARPES techniques. The pump-probe time-resolved ARPES measurements were performed at Philipps University of Marburg. We used two different pump energies: mid-infrared (MIR) at 0.30 eV and visible (VIS) at 2.58 eV [Figs. 1(a) and 1(d)]. We used an ultraviolet (UV) at 5.16 eV light as the probe. The spin-resolved ARPES measurements, utilizing very low energy electron diffraction type spin-polarimeters, were performed at ESPRESSO end-station (BL-9B) of Hiroshima Synchrotron Radiation Center [4].

Figure 1(b) shows the ARPES image recorded at temporal overlap ($t = 0$ ps) with the MIR-pump. We can recognize the Dirac-cone-like TSS and bulk conduction band above E_F . We also notice that the photoemission intensities

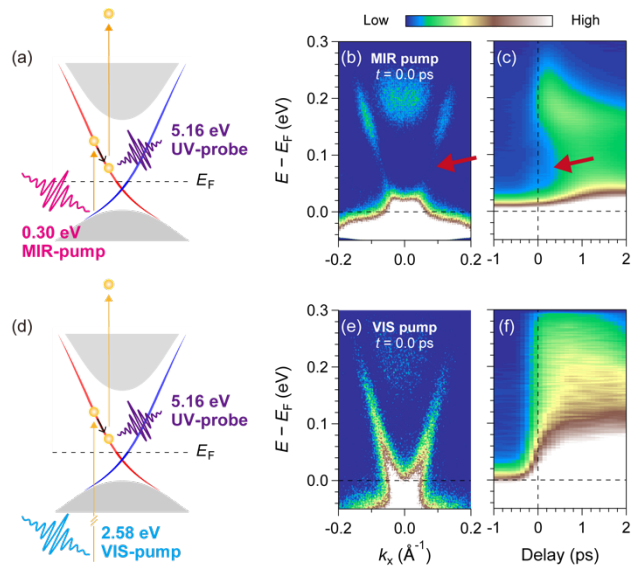


FIGURE 1. (a) Schematic illustration of time-resolved ARPES experiment using MIR-pump and UV-probe. (b) ARPES image of (Sb_{0.57}Bi_{0.43})₂Te₃ along $\bar{\Gamma} - \bar{K}$ direction recorded at $t = 0$ ps. (c) Photoemission intensity profile as a function of delay time. (d-f) Same as (a-c) but using VIS-pump.

at the TSS in a certain energy region around 0.05 eV are very weak [see the red arrow in Fig. 1(b)], while those around 0.15 eV are pronounced. To illustrate the temporal evolution of the bands, Figure 1(c) displays the momentum-integrated photoemission intensity profile as a function of delay time. We find a dip structure around 0.05 eV from 0.0 to 0.5 ps. After 0.5 ps, the intensity around 0.05 eV drastically increases because the photo-excited electrons at higher energy states relax through intra-band and inter-band scatterings. These findings suggest that the direct transition is prohibited around 0.05 eV in the MIR-pump scheme. To compare the ultrafast carrier dynamics, we also performed time-resolved ARPES using the VIS-pump [Figs. 1(e) and 1(f)]. However, in sharp contrast to the MIR-pump scheme, no dip structures are visible at $t = 0$ ps.

Since the forbidden transition observed in the MIR-pump scheme likely stems from the unique spin texture of the TSS, we proceeded with the spin-resolved measurement of the occupied bands below E_F . Figure 2(a) shows the spin-resolved ARPES image captured at 17.0 eV. Red and blue colors correspond to positive and negative in-plane spin-polarization, respectively. From E_F to -0.3 eV, the spin-polarized lower portion of TSS is evident. Additionally, M-shaped spin-split Rashba bands are observed around -0.5 eV. Since the directions of in-plane spin-polarization at the upper and lower TSSs are reversed with respect to the Dirac point, the forbidden transitions in the “resonant” MIR-pump scheme are most likely caused by the intrinsic spin texture of TSS, as depicted in Fig. 2(b). In the VIS-pump scheme, on the other hand, the direct transition to the upper TSS is allowed because the transition occurs from the unpolarized deeper-lying bulk continuum states. Finally, we discuss why the direct transition is permitted around 0.15 eV at the TSS in the MIR-pump scheme [Fig. 1(b)]. The upper panels of Fig. 2(c) show the constant energy contours recorded at $t \sim 0$ ps with VIS-pump. At 0.05 eV, an isotropic shape contour is seen. On the other hand, at 0.15 eV, the contour shape undergoes deformation from circular to hexagonal due to the warping effect. On the warped bands, it is known that not only in-plane but also out-of-plane spin components emerge [the lower panels of Fig. 2(c)] [5]. In such a case, the direct transition would be partially allowed.

In conclusion, we have experimentally demonstrated the spin-dependent forbidden transition in the TI by using time-resolved ARPES and spin-resolved ARPES. Our findings pave the way for ultrafast opto-spintronic applications using the TSS of TIs.

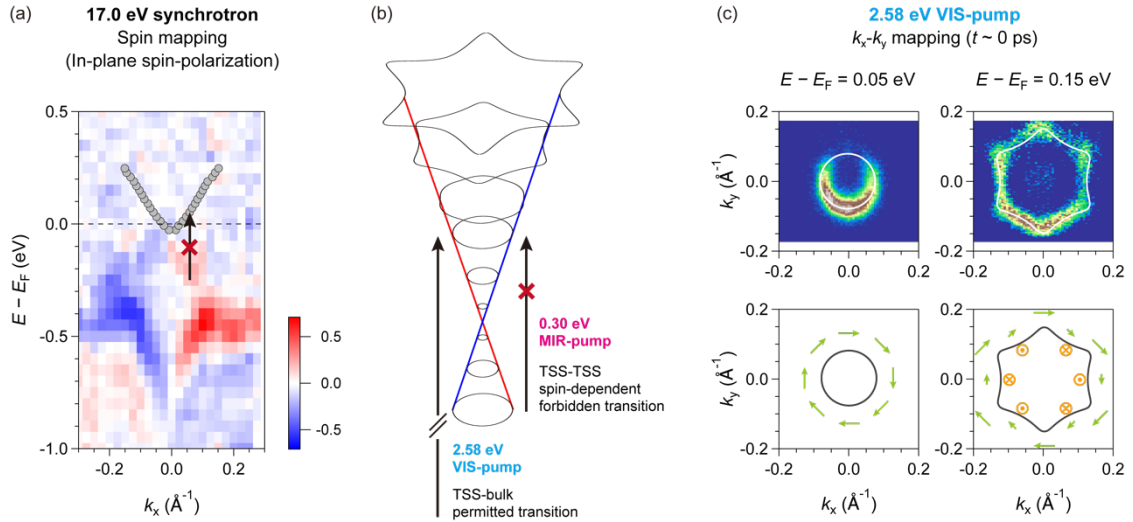


FIGURE 2. (a) In-plane spin-polarization mapping of $(\text{Sb}_{0.57}\text{Bi}_{0.43})_2\text{Te}_3$ along $\bar{\Gamma} - \bar{K}$ direction recorded at 17.0 eV. Gray circles represent the fitting results of the TSS shown in Fig. 1(e). (b) Schematic illustration of spin-dependent direct transition using MIR- and VIS-pump schemes. (c) Upper panel: constant energy contours at 0.05 and 0.15 eV recorded at $t \sim 0$ ps with VIS-pump. Lower panel: Schematic illustrations of spin texture of isotropic (left) and anisotropic TSS (right). Light green and orange colors correspond to the in-plane and out-of-plane spin components, respectively.

REFERENCES

1. Y. H. Wang *et al.*, *Science* **342**, 453 (2013).
2. S. Y. Zhu *et al.*, *Sci. Rep.* **5**, 13213 (2015)., K. Sumida *et al.*, *Phys. Rev. B* **99**, 085302 (2019).
3. K. Sumida *et al.*, *Sci. Rep.* **7**, 14080 (2017)., T. Yoshikawa *et al.*, *Phys. Rev. B* **100**, 165311 (2019).
4. T. Okuda *et al.*, *Rev. Sci. Instrum.* **82**, 103302 (2011).
5. L. Fu, *Phys. Rev. Lett.* **103**, 266801 (2009)., S. Souma *et al.*, *Phys. Rev. Lett.* **106**, 216803 (2011).

Demonstration of phase-resolved spin-ARPES on topological surface states in Bi_2Te_3

Towa Kouza^a, T. Iwata^{a,b}, S. Kumar^c, A. Kimura^{a,b},
K. Miyamoto^c, T. Okuda^{b,c} and K. Kuroda^{a,b}

^aGraduate School of Advanced Science and Engineering, Hiroshima University, 1-3-1 Kagamiyama, Higashi-Hiroshima 739-8526, Japan.

^bInternational Institute for Sustainability with Knotted Chiral Meta Matter(WPI-SKCM²), Hiroshima University, Higashi-Hiroshima 739-8526, Japan.

^cHiroshima Synchrotron Radiation Center, Hiroshima University, 2-313 Kagamiyama, Higashi-Hiroshima 739-0046, Japan

Keywords: Spin-orbit coupling, Topological surface states, Ultrafast dynamics

Optical transition such as photoemission takes place in attosecond scale (1 as = 10^{-18} s). It is very interesting to phenomena in the attosecond region from point of view of the pursuit of ultimate understanding of quantum mechanics and pioneering electronics that can be controlled on as-time-scale. Great development of ultrashort pulse laser technology over the past few decades has permitted to track the ultrafast dynamics as the attosecond scale in the time domain [1-4]. However, the ultrashort pulse nature of the attosecond pulse diminished energy resolution because of a trade-off relationship between the pulse width in time and frequency domains. This means that it is difficult to experimentally trace the ultrafast photoemission dynamics together with resolving valance band structures.

In this work, to overcome the above difficulty, we attempted phase-resolved spin-ARPES [5-7] by laser-based angle-resolved photoelectron spectroscopy with 3D spin detection. Using this technique, we accessed phase information in the transition matrix of the photoelectron states and its kinetic energy dependence that can be converted to the time scale of photoemission dynamics in as-time-scale [8]. For this measurement, a picosecond laser was used to achieve a 20-meV energy resolution for spin-ARPES and 3D spin detection was used for the delay phase determination[9]. In addition, we built a polarization rotation control system that allows us to perform the automatic spin-ARPES measurements collecting a number of data points.

We studied the spin polarization of the photoelectrons emitted from the topological surface state of the typical topological insulator Bi_2Te_3 . The topological surface state is ideal for this experiment because they form fully spin-polarized electronic states that are locked to be a helical texture in momentum space. Let us also note that the spin-polarization of the photoelectron is collected on the mirror plane [Fig.1(a)], and therefore the orbital selection rule is allowed in the photoemission process. Owing to these simple experimental geometry, one can selectivity excite either *even* or *odd* orbital function that is coupled to different spin wavefunction [10] and superimposes these two dipole matrixes with the different spin in photoelectron final state, resulting in the rotation of the spin polarization axis [5-7]. This process is schematically summarized in Fig1.(b).

Though this process, the spin-orbit coupled wavefunction in the topological surface states allows us to selectively excite the spin and control its direction by photon polarization. Furthermore, the spin direction as a function of the photon polarization sensitivity depends on the relative phase between the two matrix elements, which therefore allows us to extract the phase from our spin-ARPES data. The extracted relative phase ϕ between two transition is used for time conversion according to the Eisenbud-Wigner-Smith (EWS) model [1,11] :

$$\tau_{EWS} = \hbar \frac{\partial \phi}{\partial E_k} \quad (1)$$

where τ_{EWS} is a time delay obtained in the EWS-model, and E_k is kinetic energy of the photoelectron.

Fig2.(a) represents a Fermi surface and ARPES of the topological surface states in Bi₂Te₃. Fig2.(b) represents the results of photoelectron spin interference performed at each of wavenumbers $k_1 \sim k_4$ in Fig2.(a). Also, we just give a brief description here, a slight correlation is observed between each phase and kinetic energy, indicating that phase decomposition is possible. Using its data and Eq.(1), we obtained the result that the delay time $\tau_{EWS} = 1.29 \times 10^{-18}$ s.

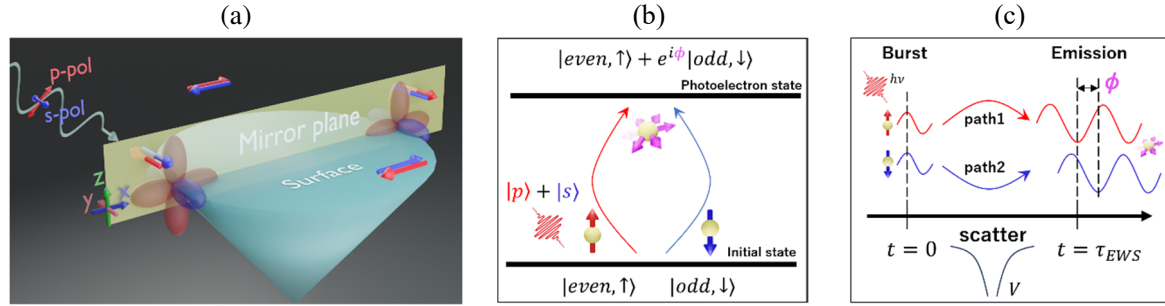


[Fig1.] (a) Electron orbitals and spins of topological surface states on the mirror plane. (b) Concept of photoelectron spin interference. (c) Concepts that tie our work to EWS model [5-7,11]. The wave packets of two transition are scattered differently as they pass through the potential V , therefore ϕ occurs between the two transitions. We noted that ϕ is extracted for each E_k and τ_{EWS} is calculated from Eq.(1).

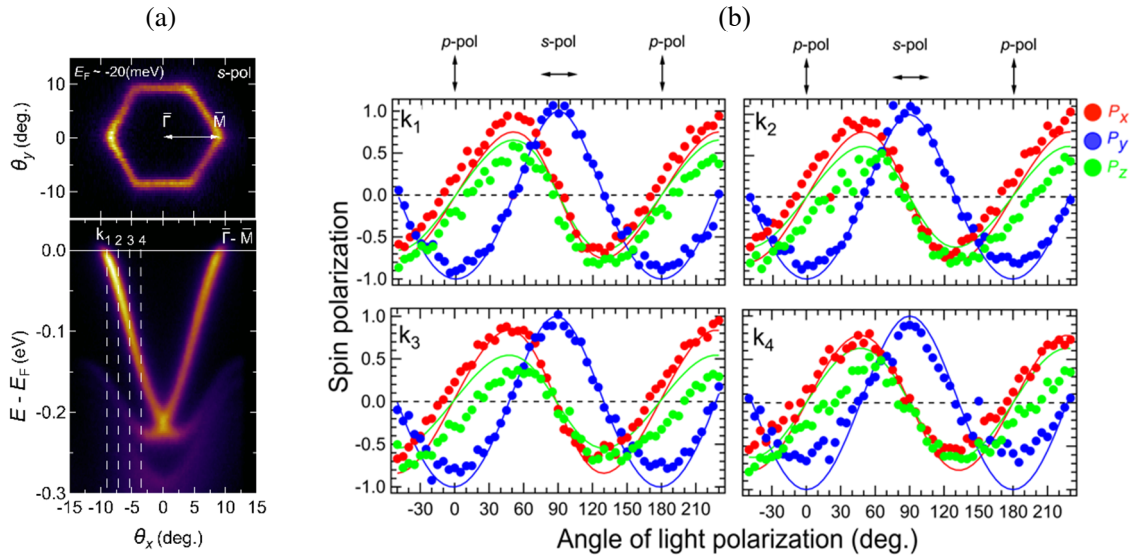


[Fig2.] (a) ARPES of topological surface states in Bi₂Te₃. Temperature is 40~50K. Photon energy is 6.3eV. Photon is linear polarization. $k_1 \sim k_4$ are wavenumber of each spin detection. Clean surface was obtained by cleaving in 7.3×10^{-8} Pa. The mirror plane ($\Gamma - M$ direction), the detection plane and the slit direction are all parallel. (b) Spin detection with polarization rotation at binding energies corresponding to each wave number. $S_{\text{eff}} = 0.27$. The dots are experimental values, and the solid lines are model fittings [5-7].

REFERENCES

1. E. P. Wigner, Phys. Rev vol **98** 145 (1955).
2. Paul, P. M *et al.*, Science **292**, 1689-1692 (2001).
3. Hentschel, M *et al.*, Nature **414**, 509-513 (2001).
4. Schultze, M *et al.*, Science **328**, 1658-1662 (2010)
5. K. Kuroda *et al.*, Phys. Rev. **94**, 165162 (2016)
6. K. Kuroda *et al.*, Phys. Rev. B. **105**, L121106 (2022)
7. K. Yaji *et al.*, Nature. communications. **8**, 14588 (2017)
8. M. Fanciulli *et al.*, Phys. Rev. Lett. **118**, 067402 (2017)
9. T. Iwata *et al.*, Scientific Reports 14:127 (2024)
10. J. Henk *et al.*, Phys. Rev. B. **68**, 165416 (2003)
11. F. T. Smith *et al.*, Phys. Rev. **118**, 349 (1960)

Performance of laser-based SARPES with micrometer spatial and vector spin resolution at HiSOR

^{A, B} Takuma Iwata, ^A T. Kousa, ^A Y. Nishioka, ^A K. Ohwada, ^C K. Sumida,
^D E. Annese, ^A M. Kakoki, ^{A, B} K. Kuroda, ^E H. Iwasawa, ^C M. Arita, ^C S. Kumar,
^{A, B} A. Kimura, ^C K. Miyamoto and ^{B, C} T. Okuda

^A *Grad. Sch. Adv. Sci. Eng., Hiroshima Univ. 1-3-1 Kagamiyama, Higashi-Hiroshima 739-8526, Japan*

^B *WPI-SKCM², Hiroshima Univ., 2-313 Kagamiyama, Higashi-Hiroshima, Japan 739-0046*

^C *HiSOR, Hiroshima Univ. 2-313 Kagamiyama, Higashi-Hiroshima 739-0046, Japan*

^D *Brazilian Center for Research in Physics, Rua Dr. Xavier Sigaud 150,*

Rio de Janeiro, RJ 22290-180, Brazil

^E *Institute for Advanced Synchrotron Light Source, National Institutes for Quantum Science and
Technology, Sendai 980-8579, Japan*

Keywords: Spin-and angle-resolved photoemission spectroscopy, electronic structure, spin polarization, momentum space

Angle-resolved photoemission spectroscopy (ARPES) is a powerful tool to directly observe the electronic structure of solids. In recent years, micro-ARPES [1] which is combined with a micro-focused light source has attracted much attention, since it is found to be very useful to explore the electronic states in newly topological materials [2], phase-separated correlated systems [3] and transition samples [4].

Spin-resolved ARPES (SARPES) [5] enables us to detect not only the energy and momentum but also the spin of photoelectrons owing to recent development of the spin detectors. However, micro-SARPES measurement has never been reported so far, because of the difficulties of the spin detection and its combination technique. Synchrotron Radiation is a conventional light source used for SARPES. Although there are some synchrotron radiation based micro- (or nano-)ARPES systems, the use of special optical elements (such as Fresnel zone plate) attenuate intensity of light and the need for a mechanism to control the optical system under ultrahigh vacuum condition make micro-SARPES a difficult and still developing technology.

In this context, we employed a high-photon flux ultraviolet laser with 6-eV of photon energy instead of synchrotron radiation to realize micro-SARPES. In addition to high photon flux, the advantage of the 6-eV laser is the flexibility of its optical system due to high atmospheric transmission. Since SARPES requires an intense light source to perform high resolution measurements, we considered a laser to be the best light source for micro-SARPES. Therefore, we combined a high-intensity 6-eV laser with a high-efficiency spin detector at HiSOR to develop micro-SARPES machine that can perform high-efficiency spin-resolved experiments while maintaining micro-focusing.

In this presentation, we will describe the performance of the state-of-the-art micro-SARPES machine combining 6-eV laser source and the photoelectron analyzer equipped with the electron deflector function and two VLEED type spin detectors [6]. We evaluated spatial resolution and long-time stability using an Au polycrystalline letter pattern (“ μ -SARPES”) sample, which is fabricated on a Si substrate using photo lithography (Fig. 1). We performed not only 3D spin-resolved experiment to Bi₂Te₃, which is a typical topological insulator as a test sample, but also spin- and spatial-resolved experiment to PbBi₄Te₄S₃ [7], which has two Dirac-cone-like dispersions derived from two distinct terminations (Fig. 2).

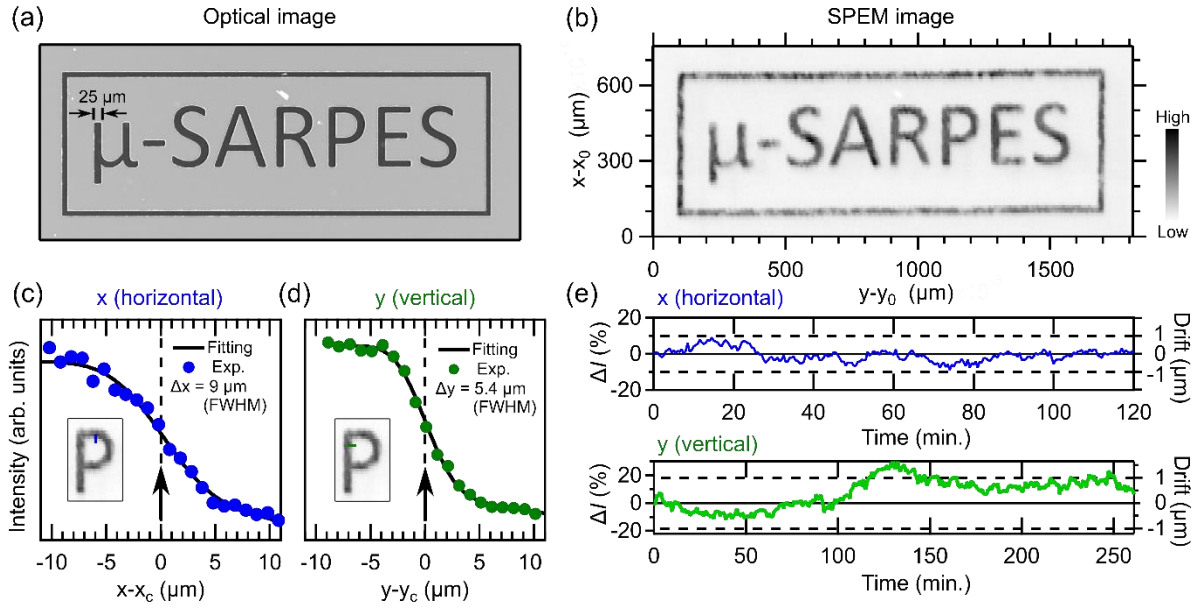


FIGURE 1. Characterization of the spatial resolution. (a) The optical microscope image of the Au pattern on the Si (001) substrate. (b) The image of the scanning photoelectron intensity map (SPEM) taken in the Au pattern. (c) and (d) Photoelectron intensity profiles at the edges of the Au pattern along the x (horizontal) and y (vertical) axes, respectively (green and blue lines in the insets). (e) Plots of the intensity deviation $\Delta I(x)$ and $\Delta I(y)$ as a function of time to evaluate possible long-term drifts of the laser and the sample stage. The data was recorded at the intensity edge at x_c and y_c denoted by arrows in (c) and (d). The 1- μm of the drift along x (y) axis can correspond to 19% (10%) of $\Delta I(x)$; $[\Delta I(y)]$ guided by dashed lines.

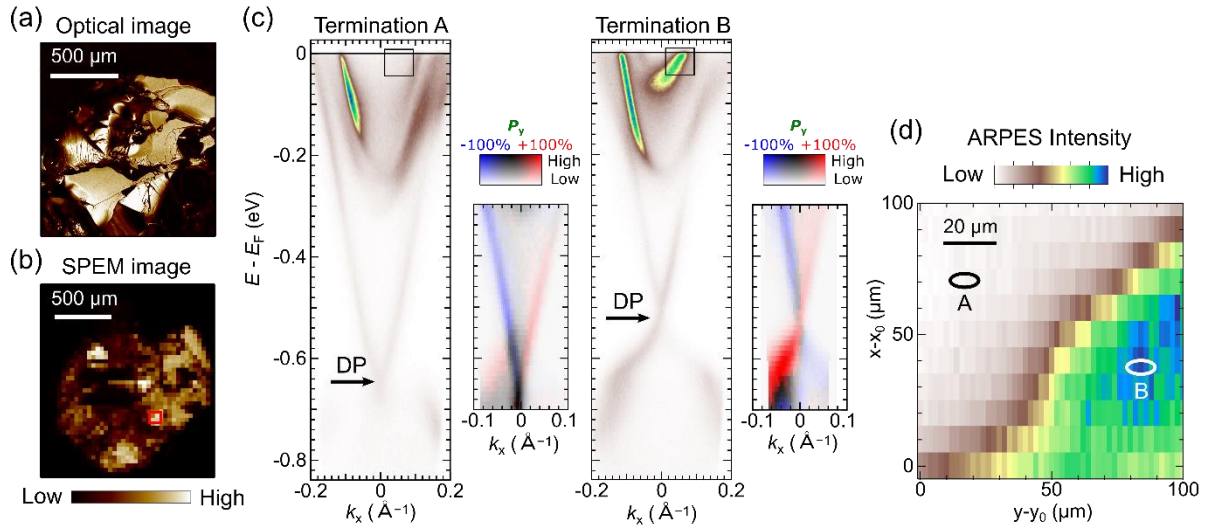


FIGURE 1. Demonstration of spatially-resolved SARPES measurements on $\text{PbBi}_4\text{Te}_4\text{S}_3$. (a) Optical microscope image of a cleaved surface of $\text{PbBi}_4\text{Te}_4\text{S}_3$. (b) SPEM image taken with a 50 μm step. (c) Spatially-resolved ARPES images acquired at different surface terminations [7]. (d) Scanning ARPES intensity map measured at the $100 \times 100 \mu\text{m}$ marked by the red square in (b). The map is taken by scanning 2 μm and 10 μm steps along x and y axes, respectively.

REFERENCES

- [1] H. Iwasawa *et al.*, *Ultramicroscopy*, **182**, 85 (2017).
- [2] R. Noguchi *et al.*, *Nature*, **566**, 518 (2019).
- [3] K. Kuroda *et al.*, *Nature Communications*, **11**, 2888 (2020).
- [4] I. Cucchi *et al.*, *Nano Letters*, **19**, 554 (2019).
- [5] T. Okuda *et al.*, *J. Phys.: Condens. Matter*, **29**, 483001 (2017).
- [6] T. Iwata *et al.*, *Scientific Reports*, **14**, 127 (2024)
- [7] K. Sumida *et al.*, *Physical Review materials*, **2**, 104201 (2018)

Direct Observation of Spin-split Electronic Structures in Antiferromagnet NdBi by Laser-based SARPES

Rikako Yamamoto^a, T. Motoyama^b, T. Iwata^{a,b}, T. Kosa^b, Y. Nishioka^b,
K. Ideura^b, M. Arita^c, S. Ideta^c, K. Shimada^{a,c}, K. Miyamoto^c,
T. Okuda^{a,c}, A. Kimura^{a,b}, T. Onimaru^b, and Kenta Kuroda^{a,b}

^a*International Institute for Sustainability with Knotted Chiral Meta Matter (WPI-SKCM²),
Hiroshima University, Higashi-Hiroshima 739-8526, Japan*

^b*Graduate School of Advanced Science and Engineering, Hiroshima University,
1-3-1 Kagamiyama, Higashi-Hiroshima 739-8526, Japan*

^c*Hiroshima Synchrotron Radiation Center, Hiroshima University,
2-313 Kagamiyama, Higashi-Hiroshima 739-0046, Japan*

Keywords: rare-earth monopnictide, spin-resolved and angle-resolved photoemission spectroscopy, spin textures

Rare-earth monopnictides RX (R : Rare-earth, X : N, P, As, Sb, and Bi) have attracted much attention because of their topological electronic structures [1,2] and unusual magnetic transitions [3,4]. Recently, unconventional surface states have been reported in the antiferromagnet NdBi. The surface states, consisting of sharp Fermi-arc-like hole bands and electron bands near Fermi energy E_F , appear below the antiferromagnetic (AFM) transition at $T_N = 24$ K [5]. Density functional theory calculations suggest that the multi-q magnetic structures induce the surface states inside the band-folding hybridization bulk gap [6]. Although the discovery of the unconventional surface states stimulates intense discussion on their origin, the key information on the spin polarization is still missing.

Here, we investigated the electronic structure and the spin polarization of the unconventional surface states. The experiments were performed synchrotron-based angle-resolved photoemission spectroscopy (ARPES) by BL-1 and BL-9A and laser-based spin-resolved ARPES (SARPES) at Hiroshima Synchrotron Radiation Center. The Fermi surface in the paramagnetic state has a square and a surrounding rhomboid hole pocket centered in the Brillouin zone. On cooling below T_N , the electronic structure is reconstructed and the surface states appear, which is consistent with previous reports [7,8]. In addition, we successfully observed different electronic structures depending on the magnetic domain: while the electron bands were recognized along the k_x direction, those appear along perpendicular to the k_x direction in different measurement areas. To obtain the spin information of the surface state, we conducted SARPES measurements. It is revealed that spin polarization for the hole and electron bands emerging in the AFM state is the opposite: the hole and electron bands show negative and positive spin polarization, respectively. Moreover, the spin-resolved measurements of the in-plane spin component demonstrated spin polarizations exceeding $\pm 50\%$. Our results fill the gap between experimental and theoretical studies and enable us to further understand the origin of the unconventional surface states.

REFERENCES

1. J. Nayak *et al.*, Nat Commun. **8**, 13942 (2017).
2. K. Kuroda *et al.*, Phys. Rev. Lett. **120**, 086402 (2018).
3. K. Kuroda *et al.*, Nat Commun. **11**, 2888 (2020).
4. Y. Arai *et al.*, Nat. Mater. **21**, 410 (2022).
5. B. Schruck *et al.* Nature **603**, 610 (2022).
6. LL. Wang *et al.*, Commn. Phys. **6**, 78 (2023).
7. Y. Kushnirenko *et al.*, Phys. Rev. B **108**, 115102 (2023).
8. A. Honma *et al.* Nat Commun. **14**, 7396 (2023).

21AG028, 21BU002, 22AG009

BL-12

Secondary Structural Changes of FUS-LC induced with Phase-Separation observed by VUV-CD

Kentaro Fujii^a, Nobuo Maita^a, Koichi Matsuo^b, and Masato Kato^a

^a*Institute for Quantum Life Science, National Institutes for Quantum Science and Technology,
4-9-1 Anagawa, Inage-ku, Chiba-city, Chiba, 263-8555 JAPAN*

^b*Hiroshima Synchrotron Radiation Center, Hiroshima-university,
2-313 Kagamiyama, Higashihiroshima-city, Hiroshima, 739-0046 JAPAN*

Keywords: Liquid-Liquid Phase Separation, FUS-LC, Secondary structural changes.

Aggregation of the RNA-binding protein FUS (Fused in Sarcoma) has been implicated in neurodegenerative diseases such as ALS (amyotrophic lateral sclerosis) and FTD (frontotemporal dementia). The low-complexity domain of the FUS (FUS-LC) mediated liquid-liquid phase separation (LLPS), but the structural mechanism is not known in detail. To address the revealing mechanism, we examined the spectroscopic study using VUV-CD measurement, which can analyze the secondary structure of the proteins.

CD measurements were performed at BL12 VUV-CD station in HiSOR. CD spectra were measured between 185 and 260 nm. The temperature of the samples was controlled from room temperature to 5°C to obtain the LLPS of the FUS LC.

The CD spectrum obtained by measuring at room temperature has a prominent peak at 195 nm and a small shoulder peak near 220 nm. This shows that the major structure is a random coil since the spectrum was similar to that of STI, which is mainly an unordered structure. This result is consistent with that obtained from NMR measurement. The peak intensity around 195 nm decreased by cooling the sample temperature.

The reasons for the obtained spectral changes are as follows; 1) LLPS showed secondary structural changes, 2) LLPS made an effect to decreasing the transmission light intensity by scattering of suspension. We examine the measurement by changing the relative distance between the cell and the photo-multiplier detector. This may clarify the contribution of the scattering effect on the obtained spectrum.

Insights into Physical Interactions and Structuration in Self-Assembled Azapeptide Hydrogels Through Spectroscopy Techniques

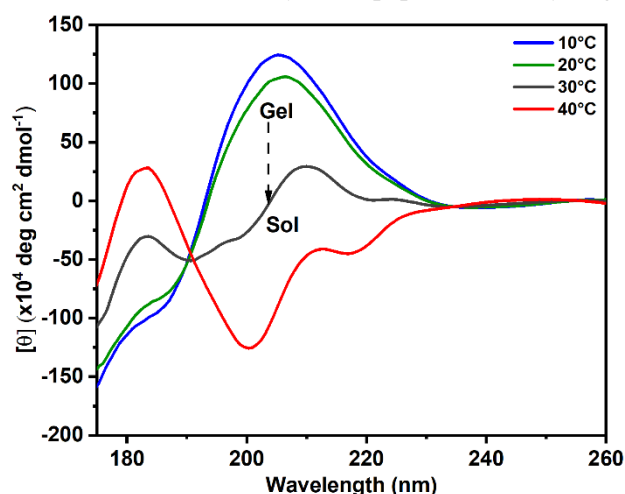
Mohamed Ibrahim^{a,b}, Jacques Bodiguel^b, Marie-Christine Averlant-Petit^b, and Koichi Matsuo^a

^aHiroshima Synchrotron Radiation Center (HiSOR), Hiroshima University, 2-313 Kagamiyama, Higashi-Hiroshima, Hiroshima 739-0046 Japan.

^bUniversité de Lorraine, CNRS, LCPM, F-54000 Nancy France.

Keywords: Self-Assembly, Azapeptides, Hydrogels, Circular Dichroism.

Self-assembly is a captivating phenomenon within supramolecular chemistry, triggering the formation of hydrogels stabilized by non-covalent interactions including hydrogen bonding, π - π stacking, electrostatic interactions, and hydrophobic forces. Supramolecular gels-based low molecular weight molecules find applications in tissue engineering, drug delivery, biosensing, and catalysis [1]. Azapeptides, characterized by their nitrogen atoms, offer unique functionalities and stability, rendering them ideal for the fabrication of supramolecular hydrogels [2, 3]. In this study, two hydrogelator molecules derived from azapeptide family were designed, and structurally elucidated using various spectroscopic techniques. NMR, FTIR, UV-Vis, fluorescence, SEM, and rheology experiments were conducted to explore molecular, supramolecular, mechanical features. In solution, both molecules exhibit monomeric states adopting β -turn conformation stabilized by intramolecular hydrogen bonding, while the supramolecular structure (as revealed by X-ray crystallography) is stabilized mainly through intermolecular hydrogen bonding and π - π stacking (data is not shown). In the gel state, circular dichroism (CD) spectroscopy, is crucial for understanding the secondary structure and self-assembly of azapeptide-based hydrogels [4]. This study sheds light on the conformational changes occurring during the self-assembly process.



For example, the temperature dependent experiment revealed the gel-sol transition associated with conformational changes (see **Figure 1**). By integrating principles from supramolecular chemistry, innovative azapeptide design strategies, and sophisticated spectroscopic methodologies, the development of functional hydrogels with tailored properties for diverse applications becomes achievable.

FIGURE 1. Temperature-dependent SRCD spectrum of azapeptide hydrogel ($c = 0.8$ w/w%, $\text{pH} = 7.0$).

REFERENCES

1. M. J. Webber, E. A. Appel, E. W. Meijer, R. Langer, *Nature Materials*, 2016, **15**, pp. 13–26.
2. F. Rodríguez-Llansola, B. Escuder, J.F. Miravet, *Chemical Society Reviews*, 2015, **44**, pp. 6058–6071.
3. E. R. Draper, M. Wallace, S. Ladame, *Chemical Society Reviews*, 2020, **49**, pp. 7134–7171.
4. N. Berthet, P. Dugourd, R. Antoine, S. Lecomte, *Chirality*, 2019, **31**, pp. 458–476.
5. M. I. A. Ibrahim, G. Pickaert, L. Stefan, B. Jamart-Grégoire, J. Bodiguel, M.-C. Averlant-Petit, *RSC Advances*, 2020, **10**, pp. 43859–43869.

Monitoring the Self-Assembly of Alginate Hydrogel Using Synchrotron Radiation Circular Dichroism

Tatsuki Haga^a, Masaya Yoshida^a, Takeharu Haino^a, Koichi Matsuo^b and Mohamed I.A. Ibrahim^b

^a*Graduate School of Advanced Science and Engineering, Hiroshima University.*

^b*Hiroshima Synchrotron Radiation Center (HiSOR), Hiroshima University, 2-313 Kagamiyama, Higashi-Hiroshima, Hiroshima 739-0046 Japan.*

Keywords: Alginate, Hydrogel, Self-Assembly, CD, AFM

Circular dichroism (CD) spectroscopy, traditionally used for studying the secondary structure of proteins and peptides [1], has not been yet established for studying polysaccharides (PSs). The current study has explored the potential of using CD in structural changes associated with PS hydrogelation. Certain PSs can change from a liquid to a gel when exposed to light, ions, or temperature. Alginate, an ecofriendly and nontoxic PS used in medicine and food, is especially known for forming hydrogels when mixed with polyvalent ions [2]. In the food industry, alginate serves as an additive to enhance texture and shape. This function is closely related to the conformational changes during sol-gel transitions, so structural analysis of alginate is helpful for maximizing its function as an additive.

Herein, CD experiments using synchrotron radiation (SR) light were carried out to investigate the structural changes associated with gel formation in the presence and absence of metal ions. Monovalent ions such as Na⁺, K⁺, and Li⁺ did not induce hydrogel formation, whereas hydrogels were obtained by divalents (e.g., Ca²⁺, Ba²⁺, Cu²⁺, and Zn²⁺), as well as trivalent ion (e.g., Fe³⁺). The cations exhibited different influences on the native conformation of alginate, suggesting variations in the assembly of the alginate chains in the presence of different ions. Additionally, discrepancies in CD spectra reflected that the formed hydrogels possessed diverse mechanical, physical properties, and morphology.

The formulation of hydrogels is an evidence of the self-assembly phenomenon. Alginate chains are interconnected, forming a cross-linked 3D-network structure that entraps water molecules, leading to hydrogel formation. Hence, to construct the self-assembly/gel phase diagram based on the CD observations, concentration-dependent experiments, varying alginate concentrations or polyvalent ion concentrations (i.e., Ca²⁺), were conducted using a CD spectrometer. The concentration of the polyvalent ion that causes no change in the CD spectrum of alginate or that self-assembly of alginate chains was terminated (**Figure 1**, left) was marked as the initiation of aggregation. As a result, a Ca²⁺ concentration of 1.56 mM, at 1.0 mg/ml alginate concentration, was referred to the transition concentration from the self-assembly to aggregation which is followed by hydrogel formation (**Figure 1**, right). This finding was reinforced by atomic force microscopy (AFM) imaging, which showed increased cross-linking and thickness of fibers at higher Ca²⁺ concentration (2.5 mM) (**Figure 2**).

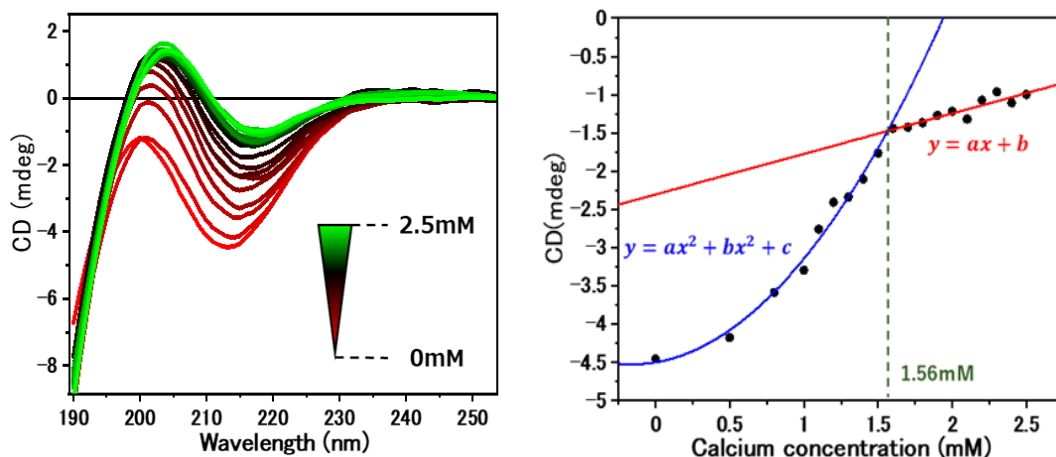


FIGURE 1. CD spectrum of alginate (1.0 mg/ml) as a function of Ca^{2+} concentrations (0.5 mM ~ 2.5 mM) (left), and self-assembly transition diagram based on CD observations (right).

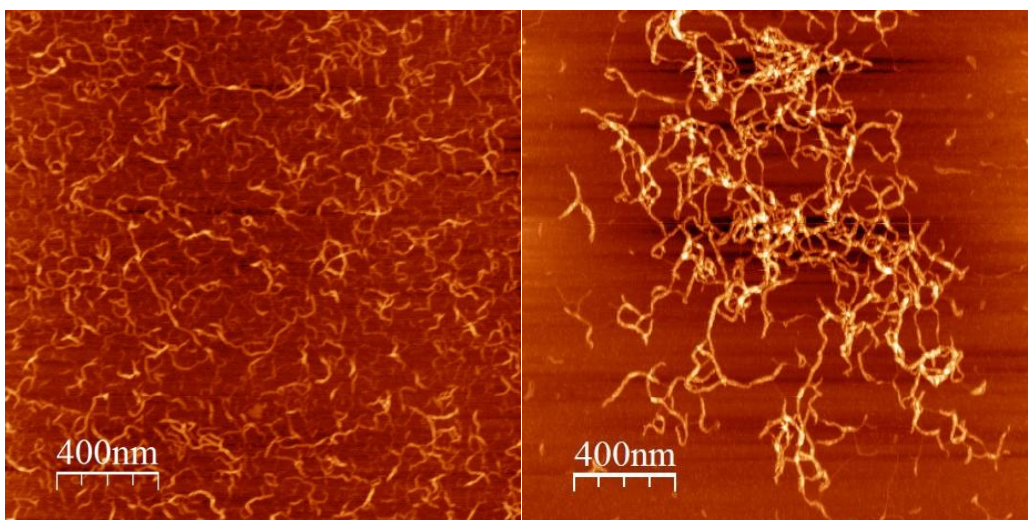


FIGURE 2. AFM images of the alginate- Ca^{2+} system with [alginate] = 1.0 mg/ml and Ca^{2+} concentrations of 1.0 mM (left), or 2.5 mM (right).

Ongoing investigations are underway to further explore the alginate- Ca^{2+} hydrogel system using SRCD, aiming to study the kinetics and thermodynamics of hydrogelation process.

REFERENCES

- [1] K. Matsuo, G. Kuniyoshi, *Bulletin of the Chemical Society of Japan*, 2013, **86**, 675-689.
- [2] J. Brus, M. Urbanova, J. Czernek, *Biomacromolecules*, 2017, **18**, 2478-2488.

VUVCD Measurements of dried proteins and its application to protein-membrane interaction study

Kosuke Hayashi^a, Ryota Imaura^a, and Koichi Matsuo^{a,b}

^aGraduate School of Advanced Science and Engineering, Hiroshima University

^bHiroshima Synchrotron Radiation Center, Hiroshima University, Hiroshima University

Keywords: circular dichroism, G3LEA protein, membrane, spin coat, secondary structure

Proteins in the dry state are utilized in various fields such as pharmaceuticals and food science. It is known that the structural differences between the liquid and dry states are slight for globular proteins [1], but intrinsically disordered protein undergoes a structural alternation from non-regular to regular structures during the dry process, expressing some unique biological functions. Hence, the elucidation of the relationships between the structural alternation and the function expression is attractive targets. In this study, we measured some globular proteins in the dry state using a vacuum-ultraviolet circular dichroism (VUVCD) spectroscopy, which is the powerful tool for secondary structure analysis of proteins, to discuss the preparations methods of dried proteins. Further, we measured the VUVCD spectra of dried G3LEA protein, which has the structural alternation from disordered structure in liquid state to helical structure in the dry state, expressing a protective function of cell membrane [2].

Eight types of dried globular proteins with different secondary structures were prepared by a spin coating technique and a vacuum drop casting method. As expected, the spin coating can suppress the surface inhomogeneity of the samples compared the drop casting, depressing the artifact within the CD data due to linear dichroism, which were confirmed by the suppression of rotation and inversion CD dependence of dried samples. Dried G3LEA consisting of 22 residues were prepared by the spin coating technique and we confirmed the structural alternation from random structure in liquid state to α -helix structure in the solid state (Figure 1). The CD spectra of dried G3LEA protein were also measured in the presence of two types of liposomes which are composed of net neutral or negatively-charged phospholipids. As a result, the formation of α -helix structures was clearly observed in negatively-charged lipid liposome but not in neutral one. Furthermore, the formation of α -helix structures was further promoted in the lipid liposome of the gel phase, compared to that of the liquid crystal phase. These results indicated that the surface charge of liposome and its liposome fluidity influenced the structural alternations of dried G3LEA protein.

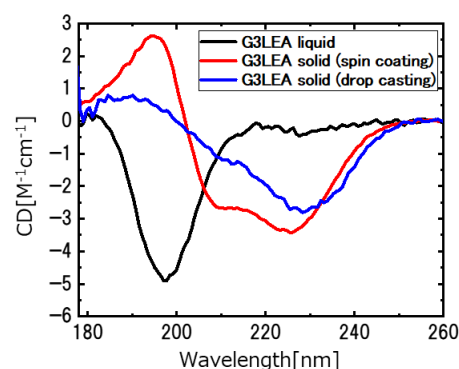


FIGURE 1 VUVCD spectra of G3LEA protein

REFERENCES

1. J.S Yoneda, A. J.Miles, A.P.U. Araujo, and B.A. Wallace, Differential dehydration effects on globular proteins and intrinsically disordered proteins during film formation, *Protein Sci.*, **26**, 718-726(2017)
2. T. Furuki, M. Sakurai, Group 3 LEA protein model peptides protect liposomes during desiccation, *Biochim. biophys. acta* **1838**, 2757-2766(2014)

Optical Activity Measurement of Circularly Polarized Lyman- α Light Irradiated and Magnetic Field Applied Amino-acid Films

Jun-ichi Takahashi^a, Masahiro Kobayashi^b, Gen Fujimori^c, Hiroshi Ota^d
Koichi Matsuo^e, Yoshitaka Taira^d, Masahiro Katoh^{d,e}, Kensei Kobayashi^{c,f}
Yoko Kebukawa^f, Hiroaki Nakamura^b

^a*Doshisha University, 1-3 Tatara Miyakodani, Kyotanabe 610-0394, Japan*

^b*National Institute for Fusion Science, 322-6 Oroshi-cho, Toki 509-5292, Japan*

^c*Yokohama National University, 79-5 Tokiwadai, Hodogaya-ku, Yokohama 240-8501, Japan*

^d*UVSOR Synchrotron Facility, 38 Nishigo-Naka, Myodaiji, Okazaki 444-8585, Japan*

^e*Hiroshima Synchrotron Radiation Center, 2-313 Kagamiyama, Higashi-Hiroshima 739-0046, Japan*

^f*Tokyo Institute of Technology, 2-12-1 Ookayama, Meguro-ku, Tokyo 152-8511, Japan*

Keywords: Homochirality, Amino Acid, Optical Activity, Circularly Polarized Light, Lyman- α , Circular Dichroism.

The origin of homochirality in terrestrial biomolecules (L-amino acid and D-sugar dominant) remains one of the most mysterious problems in the research for the origins of life. Rational explanations for the chiral asymmetry introduction into biomolecules are required through interdisciplinary collaborations. One of the most attractive hypotheses in the context of astrobiology is cosmogenic scenario; Asymmetric reactions of prebiotic molecules on interstellar dust surfaces in molecular cloud circumstances were introduced by polarized quantum radiation sources in space, that is “chiral radiations” [1, 2].

Among the polarized quantum radiation sources, circularly polarized light (CPL) in the space environment is thought to be one of the most likely causes of the enantiomeric excesses of terrestrial bioorganic molecules. A cosmogenic scenario has attracted attention, which proposes that the radiation fields of CPL induce new optical activity in organic molecules produced in the interstellar environment, leading to the enantiomeric excesses. The radiation fields of CPL are assumed to exist in the scattered light by magnetic field-aligned dust in massive star-forming regions [3] and in synchrotron radiation (SR) or gamma-ray bursts from neutron stars with strong magnetic fields [2]. Ultraviolet light with a wavelength shorter than 230 nm is highly absorbed by bioorganic molecules such as amino acids. Furthermore, this is in the region where the optical response to left- (L-) and right- (R-) CPL is of opposite sign, that is, optical activity is prominent.

To validate the cosmogenic scenario, several ground simulating experiments have been investigated using ultraviolet CPL from high-energy particle accelerators. In this study, we focused on a hydrogen Lyman- α wavelength of 121.6 nm, where strong emission lines are observed in star-forming regions. Furthermore, it is predicted by recent theoretical calculations that the hydrogen Lyman- α light is circularly polarized by the magnetic field-aligned dust scattering in massive star-forming regions. We have carried out irradiation experiments by using circularly polarized hydrogen Lyman- α light to investigate the further photon energy dependence of chiral asymmetric reactions. We formed thin solid film samples of racemic mixture of alanine (DL-alanine) on quartz substrates from crystal powders of DL-alanine by using a thermal-crucible vacuum-evaporation system. The samples were irradiated with L- or R-CPL in hydrogen Lyman- α wavelength of 121.6 nm using the undulator beam line BL1U of UVSOR-III. The irradiated CPL wavelength corresponds to photon absorption bands with the chromophores from the electronic transitions of carboxyl and amino groups (π - σ^*) of alanine molecule [4, 5]. The samples were set in a vacuum sample chamber preventing attenuation by air absorption. The 121.6 nm wavelength radiation from the undulator is reflected by a gold-coated mirror located in the mirror chamber directly beam upstream of the sample chamber and then enters the sample chamber. On the beam entrance side of the vacuum sample chamber, a gate valve with an MgF₂ vacuum sealing window (0.5 mm in thickness) was mounted. The use of gold-coated mirror reflections has

made it possible to suppress high-energy higher-order light from the undulator source expecting to reduce the transmittance loss of the MgF₂ window due to high-energy radiation induced defects. The sample substrate was set in the sample holder, in which magnetic field can be applied to perpendicularly to the sample surface (Figure 1). The total photon beam intensity irradiated on the sample was monitored with photoelectron current of a silicon photodiode settled at the beam downstream side of the sample holder.

CD spectra of the CPL irradiated films were measured using the SR-CD beam line BL-12 of HiSOR to clarify the optical activity emergence by CPL irradiation. CD spectroscopy can detect optical activity with a high accuracy because CD spectra sensitively reflects the steric structures of chiral molecules. To delete the effects of linear dichroism components, the CD spectra at sample rotation angles (0, 45, 90, and 135 degrees) from both back and front directions of each were individually measured and averaged them. We already reported the results of the first feasibility study conducted as application proposals to collaborate with UVSOR and HiSOR in FY2022 (6). The measured CD spectra of DL-alanine films irradiated with CPL at 121.6 nm in wavelength indicated the emergence of optical activity depending on the irradiated CPL polarization helicity (L- or R-CPL). In addition, we examined the effect of applying a magnetic field to the sample to investigate the effect of the magnetic field in interstellar space. Comparing with CD spectra of irradiations at 215, 180 and 155 nm in wavelength in our previous study [7, 8], the aspects of the optical activity emergence strongly depend on the irradiated CPL wavelength.

In the experiments for the FY2023 collaborative application proposals, we focused on accumulating reproducibility data of the previous FY2022 results and improving the accuracy of quantification in the quantum efficiency of the emergence of optical activity. Figure 2 shows CD spectra of DL-alanine films after right (R-) and left (L-) circularly polarized Lyman- α (121.6 nm) irradiation with magnetic field (0, ± 0.7 T). As shown in this figure, we found a clear emergence of optical activity and a significant magnetic field application effect. The clarification of full mechanism of the optical activity emergence potentially has relevance to the origin of terrestrial bioorganic homochirality stimulated by “chiral photon radiation”.

This work is supported by the Astrobiology Center Program of National Institutes of Natural Sciences (NINS) (Grant Number AB041014 and AB0515) and Frontier Photonic Sciences Project of National Institutes of Natural Sciences (NINS) (Grant Number 01212202 and 01212304).

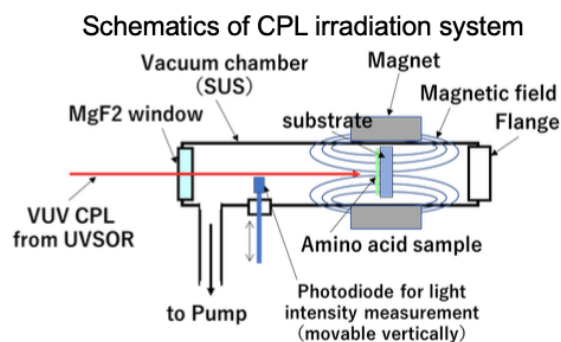


FIGURE 1. Schematic view of circularly polarized Lyman- α (121.6 nm) irradiation system.

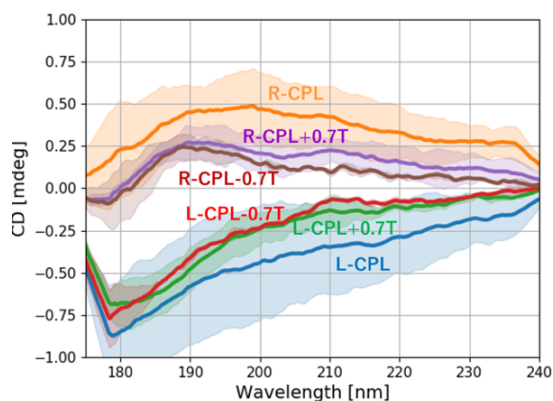


FIGURE 2. CD spectra of on DL-alanine films after right (R-) and left (L-) circularly polarized Lyman- α irradiation with magnetic field (0, ± 0.7 T).

REFERENCES

1. W. A. Bonner, *Orig. Life Evol. Biosph.* **21**, 407 (1991).
2. J. Takahashi and K. Kobayashi, *Symmetry* **11**, 919 (2019).
3. H. Fukushima, et al., *Month. Notices Roy. Astron. Soc.* **496** 2762 (2020).
4. M. Tanaka et al., *Enantiomer* **7** 185 (2002).
5. F. Kaneko et al., *J. Phys. Soc. Jpn.* **78** 013001 (2009).
6. M. Kobayashi et al., in Proceedings of A joint ISSOL/IAU-Astrobiology Commission Meeting Origins 2023, Quito, 2023.
7. J. Takahashi et al., *Int. J. Mol. Sci.* **10**, 3044 (2009).
8. J. Takahashi et al., *HISOR Act. Rep.* 2019 p.120 (2020).

Molecular orientation in polymer/fullerene blend films studied by NEXAFS

Y. Hanaki^a, H. Yoshida^{b,c} and T. Sekitani^{b,c}

^aFaculty of Science, Hiroshima University

^bGraduate School of Advanced Science and Engineering, Hiroshima University

^cHiroshima Synchrotron Radiation Center, Hiroshima University

Keywords: fullerene, polymer, solar cell, NEXAFS

With the increasing demand for renewable energy, organic photovoltaics have attracted much attention due to the low cost, lightweight and flexibility in recent years. Polymer solar cells based on bulk heterojunction (BHJ) consisting of interpenetrating networks of conjugated polymers as electron donors and fullerene derivatives as electron acceptors, are being developed for their potential application [1]. They provide a large interfacial area where efficient exciton dissociation can occur. The morphology of BHJ plays an important role in obtaining high efficiency organic photovoltaic devices. The order and orientation of the polymer backbone in the bulk heterojunction can influence device properties, such as the exciton diffusion, and charge carrier transport.

In this study, the molecular orientation of polymer/fullerene blend film was examined by near edge X-ray absorption fine structure (NEXAFS) spectroscopy. Poly-{bi(dodecyl)thiophene-thieno[3,4-c]pyrrole-4,6-dione} (PBTTTPD) was used as electron donor, and (6,6)-phenyl-C₆₁-butyric acid methyl ester (PCBM) is used as electron acceptor. Figure 1 show the molecular structures of PBTTTPD and PCBM. The blend of poly-3-hexylthiophene (P3HT) and PCBM has been used as a model system in BHJ solar cells. Compared with P3HT, PBTTTPD is co-polymer which has donor and acceptor in the main chain and the higher power conversion efficiency of PBTTTPD blend film is reported [2].

Samples for NEXAFS measurement were spin-coated on the gold coated silicon substrate from each solution. Pure PBTTTPD PCBM, and blend of PBTTTPD:PCBM (1:1.5 by weight) were dissolved in chloroform. NEXAFS measurements were performed at BL6 of Hiroshima Synchrotron Radiation Center.

Oxygen K-edge NEXAFS spectra were measured for PBTTTPD, PCBM and PBTTTPD:PCBM blend films. Figure 2 shows the NEXAFS spectra of blend films. Red line shows spectrum of normal incidence and black line shows that of grazing incidence. First strong peak come from $\pi^*_{C=O}$ resonant excitations of both PBTTTPD and PCBM. NEXAFS spectrum of blend film was well reproduced by the superposition of PBTTTPD and PCBM. From the angular dependence of $\pi^*_{C=O}$ excitation, orientation angle of each molecule was obtained. Both PBTTTPD of pure and blend films show “edge-on” orientation, which has the plane of polymer backbone perpendicular to the substrate. The effect of the coexistence of PCBM is considered small for polymer orientation which is important for charge transport process.

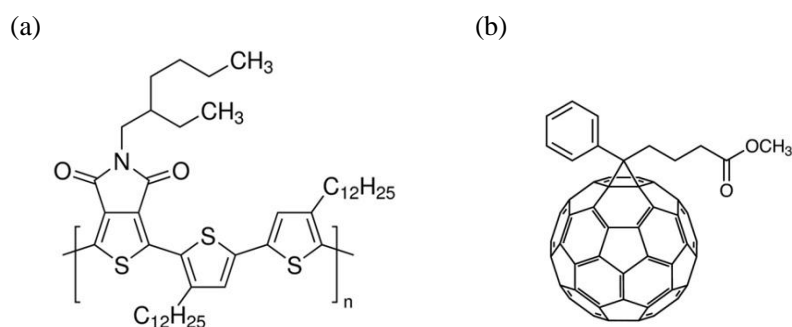


FIGURE 1. Molecular structures of (a) PBTTTPD and (b) PCBM.

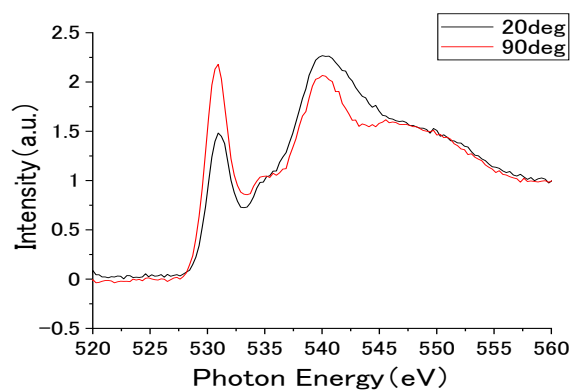


FIGURE 2. Oxygen K-edge NEXAFS spectra of PBTPPD:PCBM blend film measured at different incidence angle.

REFERENCES

1. G. Yu, J. Gao, J. C. Hummelen, F. Wudl, A.J. Heeger, *Science* **270**, 1789 (1995).
2. M. S. Su, C. Y. Kuo, M. C. Yuan, U. S. Jeng,; C. J. Su, K.-H. Wei, *Adv. Mater.* **23**, 3315 (2011)

Charge Transfer in Gold Substrates and Nanoparticles Coated with Methyl Ester Substituted Aromatic Thiol Molecules

Shogo Tendo¹, Akinobu Niozu¹, Kakuto Yoshioka¹, Jun-ichi Adachi², Hirokazu Tanaka², and Shin-ichi Wada^{1,3}

¹ Graduate School of Science and Engineering, Hiroshima University, Higashi-Hiroshima 739-8526, Japan

² Photon Factory, Institute of Materials Structure Science, KEK, Tsukuba 305-0801, Japan

³ Hiroshima Synchrotron Radiation Center, Hiroshima University, Higashi-Hiroshima 739-0046, Japan

Keywords: Self-assembled monolayers (SAMs), Gold nanoparticles, Site-selective desorption, Core-hole-clock (CHC)

Charge transfer between molecules and metal surfaces is a crucial process with implications for molecular electronics, energy storage, and catalysis. Particularly in nanoparticle films deposited on substrates, where organic molecules coat gold nanoparticles (AuNPs), charge transfer between π -conjugated molecules and metal plays a pivotal role in determining the photoelectric conversion efficiency of dye-sensitized solar cells. In this study, we focused on oligophenyl molecules, which have different molecular lengths, and directly measured the charge transfer time using soft X-rays (Figure 1 (a)–(c)) [1]. Subsequently, we elucidated the electronic properties of the nanoparticle films by comparing the charge transfer dynamics from molecules to flat metal surfaces.

Monophenyl and biphenyl self-assembled monolayers (MP and MBP SAMs, Figure 1 (a), (b)) were prepared on two different metal surfaces. The first SAMs were formed on two-dimensional flat gold substrates (2D SAMs, Figure 1 (d)). The second SAMs were formed on three-dimensional AuNPs, which were drop-cast onto the substrates (3D SAMs, Figure 1 (e)). AuNPs were synthesized by pulsed laser ablation in liquid. The size of the AuNPs was determined to be 7 nm from the surface plasmon resonant peak wavelength, as shown in Figure 2, based on the analytical equation.

Near-edge X-ray absorption fine structure (NEXAFS) spectra and X-ray photoelectron spectra (XPS) were collected at the HiSOR BL-13. The XPS results for the 2D-MP and 3D-MBP SAMs are presented in Figure 3. An important observation from XPS is the similarity in chemical shifts, with no clear discrepancy in the energy position between 2D and 3D SAMs. Any slight variations were attributed to the inhomogeneity of the NP surfaces; nevertheless, the electronic structures of the 2D and 3D SAM remained identical. Figure 4 shows the C and O K-edge NEXAFS spectra. The dominant peaks included $\pi^*(C=C)$ at ~ 285 eV for the C K-edge and $\pi^*(C=O)$ at 532.0 eV for the O K-edge. Polarization angular

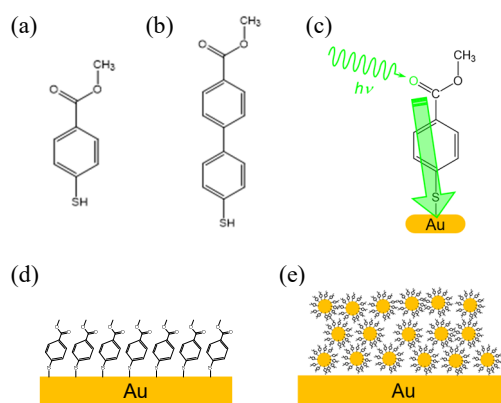


FIGURE 1. Molecular structures of (a) MP and (b) MBP. Images of (c) charge transfer process, and (d) 2D-MP, and (e) 3D-MP SAMs.

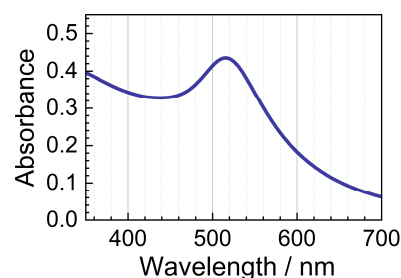


FIGURE 2. UV-VIS spectrum of AuNP colloids.

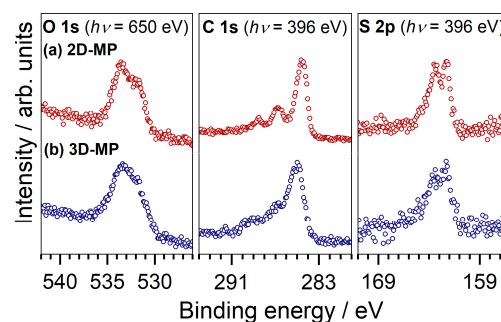


FIGURE 3. XPS of 2D-MP and 3D-MP SAMs.

dependence was observed in 2D-MP, and the subsequent fitting analysis suggested that the molecules adsorbed in an upright orientation to the surfaces [2]. In contrast, this phenomenon was not observed in 3D SAMs, likely due to the averaging of the transition dipole moment of molecules on spherical particles. The energy level of the $\pi^*(\text{C}=\text{O})$ peaks exceeded the binding energy of the $\text{C}=\text{O}$ peaks at 531.7 eV in the O 1s XPS spectra, indicating that it was suitable for subsequent resonant Auger electron spectroscopy experiments.

We conducted time-of-flight mass spectrometry (TOF-MS) at Photon Factory BL-2B and utilized the data obtained to construct near-edge X-ray absorption mass spectra (NEXAMS), as shown in Figure 5. The total ion yield (TIY) and partial ion yield (PIY) spectra for both 2D and 3D SAMs exhibited a primary peaks corresponding to $\sigma^*(\text{O}-\text{CH}_3)$ at 288.9 eV. This observation indicates that 3D SAMs form monolayers similar to those formed by 2D SAMs. The presence of a single sharp peak at 288.9 eV for CH_n^+ ($n = 0-3$) ions suggests site-selective desorption of CH_n^+ ions from the methoxy group of SAMs [3].

Resonant Auger electron spectra (RAES) were measured at HiSOR BL-13, and the charge transfer times of the 2D and 3D SAMs were determined using the core-hole-clock (CHC) approach. In Figure 6, RAES at O $1s \rightarrow \pi^*(\text{C}=\text{O})$ excitation is presented, with peaks corresponding to spectator Auger decay processes observed at ~ 486 eV and ~ 511 eV. The RAES at $\pi^*(\text{C}=\text{O})$ excitation was fitted with the RAES at post-edge excitation and $\pi^*(\text{C}=\text{O})$ excitation of 2D-aliphatic SAMs, which exhibit insulation properties. Using the fitting coefficient and core hole lifetime of O 1s, the charge transfer time for each 2D and 3D SAMs were determined. The charge transfer time of 3D SAMs decreased with increasing chain length, similar to that of 2D SAMs. Furthermore, the charge transfer time between the 2D and 3D SAMs remained unchanged.

Our results suggest that the spectroscopic and electrical properties of 3D SAMs closely resemble those of 2D SAMs. This similarity can be attributed to the fact that the AuNPs synthesized in our study had a diameter of ~ 7 nm, predominantly comprising $\{111\}$ terraces on their surfaces [4]. Notably, unique absorption features at the corners and edges of the NPs were not observed in the spectra. In essence, this study serves as a crucial link, extending the applicability of insights into the charge transfer times obtained from diverse molecules observed in 2D to the context of 3D SAMs.

REFERENCES

1. M. Zharnikov, *Acc. Chem. Res.*, **53**, 2975–2984 (2020).
2. J. Stöhr, *NEXAFS Spectroscopy*, Surface Sciences, vol. 25, Berlin, Springer, 1992.
3. S. Wada, H. Kizaki, et al. *J. Phys.: Condens. Matter*, **18**, S1629-S1653 (2006).
4. A. C. Templeton, W. P. Wuelfing and R. W. Murray, *Acc. Chem. Res.*, **33**, 27–36 (2000).

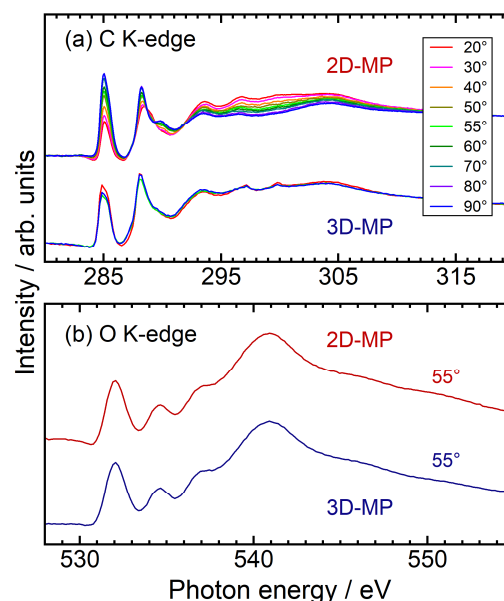


FIGURE 4. (a) Polarization dependence spectra of C K-edge NEXAFS spectra of 2D and 3D-MP. (b) O K-edge NEXAFS spectra of 2D and 3D-MP.

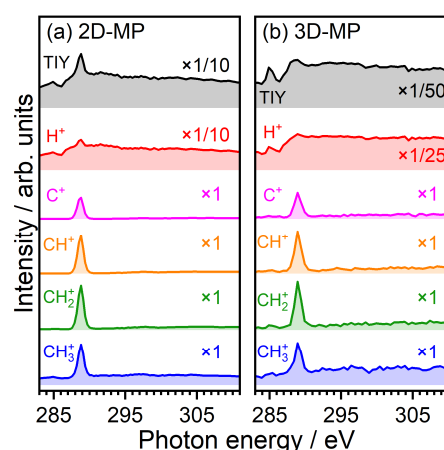


FIGURE 5. C K-edge NEXAMS spectra of (a) 2D-MP and (b) 3D-MP. Total ion yield spectra and partial ion yield spectra of major products.

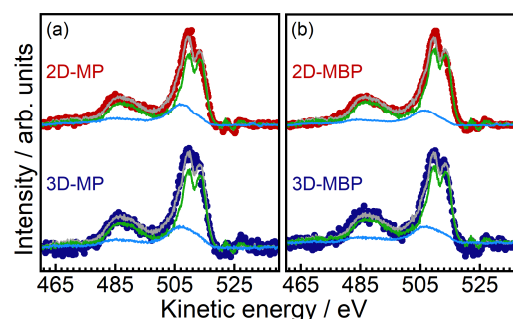


FIGURE 6. RAES of (a) MP and (b) MBP under $\pi^*(\text{C}=\text{O})$ excitation after Shirley background subtraction (dotted lines). The reproduced spectra (gray lines) were obtained by fitting with the normal Auger spectra of each MP or MBP SAM (green lines) and the spectator Auger spectra of 2D-aliphatic SAM (light blue lines).

Ultrafast charge transfer through biphenyl and fluorene monolayers studied by core-hole clock spectroscopy

Akinobu Niozu^a, Kakuto Yoshioka^a, Shogo Tendo^a, Shohei Asakura^b,
Yoshikazu Hanaki^b, Jumpei Koizumi^b, Yuri Ohura^b, Junna Yamada^b,
and Shin-ichi Wada^{a, c}

^aGraduate School of Science and Engineering, Hiroshima University,
Higashi-Hiroshima 739-8526, Japan

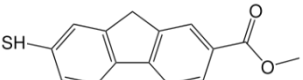
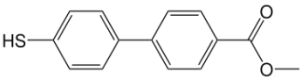
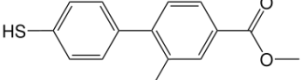
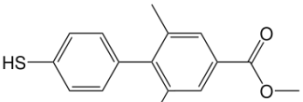
^bFaculty of Science, Hiroshima University, Higashi-Hiroshima 739-8526, Japan

^cHiroshima Synchrotron Radiation Center, Hiroshima University,
Higashi-Hiroshima 739-0046, Japan

Keywords: Self-assembled monolayers, charge transfer, core-hole clock spectroscopy

Nanoscale charge transfer dynamics are crucial for fundamental physical chemistry and applications, such as nanoelectronics and photovoltaics. For these applications, it is crucial to understand the correlation between the molecular structure and charge transport properties. Although molecular conductance has been extensively studied using single-molecule conductance measurements [1], a notable disparity exists between these fundamental investigations of single-molecule junctions and their direct application in functional devices. The use of self-assembled monolayers (SAMs) is a potential solution to bridge this gap given their capacity to form functional devices, thus connecting the insights gained from fundamental studies to practical applications.

TABLE 1. Molecular structures and torsion angles of the molecules in SAMs.

Name	Structure	Torsion angle / °
MFL		0
MBP		0 [3]
MmBP		52
MdmBP		90

In this study, we investigated ultrafast charge transfer through self-assembled monolayers of biphenyl and fluorene molecules via resonant Auger electron spectroscopy (RAES) using the core-hole clock (CHC) technique [2]. In this approach, molecules are resonantly core-excited with soft X-rays, and the subsequent electron transfer is probed by monitoring Auger decay spectra. The thiolated derivatives of biphenyl and fluorene used in this study are listed in Table 1. The addition of methyl groups induces torsion between the two phenyl rings within the SAMs, resulting in a reduction in π -conjugation. MBP molecules are anticipated to adopt an almost planar conformation [3], similar to that observed in bulk solids. Conversely, the methyl-substituted thiolates (MmBP and MdmBP) are expected to exhibit twisted conformations owing to steric hindrance from the methyl groups. Density functional theory (DFT) calculations of the relaxed molecular geometries yielded torsion angles of 52° and 90° for MmBP and MdmBP molecules, respectively. These molecules have a methyl ester (COOCH₃) moiety as the tail group, which serves as the site resonantly excited

with soft X-rays in the CHC experiments.

The methylester-terminated biphenyl and fluorene derivatives were custom-synthesized by and purchased from Tokyo Chemical Industry Co., Ltd. (for MFL, MmBP, and MdmBP) and NARD Institute Ltd. (for MBP). The SAMs were formed by immersing the Au substrates in 1 mM ethanol (for MBP, MmBP, and MdmBP) and toluene (for MFL) solutions of the precursors at 30 °C for 24 h. After immersion, the SAM samples were rinsed with solvent and dried under a flow of N₂ gas. The SAM samples were characterized using near-edge X-ray fine structure (NEXAFS) and X-ray photoelectron spectroscopy (XPS). NEXAFS, XPS, and RAES experiments were conducted at HiSOR BL13. NEXAFS spectra were collected at the C and O K-edges using the total electron yield mode. The XPS and RAES spectra were acquired at an X-ray incidence angle of 45° in the normal emission geometry using Omicron EA125 electron energy analyzer.

The C K-edge NEXAFS spectra showed several peaks corresponding to C 1s → π^* and C 1s → σ^* excitations. The polarization dependence of the π^* intensities indicated the orientational order of the molecules within the SAMs. The S 2p XPS spectra of the target SAMs confirmed sulfur species chemisorbed on Au. The NEXAFS and XPS spectra suggest the formation of ordered SAMs on the Au substrates.

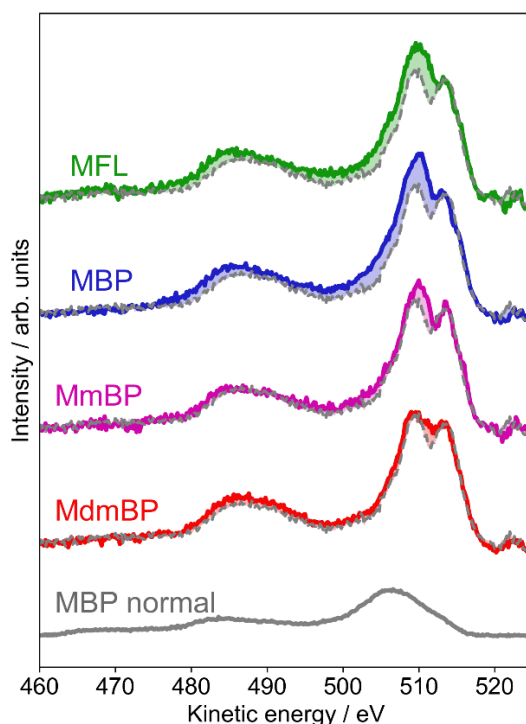


FIGURE 1. RAES spectra of MFL, MBP, MmBP, and MdmBP SAMs. The spectra were compared with the pure resonant spectrum recorded using the MHDA SAM and the normal Auger spectrum of the MBP SAM.

The RAES spectra at the O 1s → $\pi^*(\text{C}=\text{O})$ excitation are shown in Fig. 1. The spectra were compared with the pure resonant spectrum recorded with an MHDA (HS-(CH₂)₁₅-COOCH₃) SAM consisting of a long aliphatic chain, which was assumed to show no charge transfer contribution. The spectra for the MFL, MBP, and MmBP SAMs showed an increase in intensity corresponding to normal Auger decay, which indicates ultrafast charge transfer from the molecule to the Au substrate. For a quantitative analysis of the charge transfer dynamics, the RAES spectra were fitted with linear combinations of the normal Auger spectrum and the pure resonant Auger spectrum recorded with the MHDA SAM. The fitting analysis yielded charge transfer times of 16, 16, ~47, and ≥ 50 fs for the MFL, MBP, MmBP, and MdmBP SAMs, respectively. The CHC results demonstrate the conformational control of ultrafast charge transfer and suggest a negligible influence of the methylene bridge on the charge transfer dynamics.

REFERENCES

1. L. Venkataraman, J. E. Klare, C. Nuckolls, M. S. Hybertsen, and M. L. Steigerwald, *Nature* **442**, 904-907 (2006).
2. M. Zharnikov, *J. Electron Spectros. Relat. Phenomena* **200**, 160-173 (2015).
3. A. Masillamani et al., *Chem. - A Eur. J.* **18**, 10335-10347 (2012).

Soft X-ray Absorption Spectroscopy of Phospholipid Films Supported on Au Substrates by Different Casting Techniques

Yuri Ohura^a, Kakuto Yoshioka^b, Shogo Tendo^b, Akinobu Niozu^{a,b}, and Shin-ichi Wada^{a,b,c}

^a Faculty of Science, Hiroshima University, Higashi-Hiroshima 739-8526, Japan

^a Graduate School of Science and Engineering, Hiroshima University, Higashi-Hiroshima 739-8526, Japan

^c Hiroshima Synchrotron Radiation Center, Hiroshima University, Higashi-Hiroshima 739-0046, Japan

Keywords: Enter keywords. Linear polarization, XAS (X-ray absorption spectroscopy), NEXAFS (near edge X-ray absorption fine structure), Spin-casting, Phospholipids, DPPC

Lipids are one of the major constituents of living organisms. In particular, lipids self-assemble into oriented amphiphilic bilayers, which are the basic structure of the cell membranes. Lipid bilayers not only play an important protective role in maintaining cells, but also serve as sites for information transfer and protein reactions. Therefore, understanding the properties of lipid membranes is fundamental to studying biological mechanisms in detail, and to this end, attempts have been made to reproduce artificial cell membranes by supporting lipids on metal substrates. Lipid membranes supported on solid substrates (Figure 1), such as LB (Langmuir-Blodgett) and vesicle fusion methods, resemble natural cell membranes, and the information obtained are known to be biologically reliable. We have found that even a drop of an organic solution of phospholipid molecules onto a gold substrate can form a highly oriented multi lipid-bilayers. In this study, we prepared multi lipid-bilayer membranes by spin-casting method of lipid solutions, aiming to create more uniformly oriented bilayers and to evaluate the state of the bilayers.

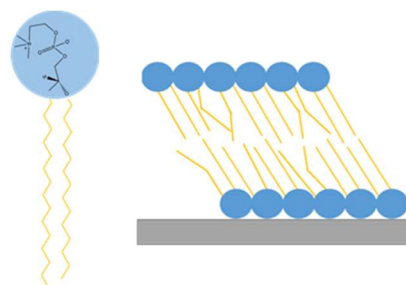


FIGURE 1. Molecular structure of DPPC phospholipids and schematic bilayer membrane.

DPPC shown in Figure 1 was used as the phospholipid and dissolved in chloroform to make a lipid solution. The solution was dropped onto Au substrates and dried under a nitrogen stream to create a multi lipid-bilayer membranes. The spin-casting method was also used to create a more uniform bilayer films on the substrates.

The prepared lipid films were characterized by NEXAFS (near edge X-ray absorption fine structure) measurements at HiSOR BL13 and AFM (atomic force microscopy) measurements at the laboratory. NEXAFS spectra were obtained by irradiating soft X-rays in the carbon K-edge region, and the emitted electrons were detected as drain current. The polarization angle dependence of the NEXAFS spectra was measured by changing the incidence angle of horizontally polarized X-rays on the sample surface, and the orientation angle of the organized lipid molecules was thereby determined to evaluate the differences in the multilayer films due to the different preparation methods.

In this study, soft X-ray absorption spectroscopy measurements were performed at different incident angles of soft X-rays to investigate the orientation angles of lipid films prepared by drop and spin-casting methods. Figure 2 shows NEXAFS spectra in the C K-edge region measured at different sample positions for lipid films prepared by drop and the spectrum for the lipid film prepared by spin-casting. The obtained NEXAFS spectra show characteristic resonant excitation peaks at specific energies and different spectral shapes with respect to the incident angle of soft X-ray. In other words, both lipid membranes are highly oriented, despite being multilayered.

Each spectrum can be fitted with a Gaussian function to extract each resonant excitation component. From the area intensities of fitted functions, the orientation angle of the transition dipole moment at each transition was determined. As a result, there is a clear difference between the orientation angles of the lipid films prepared by the drop and spin-casting methods. This is thought to be due to the difference in the method used to prepare the lipid films and the difference in the thickness of the films.

From the Rydberg and $\sigma^*(\text{C-C})$ transitions, the orientation angle of the hydrocarbon chains, which determines the overall shape of the lipid molecules, can be derived specifically. In lipid films prepared by the spin-casting method, the orientation angle is closer to 55 degrees, which is called the "magic angle", than in films prepared by drop-casting. Based on previous studies [1], it is thought that the orientation ordering is reduced in lipid films obtained by spin-casting due to the random structure of some of the hydrocarbon chains. In addition, the NEXAFS spectra of the lipid films obtained by spin-casting are different from those obtained by the drop-casting method in their detailed shape, and are in good agreement with the spectral shape of the single bilayer films in the previous study [1]. These results suggest that the spin-casted lipid films are sufficiently thin to be considered single bilayer films, unlike the drop method, and that the degree of freedom of the molecules constituting the films is increased in this ultra-thin state.

REFERENCES

1. M. Tabuse, A. Niozu, and S. Wada, *HiSOR Activity Report 2021*, 100-101 (2022).

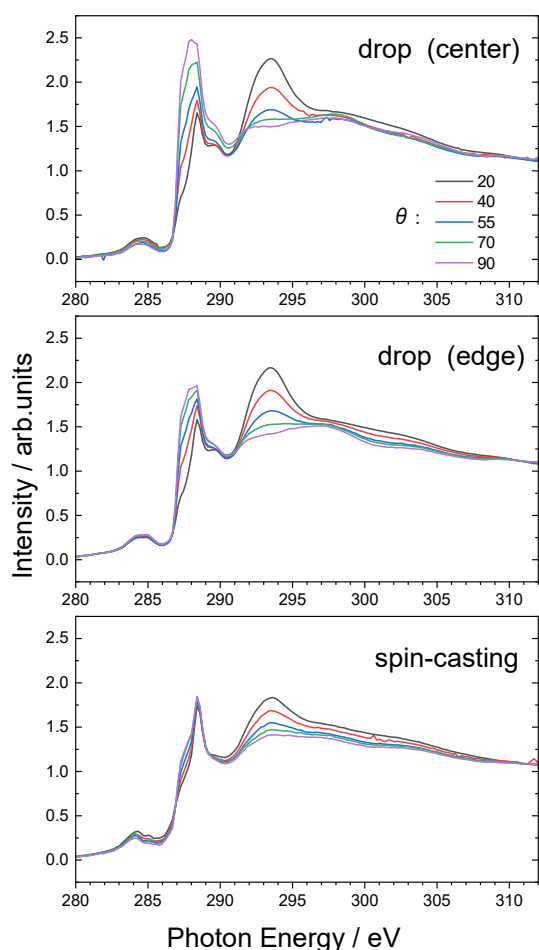


FIGURE 2. Polarization dependent NEXAFS spectra of (upper) center and (middle) edge positions of DPPC drop-casting films and (c) spin-casting film measured at C K-edge. θ : incident angle from the surface, and therefore the angle of electric vector from the surface normal.

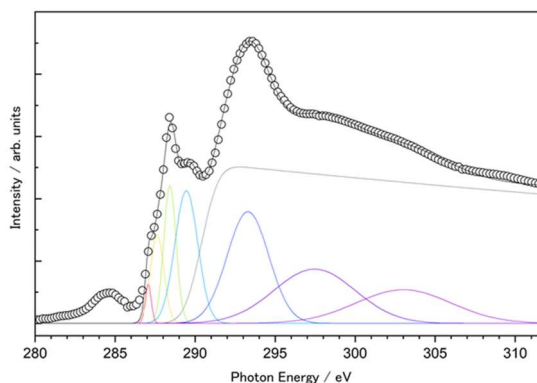


FIGURE 3. Typical result of Gaussian fitting obtained for drop-casting film at 55-degree incidence angle.